Chapter 4: Detection of Spatially Distributed Damage in Fiber-Reinforced Polymer Composites

4.1 Abstract

This work is a first look detecting detection embedded within glass fiber reinforced polymer composites. Damage detection is achieved by monitoring the spatially distributed electrical conductivity of a piezoresistive multi-walled carbon nanotube thin film. First, thin films were spray-deposited directly upon glass fiber mats. Second, using electrical impedance tomography (EIT), the spatially conductivity distribution of the thin film was determined before and after damage events. The resolution of the sensor was determined by drilling progressively larger holes in the center of the composite specimens, and the corresponding EIT response was measured. In addition, the sensitivity to damage occurring at different locations in the composite was also investigated by comparing EIT spatial conductivity maps obtained for specimens with sets of holes drilled at different locations in the sensing area. Finally, the location and severity of damage from impact events was detected using the EIT method. The work presented in this study indicates a paradigm shift in the possibilities available for structural health monitoring of fiber-reinforced polymer composites.

4.2 Introduction

For over 50 years, fiber-reinforced polymer (FRP) composites have been used with increasing frequency in retrofitted and newly constructed structures. This utilization spans the aerospace, wind turbine, automotive, naval, and civil industries. The reason for their widespread adoption is that FRPs feature high strength-to-weight ratios, resistance to fatigue and corrosion, as well as high conformability

and tailorability to a specific design. Despite these impressive characteristics, FRPs are still susceptible to damage due to a variety of avenues, including overloading, impact events, chemical penetration, multi-axial fatigue, and/or a combination of all of the above. Such damage tends to manifest in various modes, such as delamination, fiber- or matrix-breakage, fiber-matrix debonding, and matrix swelling, among others. They typically occur internal to the laminate architecture of the composite, thereby making damage nearly invisible to visual inspection. As visual inspection is a common structural monitoring approach [1, 2], this is a serious cause for concern.

Due to the internal nature of damage within FRP composites, several groups have focused on embedded sensing methodologies into the layered architecture of composite materials. Direct strain measurements have been performed using embedded foil-based strain gauges [3, 4] and fiber-Bragg gratings [5-8]. These are both point-based methodologies that have high resolution at the point of sensor application. However, to get a global view of structural health, dense instrumentation and interpolation methods must be implemented for damage detection purposes. It has also been found that an embedded optical fiber that has a diameter larger than 100 μm can lead to mechanical performance degradation [6]. Other groups have focused on embedding piezoelectric sensors within the composite architecture for acoustic emission [9, 10] and ultrasonic imaging [11-13]. Acoustic and ultrasonic imaging allow for higher resolutions of damage detection within the composite, but the embedded piezoelectric sensors and actuators can act as crack initiators, thus leading to a shorter service life of the composite part [14].

To negate the issues of embedding macro-scale sensors within composite structures, others have used changes in inherent or incorporated electrical properties of FRP composites for structural health monitoring (SHM). Several groups have measured the change in resistance of the fibers in carbon fiber-reinforced polymer (CFRP) composites while they are subjected to tensile and compressive loads [15-18]. In addition to characterizing CFRP piezoresistivity, others have focused on characterizing changes in their electrical properties due to incurred damage from transverse cracking [19-21], fatigue [22], and delamination [23]. For non-conductive FRPs like glass fiber-reinforced polymer (GFRP) composites, carbon nanotube (CNT)-based nanocomposites have been investigated for *in situ* sensing. This work has been motivated by observing the high piezoresistivity of individual carbon nanotubes [24-26]; since this discovery, extensive work has been conducted in characterizing how electrical changes to these

nanocomposites correlate to applied strain and incurred damage. Much of this work involves incorporating carbon nanotubes into the epoxy matrix of GFRPs. Carbon nanotubes have been shown to not only enhance their mechanical properties but also introducing electrical conductivity to the epoxy matrix (*i.e.*, if the appropriate functionalization of CNTs are performed prior to their dispersion) [27-32]. Additional work has demonstrated the sensitivity of these epoxy-based nanocomposites to applied strain [33, 34] and damage [33-36]. Others have focused on using CNT-based thin films for applied sensing. Typically, most work in this area involves manufacturing a thin film and affixing it onto the structural surface to be monitored. In one case, the CNT-based thin film has been deposited directly onto a glass fiber weave and embedded within a composite structure for actual *in situ* monitoring [37]. Unlike conventional point-based strain transducers, CNT-based thin films are sensitive to strain at every location of the material. Therefore, it is highly desirable to take advantage of their inherent distributed strain sensitivity as long as a corresponding spatially distributed electrical measurement method is available.

For just over 30 years, medical- and geophysical-focused research groups have been investigating the application of a soft-tomographic imaging method called electrical impedance tomography (EIT). EIT is capable of determining the conductivity distribution within a 2D or 3D body bounded by electrodes. An EIT measurement is taken by injecting current between two electrodes while simultaneously measuring the electric potential at the remaining electrodes. A full measurement consists of several of these electrical current injection patterns. The reconstruction to determine the spatial conductivity distribution is ill-posed, and its calculation has only been possible since the establishment of the mathematical framework proposed by Calderon [38] in 1980. Since then, several groups have created algorithms to perform this reconstruction using one-step [39, 40] or iterative [41-43] solvers for isotropic [44, 45] and anisotropic [46, 47] conductivity distributions. Very limited research has been conducted to date to bring this electrical imaging modality for SHM applications; examples include work by Loh *et al.* [48] for strain/impact, Hou *et al.* [49] for pH, Pyo *et al.*[50] for corrosion, Lazarovitch *et al.* [51] for cracking, and Alirezaei *et al.* [52, 53] for pressure/deformation monitoring. Despite creating a foundation for future EIT work in SHM, more studies are required for achieving embedded and *in situ* sensing and for detecting structural damage occurring within the material body.

This study introduces embedded spatial sensing for SHM of structural components such as FRPs. First, a piezoresistive multi-walled carbon nanotube (MWNT)-poly(vinylidene fluoride) (PVDF) film is spray-deposited directly onto a glass fiber mat, which is then embedded in a GFRP composite. Depositing the MWNT-PVDF thin film on the fiber mat allows for a higher sensitivity to fiber damage, and the film is protected from ambient environmental conditions by the encapsulating epoxy matrix. Second, EIT measurements are taken to detect damage from drilled holes, and they simulate well-defined damage. Once the sensitivity and resolution are established, EIT measurements are performed to detect damage from different impact energies. EIT takes advantage of MWNT-PVDF's spatial piezoresistivity by reconstructing its spatial conductivity distribution in which its change in electrical conductivity at each point is calibrated to applied strain. The reconstructed spatial conductivity map thus provides location and severity information of damage. Finally, difficulties in measurement strategy and reconstruction arising from the specimens' anisotropic electrical conductivity (*i.e.*, due to the unidirectional glass fiber mats used) have been overcome. This work serves as a first step in enabling a field deployable *in situ* spatial damage detection methodology for GFRP composites.

4.3 Electrical Impedance Tomography

Electrical impedance tomography is a soft-field tomographic imaging method that uses boundary voltage measurements from propagated electric current to reconstruct the 2D or 3D conductivity distribution with an area or volume bounded by measurement electrodes. A measurement is performed by injecting a current between two boundary electrodes, and the differential voltage is measured for the remaining electrodes that are adjacent to one another. To remove some electrode contact resistance effects, voltage measurements are not taken for the pair of electrodes used to inject current (where one is the input, and another is set to ground). This approach allows for a more stable calculation of the voltage distribution for each current propagation [45]. The reconstruction of the conductivity distribution is based on Laplace's equation:

$$\nabla \cdot \sigma \nabla u = 0 \tag{4.1}$$

In Equation (1), σ represents the conductivity distribution in the sensing area, and u is the corresponding voltage distribution, where both can be expressed as functions of spatial Cartesian coordinates (*i.e.*, (x,y) in

2D and (*x*,*y*,*z*) in 3D). Because very few analytical solutions are known for this equation, it is typical to perform these calculations numerically using the finite element method (FEM), where the conductive area is discretized into triangular elements. In this study, each element is assumed to have a constant conductivity. The numerical calculation is performed using a weak formulation of Laplace's equation as shown in Equation (2):

$$\iint_{\Omega} \nabla \phi \cdot \sigma_{\Omega} \cdot \nabla u dx dy = 0 \tag{4.2}$$

In Equation (2), ϕ is the linear shape function to account for the voltage at each node, which is located at the corner of each triangular element. To take the current injection and ground boundary conditions into consideration, Equations (3) and (4) are applied at each electrode in the mesh:

$$\int_{E_l} \sigma \frac{\partial u}{\partial \upsilon} ds = I_l \tag{4.3}$$

$$u + z_l \sigma \frac{\partial u}{\partial \upsilon} = V_l \tag{4.4}$$

Equation (3) mandates that the current injected at a specific electrode (E_l) must be normal to the surface of the electrodes and must total the amount of current in the actual measurement. Equation (4) governs the voltage drop between the electrode and that of the conductive medium due to contact resistance (z_l) [44, 54].

Typically, Laplace's equation is solved as a forward problem, where the body's conductivity distribution is known, and the boundary voltage distribution is calculated. In the case of EIT, the spatial conductivity is desired, whereas the boundary voltage values are known (*i.e.*, from experimental measurements), thus necessitating solving the inverse problem. As discussed previously, many reconstruction methods have been created in the literature. For SHM, detecting changes in the conductivity with respect to a baseline is what is desired for damage detection. For this reason, the linearized reconstruction strategy developed by Adler and Guardo [40] is used for normalized differential reconstruction. Their reconstruction algorithm, called Maximum a Posteriori (MAP), is a one-step solver, which is ideal for real-time measurements. For this reconstruction, two sets of boundary electrode voltage measurements are required, where an initial measurement is obtained and then compared to a measurement

later in time. The difference is calculated for each individual voltage measurement (ΔV) and is then divided by the corresponding initial measurement (V_0). The reconstruction is based on Equation (5):

$$\frac{\Delta\sigma}{\sigma_0} = \left(H^T W H + \lambda R\right)^{-1} H^T W \left(\frac{\Delta V}{V_0}\right) \tag{4.5}$$

The MAP algorithm reconstructs the normalized difference in conductivity, using the normalized differential voltage measurements between two points in time. This reconstruction is mainly governed by the sensitivity matrix (H), which correlates a small and normalized change in conductivity in one element to a normalized change in voltage at the boundary electrodes. The sensitivity matrix takes changes from all of the elements into account, facilitating the reconstruction. Normalized differential imaging has the advantage that the injection current's magnitude and the contact resistance values do not play a part in the calculation of the sensitivity matrix. The Gaussian white noise from the voltage measurements is taken into account in the variance matrix (W), where:

$$W_{i,i} = \frac{1}{\alpha_i} \tag{4.6}$$

In Equation (6), α_i is the variance for measurement i. As mentioned earlier, the EIT reconstruction is ill-posed due to the higher number of elements to reconstruct than the available voltage measurements.

The ill-posedness of the inverse problem is overcome through regularization, which typically imposes conditions of smoothness to stabilize the reconstruction. In this case, the regularization matrix R is based on a Gaussian high-pass filter to implement smoothing. The regularization hyperparameter (λ) must be determined to specify how much smoothing is necessary. This is accomplished by calculating the conductivity reconstructions corresponding to different λ values until the signal-to-noise ratio (SNR) is a specified multiple of the SNR of the voltage measurements. The ratio of the voltage SNR (SNR_V) to the SNR of the reconstructed conductivity (SNR_σ) is termed the noise figure (NF):

$$NF = \frac{SNR_V}{SNR_\sigma} \tag{4.7}$$

The NF used in this work has been set to 1, as has also been used by Graham and Adler [55].

4.4 Experimental Methodology

To demonstrate the performance of EIT as an embedded SHM methodology, a conductive and piezoresistive film needs to be deposited within the electrically non-conductive GFRP structure. A MWNT-PVDF film was formulated and spray-deposited on a glass fiber mat, which was stacked with other glass fiber mats and infused with epoxy to fabricate GFRP panels. These specimens were characterized for their damage resolution using progressively larger drilled holes in the center of the sensing area. In addition, sensitivity to damage occurring at different locations within the sensing area was also explored. Once the damage sensitivity was determined, the impact damage detection capability of the EIT method was investigated.

4.4.1 MWNT-PVDF Film Fabrication

A two-part conductive film was formulated for spray-deposition over large substrates. The first component of the film formulation was based on an MWNT-PSS/NMP solution. The formulation started with preparation of a 2 *wt.*% solution of poly(sodium 4-styrenesulfonate) (PSS) (~1M M_W, Sigma-Aldrich) that was dissolved in deionized (DI) water using high-energy tip-sonication (D-450D, Branson) for at least 10 min. An addition of the appropriate amount of MWNTs (SouthWest Nano Technologies) and a polar solvent called N-methyl-2-pyrrolidone (NMP) (Sigma-Aldrich) was mixed and added to the PSS solution. The NMP is used as a coalescing agent for the PVDF particles, as will be discussed later. This MWNT-PSS/NMP solution was tip-sonicated for 30 min, which was enough time to fully disperse the nanotubes. Dispersion was achieved via steric stabilization between the PSS and the MWNTs [56], and the NMP also aided with the dispersal of the MWNTs [57].

The second component of the formulation contained a latex of 150 nm diameter, spherical, sub-microparticles of Kynar PVDF suspended in a Aquatec surfactant solution (Arkema). The solution was diluted to an appropriate mass concentration using DI water. Just before spray-deposition, the first component is mixed vigorously into the second component. This created a segregated network of MWNTs, as they were unable to penetrate the PVDF particles. The final solution prior to spray-deposition was 13% solids weight content with 5 *wt.*% MWNTs. Figure 4.1 shows an illustration of this segregated network of MWNTs in the latex solution.

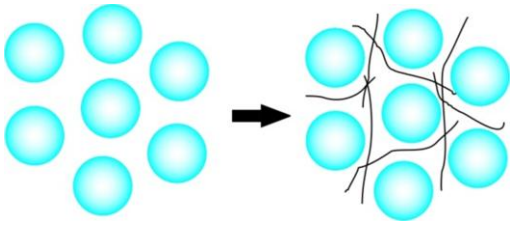

Figure 4.1. An illustration of the MWNTs (black lines) in the PVDF (blue spheres) latex solution is shown.

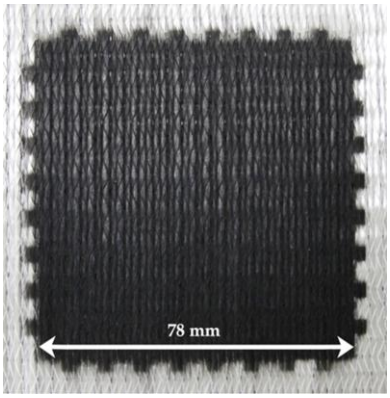

Figure 4.2. A photograph of the mask for one sensing area is shown. The smaller squares along film boundaries are for the electrode pads.

Once the film formulation was fully incorporated, it was spray-deposited using a VL-series airbrush (Paasche Airbrush). The substrates, upon which the solutions were sprayed, were unidirectional E-LR 0908 fiber mats (Vectorply) cut to 381 × 381 mm^2. The substrates were masked to contain six equally spaced 78×78 mm^2 sensing areas. In addition, the mask also allowed one to spray eight 3×3 mm^2 squares along each side of the square sensing area. The squares along the film boundaries were used for the electrode pads and were separated 6 mm apart. Once the film was spray-deposited, the substrates were dried in an oven heated to 60 °C for 10 min. A dried film on a unidirectional glass fiber mat is displayed in Figure 4.2, in which one can see the electrode pads extending from the main sensing area.

4.4.2 GFRP Composite Manufacturing

Once the MWNT-PVDF film was deposited on a number of the glass fiber mats, the GFRP composites were laid up in a $[0°/+45°/90°/-45°]_{2s}$ stack sequence, for a total of 16 layers. Using a vacuum-assisted resin transfer molding (VARTM) process, the stacked glass fiber mats were infused with a two-part epoxy system (117LV/237, Pro-Set), which was cured at 27 °C for 15 h and then 80 °C for 8 h. After the cure process was complete, the panels were cut into six specimens, each with dimensions of 150×100 mm^2 as shown in Figure 4.3.

In order to allow for easy access to the sensing layers, the glass fiber mats with the applied MWNT-PVDF films were only deposited on the top and bottom plies of the composite laminate. Since epoxy is nonconductive, easy access to the electrodes was facilitated prior to the infusion and curing of the epoxy. Here, adhesive copper tape, with a wax paper backing, was applied copper side down on each

electrode pad of MWNT-PVDF film (prior to infusion). The tape was affixed using conductive colloidal silver paint (Ted Pella). After infusion, epoxy flowed around the applied copper tape and adhered to it instead of the MWNT-PVDF film of the electrode pad. A razor blade was used to cut around the perimeter of the wax paper tape backing. The wax paper then detached from the conductive adhesive of the copper tape, and the tip of the knife was used to peel back the wax paper with encasing epoxy attached. To guarantee a good electrical connection, a top coat of colloidal silver paint was also applied to each exposed electrode. The conductive electrode pad was then exposed and was used for performing the EIT measurements. Final preparation of each specimen involved uncovering all 32 electrodes.

4.4.3 Anisotropic Spatial Conductivity Considerations

Due to the stacking sequence, the outer plies had a fiber orientation of 0° direction, which lies in the vertical direction as shown in Figure 4.3. Due to this fiber direction, the conductivities in the vertical direction are about twice as conductive as compared to the horizontal. To accommodate for this anisotropic conductivity, the scalar conductivity values in Equations (1-4) became matrix values with non-zero diagonal components. Equation (8) states how the conductivity is taken into consideration in this study:

$$\sigma = \begin{bmatrix} \sigma_{90^\circ} & 0 \\ 0 & \sigma_{0^\circ} \end{bmatrix} = \begin{bmatrix} 1 & 0 \\ 0 & \left(\frac{\sigma_{0^\circ}}{\sigma_{90^\circ}}\right) \end{bmatrix} \sigma_{90^\circ} = \begin{bmatrix} 1 & 0 \\ 0 & \left(\frac{\sigma_{0^\circ}}{\sigma_{90^\circ}}\right) \end{bmatrix} \sigma^* \tag{4.8}$$

The values σ_0 and σ_{90} were determined by taking two-point probe resistance measurements across the sensing area, using the applied electrodes and in the directions indicated.

In the normalized differential reconstruction, only the scalar value of σ^* was reconstructed and not the full matrix values. The degree of anisotropy was assumed to be the same across the sensing area, with the scalar value of the conductivity (σ^*) assumed to change. This approach had been used before for other anisotropic EIT conductivity mapping applications. Introduction of the anisotropic conductivity into the sensitivity matrix was straightforward, where the conductivity matrix was directly applied to Equations (2-4) [47]. The anisotropic conductivity changed the EIT approach in two ways, which were the calculation of the sensitivity matrix and the pattern with which the current was injected. Figure 4.4 illustrates the current injection pattern used in this study, where the blue lines connect the injection-ground electrode pairs. As indicated in Figure 4.4, electrical current is directed to flow transverse and diagonal to the vertical direction

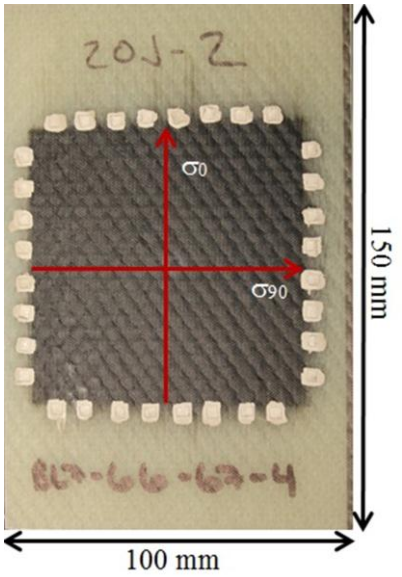

Figure 4.3. Photograph of a GFRP specimen with embedded MWNT-PVDF film. The anisotropic nature of the conductivity is indicated by the arrows.

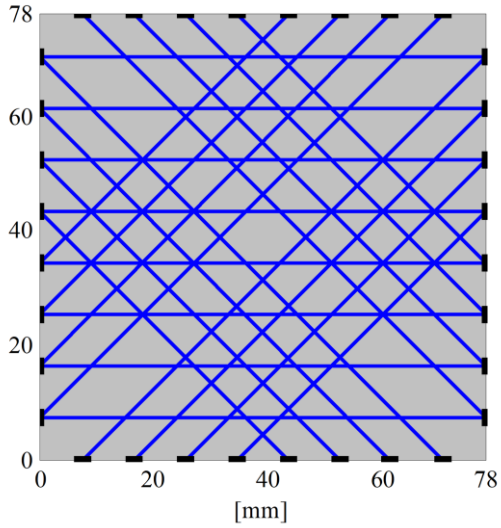

Figure 4.4. This schematic shows the current injection pattern used due to the anisotropic conductivity of the embedded MWNT-PVDF films. The blue lines indicate current injection pairs, and the thick black lines along the boundaries are the electrodes.

due to the anisotropic nature of spatial conductivity. If current is propagated in the vertical direction, the current distribution does not spread transverse to the current path, which leads to differential voltages of zero at the boundaries.

4.4.4 EIT Data Acquisition

As mentioned in Section 4.3, redundant sets of current injection-boundary voltage measurements were required for solving the EIT inverse problem. A customized acrylic fixture with 32 spring-loaded pins (Everett Charles Technologies) was designed for interrogating the test specimens (Figure 4.5). The acrylic fixture was designed to fit directly over each composite specimen, and each of the spring-loaded pins was aligned with each of the film boundary electrodes. The pins were positioned such that each of them landed at the center of each electrode. Boundary voltage measurements were collected using an Agilent 34980A equipped with a 34932A matrix switch, and a Keithley 6221 AC/DC current source was also connected to the Agilent 34980A switch for current generation and grounding. The current amplitude used in this study was a 100 μA DC current.

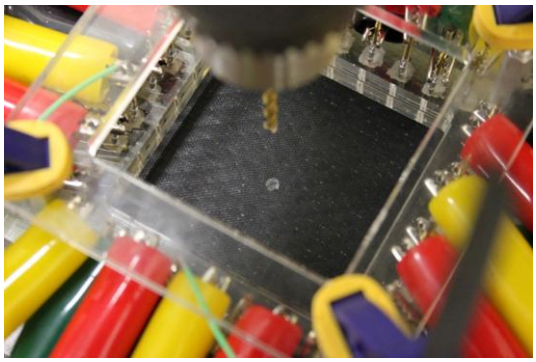

Figure 4.5. A customized fixture is used for obtaining EIT measurements. The image also shows a specimen undergoing the damage sensitivity characterization study, and a 3.18 mm hole has just been drilled.

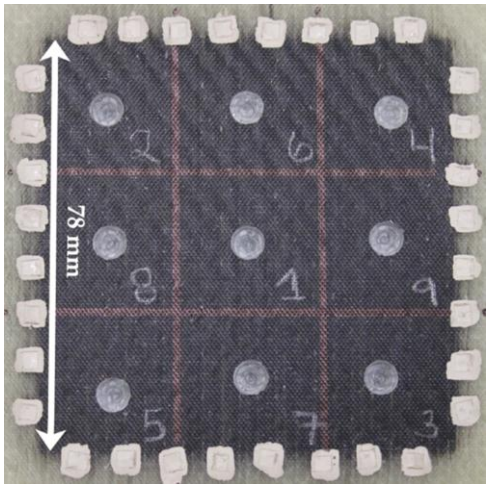

Figure 4.6. A representative specimen used for the damage sensitivity study is shown. A total of nine 6.35 mm holes have been drilled.

4.4.5 Damage Sensitivity Characterization

Progressively larger holes were drilled in the center of GFRP specimens for determining the damage detection resolution and sensitivity limit of the EIT method (Figure 4.5). The specimens were secured and mounted in a drill press while connected to the EIT measurement setup. Using titanium nitride-coated bits, holes of diameter 1.59 mm, 3.18 mm, 4.76 mm, 6.35 mm, 7.94 mm, 9.53 mm, and 12.7 mm were drilled at the center of each specimen. An EIT measurement was taken of the pristine specimen as well as after each hole was drilled. The EIT spatial conductivity reconstructions were performed in reference to the pristine specimen.

In addition to characterizing the damage severity at the center of the sensing area, the sensitivity of EIT to damage occurring at different locations within the sensing area was also characterized. To perform this characterization, a 3×3 grid was drawn on a specimen as shown in Figure 4.6. In the center of each region, a 6.35 mm hole was drilled; the sequence of drilling is based on the numbers shown in Figure 4.6 (starting with the center). An EIT measurement was performed of the pristine specimen and after every hole was drilled. Once again, the EIT images were reconstructed in reference to the pristine specimen.

4.4.6 Impact Damage Detection

With the sensitivity to prescribed damage sizes characterized, the proposed EIT technique was also investigated for detecting different magnitudes of impact damage. Following the ASTM standard

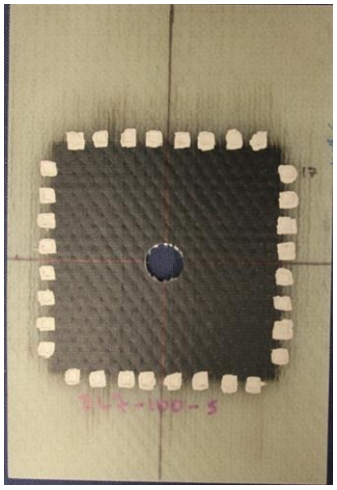

Figure 4.7. A GRFRP specimen is drilled with a 6.35 mm hole drilled in the center. This specimen has been used to determine the hyperparameter.

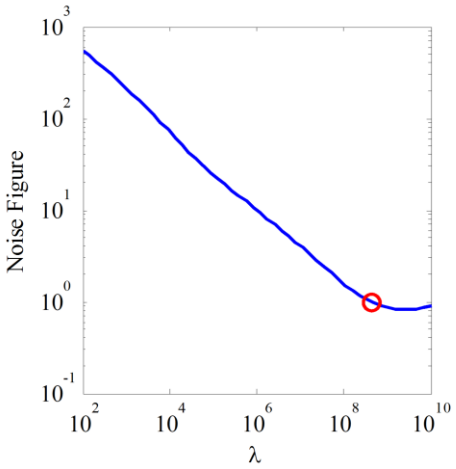

Figure 4.8. Noise figure is determined and plotted for values of hyperparameters ranging from 10^2 and 10^{10}. The hyperparameter with a *NF* of 1 is indicated with a red circle and has a value of $\lambda = 4.539\times10^8$.

D7136, specimens were subjected to nominal values of 20 J, 60 J, 100 J, and 140 J impact energies, using an instrumented Instron Dynatup 9250G drop-weight tester. EIT measurements were taken before and after each impact event. The reconstructions were conducted in reference to the initial measurement of the undamaged specimen. To verify the EIT response, the specimens were compared to photographs taken after the impact events.

4.5 Results and Discussion

4.5.1 Hyperparameter Calibration

As have been discussed in Section 4.3, a regularization hyperparameter must be determined for smoothing and stabilizing the EIT inverse problem. To find this parameter, a 6.35 mm hole was drilled in the center of a pristine specimen as shown in Figure 4.7. EIT boundary electrode measurements were acquired before and after drilling. Then, EIT spatial conductivity reconstructions was performed using the two datasets and with varying hyperparameter values ranging from 10^2 to 10^{10}. For each reconstruction, the noise figure is calculated using Equation (7), and the results are plotted in Figure 4.7. Using linear interpolation, the hyperparameter that corresponds to a *NF* of 1 was determined and used for the remainder of this study.

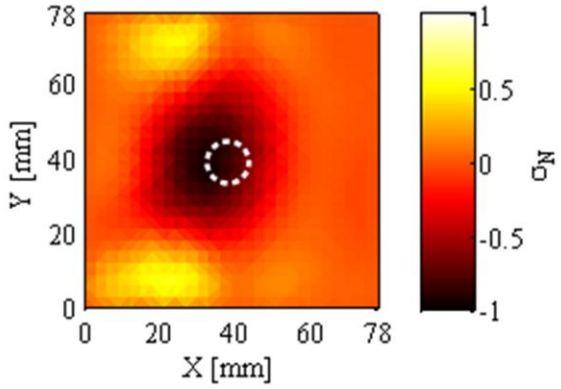

Figure 4.9. The EIT normalized spatial conductivity map for the specimen with a 6.35 mm center hole is shown. This reconstruction uses the hyperparameter that yielded a *NF* of 1. The dashed white circle indicates the locations of the actual hole.

The EIT reconstruction that corresponds to the hyperparameter with a *NF* of 1 is shown in Figure 4.8. First, as described in Section 4.3, the EIT algorithm employed in this study solves for the relative or normalized change in spatial conductivity (Equation 5). Thus, the EIT spatial conductivity maps only show relative conductivity changes, where the normalized change in conductivity of each element in the EIT FEM model ($\Delta\sigma_N$) is calculated using Equation (9):

$$\Delta\sigma_N = \frac{\Delta\sigma}{\sigma_0} \cdot 100\% \tag{9}$$

Figure 4.9 shows the EIT spatial conductivity map for the drilled specimen shown in Figure 4.7. The decrease in conductivity that corresponds to the drilled hole can be easily discerned in the center of the sensing area. One aspect of this reconstruction is the positive change of conductivity that is collocated near the circumference of the drilled hole. This phenomenon tends to happen with many EIT reconstruction algorithms, where a sharp change in conductivity will cause the reconstruction to slightly trend towards the opposite magnitude (faint yellow ring) before converging again to the actual conductivity distribution in the vicinity [40, 47, 55]. The two circular areas, one on the top-left and one on the bottom-left in Figure 4.9, may also be due to this phenomenon.

4.5.2 Damage Sensitivity Characterization

EIT damage sensitivity characterization studies based on the procedure outlined in Section 4.4.5 have been performed. EIT spatial conductivity maps corresponding to different drill-hole sizes and holes of

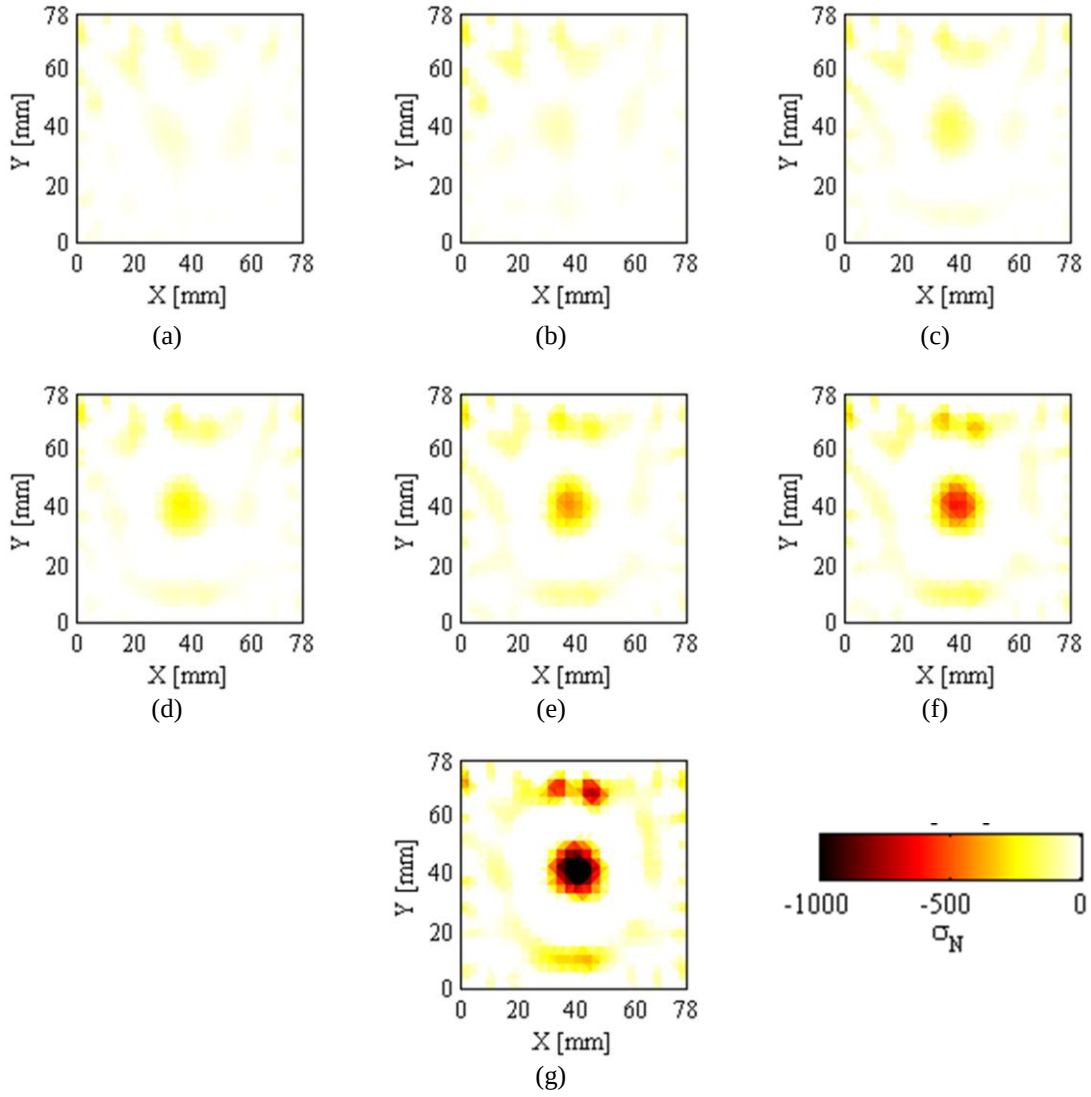

Figure 4.10. The spatial conductivity maps for drilled holes with diameters of (a) 1.59 mm, (b) 3.18 mm, (c) 4.76 mm, (d) 6.35 mm, (e) 7.94 mm, (f) 9.53 mm, and (g) 12.7 mm are shown.

the same size drilled at different locations have been reconstructed using the hyperparameter determined in Section 4.5.1. This study allows one to characterize the method's damage detection resolution and the sensitivity to damage located at different positions within the sensing area. First, a set of representative EIT reconstructions corresponding to a specimen subjected to different drill-hole sizes is shown in Figure 4.10. From Figure 4.10b, one can see that damage due to a 3.18 mm drilled hole is detectable, although the normalized change in conductivity is comparable to the level of background noise. This contrast continues to grow with increasing hole size, resulting in a contrast of about -1,000%

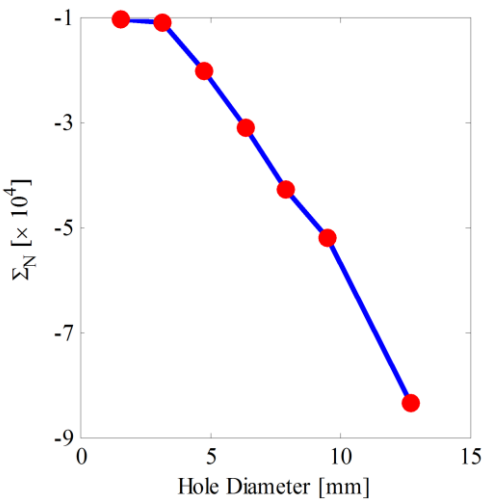

Figure 4.11. Σ_N has been calculated using EIT conductivity maps and plotted as a function of drilled center hole sizes.

for the 12.7 mm hole. While the theoretical normalized decrease in conductivity (Equation 9) is -100%, it is thought that the exaggerations observed in the results shown in Figure 4.10 are due to the anisotropic model. The degree of anisotropy might be higher than that measured using the resistance measurements. Nevertheless, the algorithm has successfully indicated the location and relative severity of enlarging damage from drilling.

To quantify the response due to the drilled holes, a metric (Σ_N) has been created and is based on integrating the normalized EIT spatial conductivity response. As shown in Equation 10,

$$\Sigma_N = \int_{\Omega} \sigma_N \, dA \quad \text{for} : \sigma_N < 0 \tag{10}$$

this integral is performed over a subset of the sensing area (Ω) which consists of only elements with negative values of σ_N (*i.e.*, due to damage). In this case, Ω is a 30×30 mm^2 square region in the center of the sensing area. Σ_N has been calculated for each of the EIT spatial conductivity maps corresponding to the different drill-hole sizes. The resulting values for Σ_N is plotted as a function of hole diameter as shown in Figure 4.11. There is a distinct linear trend between Σ_N and hole diameters from 3.18 mm to 12.7 mm. This linearity not only indicates the smallest damage the algorithm can detect (*i.e.*, 3.18 mm relative to a 78 mm sensing area), but it also validates the use of a linear EIT reconstruction algorithm. Furthermore, the center of the sensing region has the lowest sensitivity due to the distance from the electrodes [45], so smaller-sized damage may be detectable if they are located closer to the film boundaries.

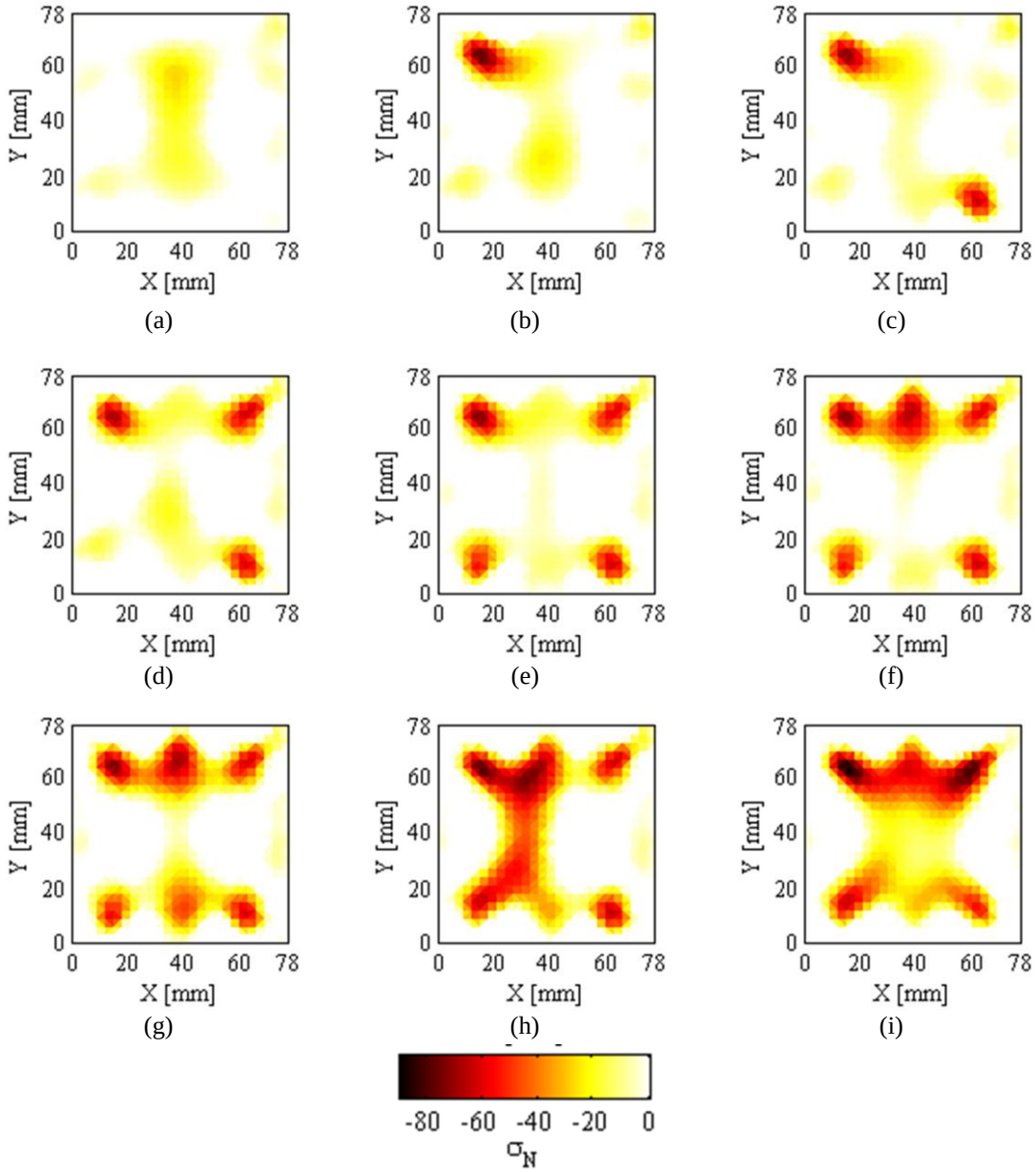

Figure 4.12. Normalized spatial conductivity maps for 6.35 mm holes drilled at different regions are shown. Each image corresponds to EIT measurements taken after a new hole has been created in the (a) center, (b) upper-left, (c) lower-right, (d) upper-right, (e) lower-left, (f) upper-center, (g) lower-center, (h) center-left, and (i) center-right of the 3×3 grid.

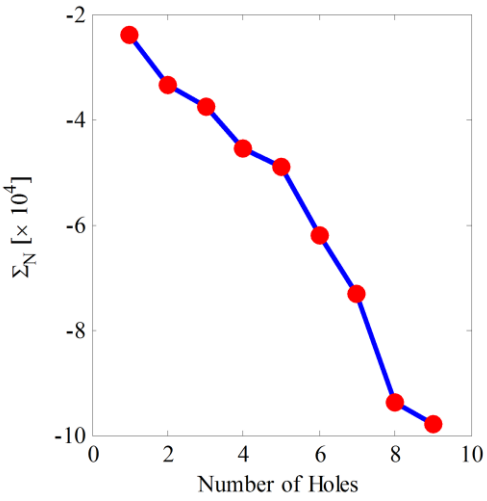

Figure 4.13. Σ_N has been calculated using EIT conductivity maps and plotted as a function of the number of drilled holes.

In addition to characterizing EIT response to damage size, the method has also been tested for its sensitivity to the location of damage. The EIT reconstruction has been performed for each set of measurements corresponding to after each drilled hole, as have been explained in Section 3.4. The results of are presented in Figure 4.12. Figure 4.12a shows the EIT reconstruction for a 6.35 mm hole located in the center of the sensing area (*i.e.*, first drilled hole). The reconstruction shows a localized change in spatial conductivity, although the results are elongated along the vertical direction. This effect is thought to be due to the anisotropic model, where the characterizing resistance measurements might not capture the correct anisotropic conditions. For the normalized spatial conductivity maps shown in Figures 4.12b to 4.12g, one can see that holes drilled in the top and bottom rows are clearly detected. However, Figures 4.12h and 4.12i show that damage corresponding to those locations can be detected, but the reconstruction pushes the localized changes in conductivity towards the center of the sensing area. Again, it is hypothesized that this is due to a discrepancy between the anisotropy of the conductivity distribution and that accounted for in the EIT reconstruction model. Despite these effects, when the corresponding response to each hole is characterized using the Σ_N metric, the response is fairly linear with respect to the number of holes present (Figure 4.13). It should be mentioned that the domain of integration Ω in this case was set to the entire sensing area (due to the distribution of hole across the entire sensing area). The linearity of the response further validates that the linear MAP reconstruction approach is appropriate for these measurements.

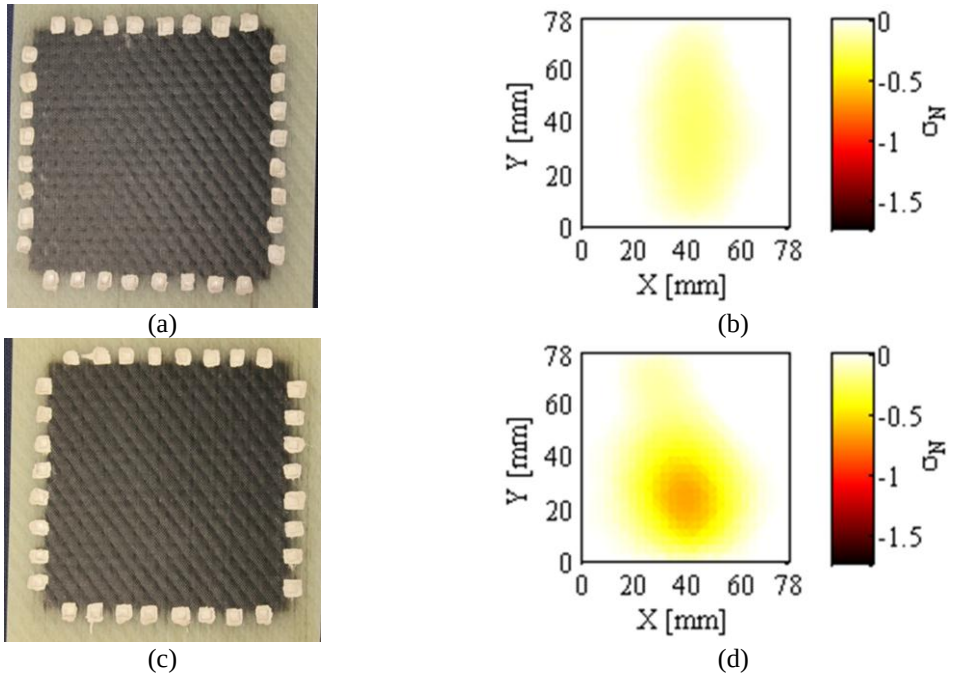

Figure 4.14. GFRP specimens have been subjected to impact testing. (a) The photograph and (b) EIT reconstruction of a specimen subjected to 20 J of impact is shown. (c) The photograph and (b) EIT map of a specimen subjected to 60 J of impact is also shown. The results suggest that EIT can detect the location and differences in magnitude of impact damage.

4.5.3 Impact Damage Detection

Section 4.2 has shown that the proposed film-enhanced composite specimens and EIT technique are able to detect and measure the location and severity of damage simulated by drilled holes (*i.e.*, full penetration of the MWNT-PVDF film and composite specimen). However, damage due to impact is far more complex and does not always cause damage to the exterior plies. Thus, following the procedures in Section 3.5, a series of tests has been conducted for characterizing the film and EIT's ability to detect impact damage. The experiment has been designed such that 20 J and 60 J of impact energy do not impart fracture damage to the exterior plies, and damage is confined within the internal structure of the multilayered GFRPs.

Figures 4.14a and 4.14c show two representative specimens impacted at 20 J and 60 J of nominal impact energy, and they do not cause apparent visual damage. Unlike visual inspection, EIT provides greater sensitivity to damage and can provide information regarding damage occurring internal to the material. The corresponding EIT spatial conductivity maps for specimens subjected to 20 J and 60 J of impact are shown in Figures 4.14b and 4.14d, respectively. It can be observed from these figures that the MWNT-PVDF film and EIT method successfully captures changes occurring internal to the structure. In

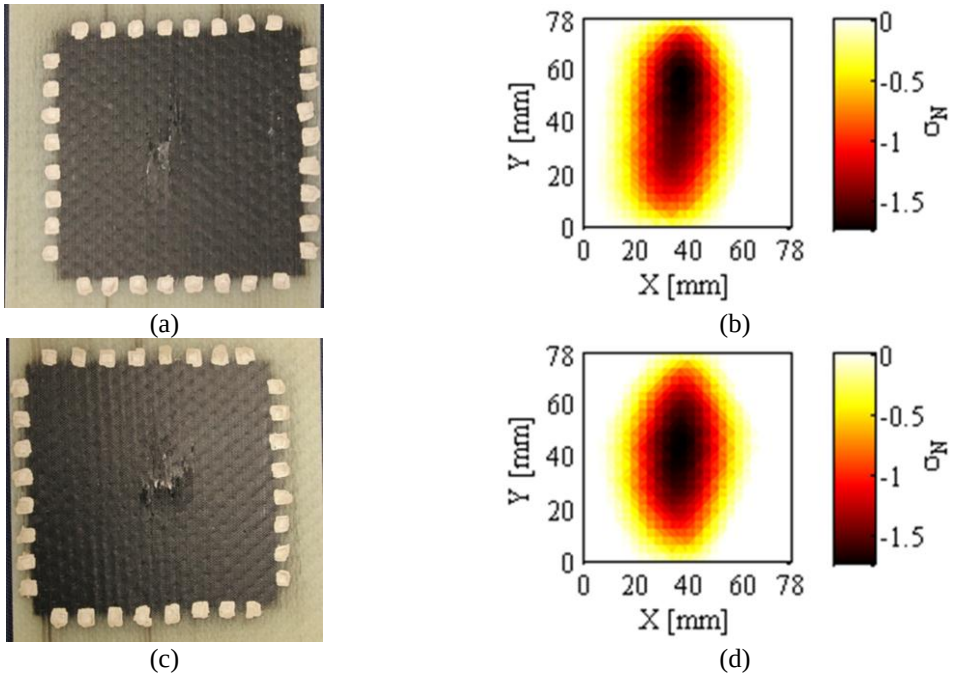

Figure 4.15. GFRP specimens have been subjected to impact testing. (a) The photograph and (b) EIT reconstruction of a specimen subjected to 100 J of impact is shown. (c) The photograph and (b) EIT map of a specimen subjected to 140 J of impact is also shown.

addition, the normalized conductivity change for the 60 J impact case (Figure 4.14d) is more significant than the 20 J case (Figure 4.14b), which is as expected due to higher magnitudes of plastic deformation. The top films are not discussed here, because the conductivity change is negligible, which is consistent with other studies [58]. One can consider that if this had been a composite aircraft wing, this damage may be invisible to the naked eye and remain undetected for long periods of time.

For the 100 J impact energy case, Figure 4.15a shows that the backside of specimens shows clear signs of visible damage to the outermost layer of the GFRP. This severe damage has also been easily captured by EIT, as can be seen from the EIT reconstruction shown in Figure 4.15b. Furthermore, the specimen that has been subjected to 140 J of impact energy also shows the same type of severe surface damage as shown in Figure 4.15c. Once again, impact damage is successfully captured by the EIT reconstruction of the MWNT-PVDF film, as can be seen from Figure 4.15d. One can observe drastic decreases in normalized conductivity near the vicinity of impact damage. It should be noted that the fracture in the center of the bottom face seems to elicit a spatial conductivity response that is elongated in the vertical direction. This is consistent with the response due to a 6.35 mm hole drilled in the center, as shown in Figure 4.12a.

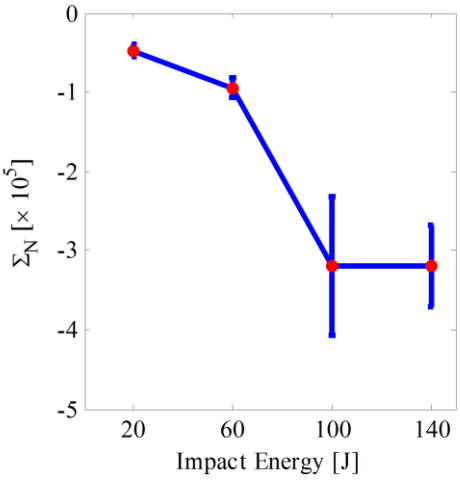

Figure 4.16. The response of the EIT images of embedded MWNT-PVDF films to increasing damage due to impact on several specimens, as indicated by the Σ_N metric.

To quantify the EIT reconstruction results to the various impact events, the Σ_N metric is once again implemented. This time, Ω is specified to be the entire sensing area due to the fact that the damaged area is likely to extend beyond the area of impact. The cumulative results are presented as a mean of the responses from each level of impact energy, which is shown in Figure 4.16. The error bars are calculated as the standard error of the mean. Figure 4.16 shows that the damage metric becomes more negative as impact energy has increased from 20 J and 60 J. On the other hand, a sudden increase in the amount of damage has been observed after the 100 J of impact (and similarly for the 140 J case). This result is expected since a large change in conductivity occurs due to localized fracture, which has already been observed in Figures 4.15a and 4.15c. Since fracture is present in both of the 100 J and 140 J cases, it is not surprising that they exhibit roughly the same amount of damage (*i.e.*, as have been quantified using the damage metric, Σ_N). From these results, it has been demonstrated that EIT spatial conductivity mapping of embedded MWNT-PVDF films is able to detect, locate, and determine the severity of damage induced by impact upon GFRP composites.

4.6 Conclusions

This study serves as a step towards introducing EIT has a next-generation structural health monitoring methodology that can be used in conjunction with MWNT-PVDF films for embedded damage

detection. First, a piezoresistive MWNT-PVDF film assembled using spray fabrication was discussed. The fabrication methodology was scalable and can find applications for deployment onto large structures while still maintaining sensitivity to damage. Second, an electrical impedance tomography (EIT) differential spatial conductivity mapping algorithm was proposed and implemented. However, it was also found that the conductivity distribution of the spray-deposited sensor on unidirectional glass mats was anisotropic in nature. Thus, the conductivity anisotropy was incorporated into the one-step linear MAP reconstruction algorithm as part of EIT. Then, the EIT algorithm was characterized for its resolution and sensitivity to well-defined damage due to different sizes and locations of drilled holes. Additional validation studies were also conducted for verifying the ability of the algorithm to detect various levels of impact damage on GFRP composites. Although more work needs to be conducted prior to their implementation in the field, EIT has potential various structural health monitoring applications.

Chapter 4 References:

[1] Federal Highway Administration (FHWA), "National Bridge Inspection Standards," Federal Highway Administration, ed., 2004, pp. 74419-74439.

[2] V. B. Nakagawara, R. W. Montgomery, G. W. Wood, and J. J. Nichols, "A Demographic Profile of Nondestructive Inspection and Testing (NDI/NDT) Personnel: A Preliminary Report," Federal Aviation Administration, ed., Federal Aviation Administration, 2003.

[3] C. Hautamaki, S. Zurn, S. C. Mantell, and D. L. Polla, "Experimental evaluation of MEMS strain sensors embedded in composites," *Microelectromechanical Systems, Journal of,* vol. 8, no. 3, pp. 272-279, 1999.

[4] A. Kesavan, S. John, and I. Herszberg, "Strain-based Structural Health Monitoring of Complex Composite Structures," *Structural Health Monitoring,* vol. 7, no. 3, pp. 203-213, September 1, 2008, 2008.

[5] A. Cusano, P. Capoluongo, S. Campopiano, A. Cutolo, M. Giordano, F. Felli, A. Paolozzi, and M. Caponero, "Experimental modal analysis of an aircraft model wing by embedded fiber Bragg grating sensors," *Sensors Journal, IEEE,* vol. 6, no. 1, pp. 67-77, 2006.

[6] H. Tsutsui, A. Kawamata, T. Sanda, and N. Takeda, "Detection of impact damage of stiffened composite panels using embedded small-diameter optical fibers," *Smart Materials & Structures,* vol. 13, no. 6, pp. 1284-1290, Dec, 2004.

[7] C. Xinlong, H. Xiangyong, H. Jianghua, and L. Jinjun, "Experimental Research on Embedded Fiber Bragg Grating Sensors Network for Solid Rocket Motors Health Monitor," in First International Conference on Intelligent Networks and Intelligent Systems, Wuhan, China, 2008, pp. 170-173.

[8] Guoliang Jiang, M. Dawood, K. Peters, and S. Rizkalla, "Global and Local Fiber Optic Sensors for Health Monitoring of Civil Engineering Infrastructure Retrofit with FRP Materials," *Structural Health Monitoring,* vol. 9, no. 4, pp. 309-322, July 1, 2010, 2010.

[9] M. P. Wenger, P. Blanas, R. J. Shuford, and D. K. Das-Gupta, "Acoustic emission signal detection by ceramic/polymer composite piezoelectrets embedded in glass-epoxy laminates," *Polymer Engineering & Science,* vol. 36, no. 24, pp. 2945-2954, 1996.

[10] F. Ciampa, and M. Meo, "Impact detection in anisotropic materials using a time reversal approach," *Structural Health Monitoring,* vol. 11, no. 1, pp. 43-49, January 1, 2012, 2012.

[11] H.-Y. Tang, C. Winkelmann, W. Lestari, and V. La Saponara, "Composite Structural Health Monitoring Through Use of Embedded PZT Sensors," *Journal of Intelligent Material Systems and Structures,* vol. 22, no. 8, pp. 739-755, 2011.

[12] V. Giurgiutiu, and A. Zagrai, "Damage Detection in Thin Plates and Aerospace Structures with the Electro-Mechanical Impedance Method," *Structural Health Monitoring,* vol. 4, no. 2, pp. 99-118, June 1, 2005, 2005.

[13] F. Aymerich, and W. J. Staszewski, "Experimental Study of Impact-Damage Detection in Composite Laminates using a Cross-Modulation Vibro-Acoustic Technique," *Structural Health Monitoring,* vol. 9, no. 6, pp. 541-553, November 1, 2010, 2010.

[14] C. Winkelmann, H.-Y. Tang, and V. La Saponara, "Influence of Embedded Structural Health Monitoring Sensors on the Mechanical Performance of Glass/Epoxy Composites," in SAMPE 2008, Long Beach, CA, USA, 2008.

[15] M. Taya, W. Kim, and K. Ono, "Piezoresistivity of a short fiber/elastomer matrix composite," *Mechanics of materials,* vol. 28, no. 1-4, pp. 53-59, 1998.

[16] A. Todoroki, and J. Yoshida, "Electrical Resistance Change of Unidirectional CFRP Due to Applied Load," *JSME International Journal Series A Solid Mechanics and Material Engineering,* vol. 47, no. 3, pp. 357-364, 2004.

[17] S. Wang, and D. Chung, "Piezoresistivity in continuous carbon fiber polymer-matrix composite," *Polymer Composites,* vol. 21, no. 1, pp. 13-19, 2000.

[18] S. Wang, and D. Chung, "Negative piezoresistivity in continuous carbon fiber epoxy-matrix composite," *Journal of Materials Science,* vol. 42, no. 13, pp. 4987-4995, 2007.

[19] H. Inoue, and K. Ogi, "Piezoresistance Behaviour of CFRP Cross-Ply Laminates with Transverse Cracking," *Key Engineering Materials,* vol. 334, no. 2, pp. 961, 2007.

[20] K. Ogi, "A Model for Piezoresistance Behavior in a CFRP Cross-Ply Laminate with Transverse Cracking," *Journal of Solid Mechanics and Materials Engineering,* vol. 1, no. 8, pp. 975-985, 2007.

[21] S. Wang, and D. D. L. Chung, "Self-sensing of flexural strain and damage in carbon fiber polymer-matrix composite by electrical resistance measurement," *Carbon,* vol. 44, no. 13, pp. 2739-2751, 2006.

[22] D.-C. Seo, and J.-J. Lee, "Damage detection of CFRP laminates using electrical resistance measurement and neural network," *Composite Structures,* vol. 47, no. 1–4, pp. 525-530, 1999.

[23] A. Todoroki, M. Tanaka, and Y. Shimamura, "Electrical resistance change method for monitoring delaminations of CFRP laminates: effect of spacing between electrodes," *Composites Science and Technology,* vol. 65, no. 1, pp. 37-46, 2005.

[24] E. D. Minot, Y. Yaish, V. Sazonova, J.-Y. Park, M. Brink, and P. L. McEuen, "Tuning Carbon Nanotube Band Gaps with Strain," *Physical review letters,* vol. 90, no. 15, pp. 156401, 2003.

[25] S. Peng, J. O'Keeffe, C. Wei, K. Cho, J. Kong, R. Chen, N. Franklin, and H. Dai, "Carbon nanotube chemical and mechanical sensors," in 3rd International Workshop on Structural Health Monitoring, Stanford, CA, USA, 2001, pp. 1142-1148.

[26] T. W. Tombler, C. Zhou, L. Alexseyev, J. Kong, H. Dai, L. Liu, C. Jayanthi, M. Tang, and S. Y. Wu, "Reversible electromechanical characteristics of carbon nanotubes under local-probe manipulation," *Nature,* vol. 405, no. 6788, pp. 769-772, 2000.

[27] F. H. Gojny, and K. Schulte, "Functionalisation effect on the thermo-mechanical behaviour of multi-wall carbon nanotube/epoxy-composites," *Composites Science and Technology,* vol. 64, no. 15, pp. 2303-2308, 2004.

[28] P. C. Ma, J. K. Kim, and B. Z. Tang, "Effects of silane functionalization on the properties of carbon nanotube/epoxy nanocomposites," *Composites Science and Technology,* vol. 67, no. 14, pp. 2965-2972, 2007.

[29] C. Martin, J. Sandler, M. Shaffer, M. K. Schwarz, W. Bauhofer, K. Schulte, and A. Windle, "Formation of percolating networks in multi-wall carbon-nanotube–epoxy composites," *Composites Science and Technology,* vol. 64, no. 15, pp. 2309-2316, 2004.

[30] J. Sandler, J. Kirk, I. Kinloch, M. Shaffer, and A. Windle, "Ultra-low electrical percolation threshold in carbon-nanotube-epoxy composites," *Polymer,* vol. 44, no. 19, pp. 5893-5899, 2003.

[31] M. H. G. Wichmann, J. Sumfleth, B. Fiedler, F. Gojny, and K. Schulte, "Multiwall carbon nanotube/epoxy composites produced by a masterbatch process," *Mechanics of Composite Materials,* vol. 42, no. 5, pp. 395-406, 2006.

[32] Z. Yaping, Z. Aibo, C. Qinghua, Z. Jiaoxia, and N. Rongchang, "Functionalized effect on carbon nanotube/epoxy nano-composites," *Materials Science and Engineering: A,* vol. 435, pp. 145-149, 2006.

[33] E. T. Thostenson, and T. W. Chou, "Carbon nanotube networks: sensing of distributed strain and damage for life prediction and self healing," *Advanced Materials,* vol. 18, no. 21, pp. 2837-2841, 2006.

[34] L. Böger, M. Wichmann, L. Meyer, and K. Schulte, "Load and health monitoring in glass fibre reinforced composites with an electrically conductive nanocomposite epoxy matrix," *Composites Science and Technology,* vol. 68, no. 7-8, pp. 1886-1894, 2008.

[35] E. T. Thostenson, and T.-W. Chou, "Real-time in situ sensing of damage evolution in advanced fiber composites using carbon nanotube networks," *Nanotechnology,* vol. 19, no. 21, pp. 215713, 2008.

[36] N. D. Alexopoulos, C. Bartholome, P. Poulin, and Z. Marioli-Riga, "Structural health monitoring of glass fiber reinforced composites using embedded carbon nanotube (CNT) fibers," *Composites Science and Technology,* vol. 70, no. 2, pp. 260-271, Feb, 2010.

[37] B. R. Loyola, V. La Saponara, and K. J. Loh, "In Situ Strain Monitoring of Fiber-Reinforced Polymers using Embedded Piezoresistive Nanocomposites," *Journal of Material Science,* vol. 45, no. 24, pp. 6786-6798, 2010.

[38] A. P. Calderon, "On an inverse boundary value problem," *Comp. Appl. Math,* vol. 25, no. 2-3, pp. 133-138, 2006.

[39] M. Cheney, D. Isaacson, J. Newell, S. Simske, and J. Goble, "NOSER: An algorithm for solving the inverse conductivity problem," *International Journal of Imaging Systems and Technology,* vol. 2, no. 2, pp. 66-75, 1990.

[40] A. Adler, and R. Guardo, "Electrical impedance tomography: regularized imaging and contrast detection," *IEEE Transactions on Medical Imaging,* vol. 15, no. 2, pp. 170-179, 1996.

[41] T. J. Yorkey, J. G. Webster, and W. J. Tompkins, "Comparing reconstruction algorithms for electrical impedance tomography," *IEEE Transactions on Biomedical Engineering*, no. 11, pp. 843-852, 1987.

[42] P. Hua, E. J. Woo, J. G. Webster, and W. J. Tompkins, "Iterative reconstruction methods using regularization and optimal current patterns in electrical impedance tomography," *IEEE Transactions on Medical Imaging,* vol. 10, no. 4, pp. 621-628, 1991.

[43] N. Polydorides, W. R. B. Lionheart, and H. McCann, "Krylov subspace iterative techniques: on the detection of brain activity with electrical impedance tomography," *IEEE Transactions on Medical Imaging,* vol. 21, no. 6, pp. 596-603, 2002.

[44] M. Vauhkonen, "Electrical impedance tomography and prior information," Department of Physics, University of Kuopio, University of Kuopio, 1997.

[45] N. Polydorides, "Image Reconstruction Algorithms For Soft-Field Tomography," Department of Electrical Engineering and Electronics, University of Manchester Institute of Science and Technology, Manchester, United Kingdom, 2002.

[46] B. Abdellatif El, "Inverse source problem in an anisotropic medium by boundary measurements," *Inverse Problems,* vol. 21, no. 5, pp. 1487, 2005.

[47] J. F. P. J. Abascal, S. R. Arridge, D. Atkinson, R. Horesh, L. Fabrizi, M. De Lucia, L. Horesh, R. H. Bayford, and D. S. Holder, "Use of anisotropic modelling in electrical impedance tomography; Description of method and preliminary assessment of utility in imaging brain function in the adult human head," *Neuroimage,* vol. 43, no. 2, pp. 258-268, 2008.

[48] K. J. Loh, T. C. Hou, J. P. Lynch, and N. A. Kotov, "Carbon Nanotube Sensing Skins for Spatial Strain and Impact Damage Identification," *Journal of Nondestructive Evaluation,* vol. 28, no. 1, pp. 9-25, 2009.

[49] T. Hou, K. Loh, and J. Lynch, "Spatial conductivity mapping of carbon nanotube composite thin films by electrical impedance tomography for sensing applications," *Nanotechnology,* vol. 18, no. 31, pp. 315501, 2007.

[50] S. Pyo, K. J. Loh, T. C. Hou, E. Jarva, and J. P. Lynch, "A wireless impedance analyzer for automated tomographic mapping of a nanoengineered sensing skin," *Smart Structures and Systems,* vol. 8, no. 1, pp. 139-155, 2011.

[51] R. Lazarovitch, D. Rittel, and I. Bucher, "Experimental crack identification using electrical impedance tomography," *NDT and E International,* vol. 35, no. 5, pp. 301-16, 2002.

[52] H. Alirezaei, A. Nagakubo, and Y. Kuniyoshi, "A highly stretchable tactile distribution sensor for smooth surfaced humanoids," in 7th IEEE-RAS International Conference on Humanoid Robots, Pittsburgh, Pennsylvania, USA, 2007, pp. 167-173.

[53] H. Alirezaei, A. Nagakubo, and Y. Kuniyoshi, "A tactile distribution sensor which enables stable measurement under high and dynamic stretch," in IEEE Symposium on 3D User Interfaces, Lafayette, Louisiana, USA, 2009, pp. 87-93.

[54] K. Paulson, W. Breckon, and M. Pidcock, "Electrode modelling in electrical impedance tomography," *SIAM Journal on Applied Mathematics*, pp. 1012-1022, 1992.

[55] B. Graham, and A. Adler, "Objective selection of hyperparameter for EIT," *Physiological measurement*, vol. 27, no. S65, 2006.

[56] M. J. O'Connell, P. Boul, L. M. Ericson, C. Huffman, Y. Wang, E. Haroz, C. Kuper, J. Tour, K. D. Ausman, and R. E. Smalley, "Reversible water-solubilization of single-walled carbon nanotubes by polymer wrapping," *Chemical Physics Letters*, vol. 342, no. 3, pp. 265-271, 2001.

[57] I. Mazov, V. Kuznetsov, S. Moseenkov, A. Ishchenko, A. Romanenko, O. Anikeeva, T. Buryakov, E. Y. Korovin, V. Zhuravlev, and V. Suslyaev, "Electrophysical and Electromagnetic Properties of Pure MWNTs and MWNT/PMMA Composite Materials Depending on Their Structure," *Fullerenes, Nanotubes, and Carbon Nanostructures*, vol. 18, no. 4-6, pp. 505-515, 2010.

[58] T.-W. Shyr, and Y.-H. Pan, "Impact resistance and damage characteristics of composite laminates," *Composite Structures*, vol. 62, no. 2, pp. 193-203, 2003.

Chapter 5: Conclusion

The work performed described in this dissertation has progressed the discipline of structural health monitoring (SHM) by presenting an improved methodology for performing spatial detection of damage using electrical impedance tomography (EIT). This sensitivity to damage was enabled by the application of piezoresistive MWNT-PSS/PVA and MWNT-PVDF films to and within glass fiber-reinforced polymer (GFRP) composites. Although, these deposition methods allow for the application of these films to almost any structural material. Furthermore, this work focused on demonstrating the detection, location, and severity determination of damage in GFRP composites. The description of this work was structured to illustrate the main thrusts performed to advance the use of spatially distributed electrical conductivity for structural health monitoring for GFRP composites.

In chapter 2, a characterization of the sensitivity of MWNT-PSS/PVA thin films to mechanical loading was discussed. Using a layer-by-layer depositional method, the thin films were manufactured with tailorable electrical properties directly on GFRP substrates. These films were characterized for the change of their electrical properties to mechanical loading using time-domain DC resistance measurements and frequency-domain electrical impedance spectroscopy measurements. Monotonic and dynamic loading was performed on GFRP substrates with the deposited thin films, while the films were probe with the two measurement methods. Bi-functional strain sensitivity was found in the electrical response, where a linear response was followed by a quadratic response. It was proposed that the linear response was due to MWNT stretching, and the quadratic response was due to the tearing of the film due to cracking in the underlying substrate, as shown using scanning electron microscope images. Furthermore, the films were tested for their response to changes in environmental conditions, including temperature and humidity. The response of the films was found to be highly non-linear to both conditions, and these responses were characterized using

appropriate models. The work performed in this chapter proved that MWNT thin films were sensitive to both strain and damage, while characterizing any environmental sensitive as well.

In chapter 3, a new carbon nanotube-based film was formulated and used in conjunction with electrical impedance tomography to demonstrate the ability to perform spatially distributed sensing. The development of a new film was necessary due to limitations in the layer-by-layer depositional methodology, which restricted the size of the area over which the film could be deposited. The new film, made from a latex-base of PVDF sub-microparticles and MWNTs, was demonstrated to be easy to apply over large areas using a spray deposition. Using areas of spatially patterned conductive films, a linear EIT algorithm called Maximum a Posteriori was implemented to detect differences in conductivity patterns between specimens. This algorithm proved to be vastly faster than the iterative solvers previously applied to EIT conductivity reconstructions for SHM applications. Finally, the films were characterized for their sensitivity to applied strain using EIT. Compressive and tensile strain was subjected to MWNT-PVDF films deposited on GFRP specimens using 4-pt bending. The EIT response was linear from -5,000 με to 4,000 με. These responses were nearly identical to those measured using 2-pt probe resistance measurements for MWNT-PVDF films placed into the same levels of tension. This initial EIT study demonstrated the spatial sensing capability of the EIT measurements on the MWNT-PVDF films.

In chapter 4, the MWNT-PVDF films were deposited directly onto the top and bottom plies of fiber mats that were embedded within the GFRP composites. Due to the fiber orientation, the conductivity was anisotropic in nature and was accounted for in an altered form of the MAP algorithm. The sensitivity of this revised algorithm and the embedded films were characterized by drilling progressively larger holes in the center of one of the sensing areas, while taking EIT measurements. Furthermore, the sensitivity of the films to multiple points of damage was determined using an array of similarly sized holes across a sensing area. Finally, specimens with embedded film were subjected to impact events with energies of 20 J, 60 J, 100 J, and 140 J. It was demonstrated that the EIT measurements were fully capable of detecting, locating and determining the severity of the damage caused by the impact events.

In conclusion, this work has further enabled a shift in the structural health monitoring paradigm towards spatial sensing using applied or embedded piezoresistive films. The reconstruction algorithm implemented in this work allows for nearly real-time reconstructions that take about one second to perform.

By embedding the MWNT-PVDF films, nearly invisible damage within the structure of GFRP composites can now be detected. Despite these successes, further work needs to be performed to improve the anisotropic models available for taking the fiber structure into account. To be able to perform EIT on each layer of a composite structure, new methods will need to be developed to allow for electrical connectivity with the boundary electrodes that will be fully embedded and encapsulated in epoxy. The innovations introduced in this work and that of the future will eventually allow for spatial sensing systems that will be ready for full field deployment.

Distributed In Situ Health Monitoring of Conductive Self-Sensing Fiber-Reinforced Polymers Using Electrical Impedance Tomography

By

Bryan Richard Loyola
B.S. (University of California, Davis) 2005
M.S. (University of California, Davis) 2010

DISSERTATION

Submitted in partial satisfaction of the requirements for the degree of

DOCTOR OF PHILOSOPHY

in

Mechanical and Aeronautical Engineering

in the

OFFICE OF GRADUATE STUDIES

of the

UNIVERSITY OF CALIFORNIA

DAVIS

Approved:

_____
Valeria La Saponara, Co-Chair

_____
Kenneth J. Loh, Co-Chair

_____
David A. Horsley

_____
Frank Yaghmaie

_____
Jack L. Skinner

Committee in Charge

2010

Chapter 1: Introduction

1.1 The Trillion Dollar Problem

With the numerous advances of the 20th century, the world has a complex infrastructure that is aging, which is depended on for transportation, communication, defense, health protection, and many other purposes. At the present, engineers are being increasingly tasked with the job of ensuring the structural integrity of this infrastructure. Numerous governmental agencies and professional engineering societies have spent an extraordinary amount of time establishing standards and estimates to accomplish these goals. As an example, American Society of Civil Engineers periodically publishes a report card on United States' civil infrastructure and the associated near-term costs to bring this infrastructure to acceptable standards. The 2009 report card issued a general "D" rating for our overall infrastructure with dams, levees, and hazardous waste facilities rating as among in the worst condition [1]. Over the next 5 years, they estimate that $2.2 trillion will need to be invested to bring our infrastructure to a "B" rating. The report continues to project that only half of that money will be allocated in governmental budgets [1]. In addition to civil infrastructure, our aircraft infrastructure requires costly maintenance and monitoring. In 2007, the aircraft maintenance and overhaul industry was worth about $45 billion for both commercial and defense assets. Furthermore, a recent report cited the cost of the entire cost of the United States' F-35 Joint Strike Fighter program to cost $1.45 trillion over its 50-year projected lifetime, with $1.11 trillion in maintenance and operational costs [2]. It is obvious that this is a very serious trillion US dollar problem.

Not unlike how maintenance is performed on an automobile, maintenance is performed on most of our infrastructure at specific time points or life-cycle events, like the number of miles driven in a car. Specifically, the Federal Highway Administration (FHA) requires that all vehicular public bridges within the United States be inspected every 24 months and underwater components checked every 60 months [3].

Due to FHA guidelines, these bridges are predominantly visually inspected [4], which is a time consuming and laborious task. In addition to bridge monitoring, civilian aircraft are required to be inspected based on time and flight-cycle (one lift-off and landing) requirements that are established in conjunction with the Federal Aviation Administration [5]. The required maintenance schedules become more intensive for longer timespans and accumulating flight-cycles, with the most intensive maintenance requiring to a complete teardown of the plane for intensive evaluation [6]. During these maintenance schedules, the aircraft are inspected primarily using visual inspection, but other non-destruction evaluation (NDE) methods are used at a lesser rate [7]. With the most intensive "D-check" inspection taken taking weeks [8], this can accumulate to a high loss of revenue for airlines.

To alleviate some of the time and costs associated with these extensive maintenance approaches, it is desired to implement sensors that can detect the presence of damage within a structure. This would allow for a paradigm shift from time/cycle-based maintenance towards condition-based maintenance. Distributed sensors could indicate that a concrete member in a bridge or lap-joint in an aircraft is cracking, necessitating action. In addition, some components are replaced based on the same criteria as maintenance, which can lead to replacing component that still has sufficient service life remaining. This adds cost to structural operations that can be reduced via sufficient monitoring. The weeks-long "D-checks" could be performed in a matter of minutes or hours, if an aircraft were fully instrumented with sensors that are capable of performing the tasks conducted during these checks. With this in mind, the research area of structural health monitoring has been focused on innovating and implementing many of these desired sensing methodologies [9].

1.2 Fiber-Reinforced Polymer Composites

Over the past 50 years, the use of fiber-reinforced polymer (FRP) composites has drastically increased in structural parts of aircraft, wind turbines, naval vessels, unmanned aerial vehicles, automobiles, and civil infrastructure. One example is the Boeing 787, which is constructed of over 50 wt.% of FRP materials [10]. The first of these aircraft was delivered to All Nippon Airlines, in October 2011. The reason for this increased usage is partly due to FRP's high strength-to-weight ratios, corrosion and fatigue resistance, and high conformability. Despite these characteristics, FRPs are still susceptible to damage from sources like overloading, impact events, chemical penetration, and multi-axial fatigue, to

name a few. These events can invoke damage responses from composite materials in a variety of modes, including delamination, fiber- and/or matrix breakage, fiber-matrix disbonding, matrix swelling. Due to their laminate structure, these damage modes tend to manifest internally to the composite part, making this damage nearly invisible. As the main method of aircraft monitoring is based on visual inspection, this presents a concern. In fact, this nearly invisible damage has caused incidents in the past, for example in the Airbus A-300 series aircraft. In one case, one of these aircraft was flying towards Ontario, Canada from Cuba, when its rudder fully detached from the aircraft. The resulting U.S./Canadian investigation determined that hydraulic fluid in the rudder had weakened the epoxy bond of the carbon fiber composite to the point that the rudder did not have sufficient structural integrity and failed [11]. Due to this nearly invisible damage, new structural health monitoring approaches need to be developed to detect damage in composite materials.

1.3 Structural Health Monitoring – The State of the Art

To lower the cost of inspecting our current infrastructure, many research groups have developed the groundwork for systems that can be deployed throughout a structure to detect the presence of damage. In addition, many groups have focused their attention on creating system for damage detection in FRP composites. Of these groups, some have even gone as far as to take advantage of the layered architecture of composites for embedding their sensing approaches within the structure for in situ measurements. These sensing methodologies include foil-based strain gauges, fiber-optic systems, acoustic and ultrasonic-based approaches, and electrical property-based detection.

1.3.1 Foil-based Strain Gauge Sensing

Foil-based strain gauges have been used for materials and structural characterization for a long time and are a mainstay in most mechanical research labs. Based on a metallic-foil that is deposited on a thin substrate, the resistance across the foil changes with applied strain [12]. This effect is called piezoresistivity. For structural health monitoring, the general approach is that an initial strain field is mapped based on some representative loading. Later, deviations from this strain field due to analogous loading can lead to a detection of damage and determination of location. Many groups have deployed networks of these sensors to measure the strain field in structures to detect damage in railroad rails [13], bridges [14], military fighter aircraft [15], and wind turbine blades [16], to name a few. In addition, other

groups have embedded these strain gauges within the structure of FRP composites for in situ monitoring of damage [17, 18]. The downside of these systems is that each sensors needs to be wired separately, so weight and cost from instrumentation can be a problem.

1.3.2 Fiber-Optic Sensing

Other researchers have used fiber-optic-based strain sensors instead of the foil-based variety. This sensing is accomplished by embedding a Bragg grating within an optical fiber. These gratings are alternating segments of the fiber with different refractive indexes, which causes a certain wavelength, called the Bragg wavelength, of light to be reflected [19]. When the gratings are subjected to strain, the gratings reflect at a shifted wavelength. If several gratings are placed in succession along a fiber with different Bragg wavelengths, a multi-wavelength light source can be used to monitor strain at several locations with one fiber. This lowers the cabling overhead necessary when compared to foil-based strain sensors. However, as the Bragg gratings measure strain, they are sensitive to thermal changes as well due to the coefficient of thermal expansion of the fiber material. To delineate between the strain sources, a temperature sensor needs to be implemented in conjunction with the fiber-Bragg gratings. Foil-based strain sensors have this same problem, as well. Fiber-Bragg gratings have been used in numerous applications, with most using multiple Bragg sensors per fiber. Some examples include monitoring bridges [20], rocket motors [21], and aircraft [22]. In addition, several research groups embedded these fibers within the laminate architecture of FRP composites for in situ monitoring [21, 23-28]. There are a few drawbacks to embedding the fiber optics within a composite. First, research has found that fibers with diameters larger than 100 mm can act as a crack initiator, thus shortening the service life of the composite structure [27]. Second, many optical fibers are made out of glass, which is brittle. This can lead to difficulties with fiber breakage during manufacturing, before the system can ever be tested. Once a fiber has broken, the system is difficult to repair.

1.3.3 Acoustic and Ultrasonic-based Sensing

Wave propagation structural health monitoring is based on the measurement of stress waves passing through a structure, at frequencies ranging from 20 Hz to 20 kHz (acoustic range) or above (ultrasonic, from 20 kHz up to ~200 MHz). Unlike the previous methods, sensing of damage happens away from the application point of the sensors. Transducers are typically based on piezoelectric materials, which

produce a voltage when they are subjected to a strain, or vice versa. This allows piezoelectric materials to be both actuators and sensors, and can be used in passive or active systems.

Passive systems have several sensors distributed across a structure and wait for a stress wave to be produced from a damage-like event, like the formation of a crack. The signal is captured by the sensors, and the time difference between the arrivals of the signal may be used to determine the location of the damage event. In addition, the detected signal is analyzed to determine the kind of damage that created it and the relative severity. Acoustic emission techniques have been used in bridge monitoring [29], wind turbines [30], and spacecraft [31]. Specifically for monitoring composite materials, other groups have embedded acoustic emission and ultrasonic sensors using piezoelectric sensors [32] and fiber-optic sensors [33] for detection.

Active sensing uses both an actuator and a sensor for detecting damage. In the pitch-catch method, an actuator creates the strain waves and other sensors, placed elsewhere on the structure, sense the propagated waves. This detection is based on how the propagated waves change as they pass through or are deflected by the damage. In the pulse-echo method, one transducer performs as both the actuator and the sensor. First, the transducer creates a strain wave. Then, the transducer is changed into a sensor and waits to detect the propagated wave to be reflected from the presence of damage or the boundaries of the structure. Several of these transducers are placed across a structure to determine the location and size of the damage. Extensive work has been done in this are with some systems tried on space structures [34], fast patrol boats [35], naval structures [36], and aircraft structures [37]. Other work has shown that active sensing can be used in composite structures as well [38-41], although the propagation of the stress waves is complex due to the anisotropic nature of composites. In fact, work has been done that involves embedding the piezoelectric transducers within the composite structure, between the plies [42, 43]. However, research has shown that the placement of the piezoelectric transducers on the surface or within a composite material can cause stress concentrations. These stresses can lead to the onset of cracking, eventually decreasing the structural integrity of the composite structure [44].

1.3.4 Two-point Electrical Sensing

Another approach taken for damage detection is monitoring for changes in electrical properties to indicate the presence of damage. This approach has been conducted in two ways: measuring changes in

inherent electrical conductivity of a structure or measuring changes in the electrical conductivity of an applied conductive film. The former approach has become a popular approach in monitoring conductive carbon fiber reinforced polymers (CFRPs), and the latter approach has been implemented for non-conductive composite materials, and for application in materials with conductivities that do not respond significantly to mechanical loading or damage.

In addition to being conductive, CFRP composites have been shown to be piezoresistive (*i.e.* resistance changes with applied strain). This change in resistance is typically measured in the direction of applied loading, or in the longitudinal direction for typical tensile loading specimens. Several groups have characterized the piezoresistivity of many types of CFRP composites [45-49]. In general, the resistance response to applied strain is linear in nature. However, deviations from this linearity has been found to be due to transverse cracking in the composites [46]. Other groups have focused on detecting fatigue damage [50-52]. In this work, repeated loadings weakened the carbon fibers, leading to fiber breakage and increases in resistance. Additionally, Seo and Lee [51] were able to create a model based on a neural network to correlate a change in the resistance measurements to a reduction in stiffness of the CFRP composite specimens. Other research has shown that changes in electrical resistance can be used to detect delamination [53, 54]. Typically, these resistance measurements are taken through-the-thickness to orient the possible damage transverse to the measurement direction, increasing sensitivity. By using the inherent electrical properties of CFRP composites, many of the damage modes demonstrated by composite materials can be detected.

When the electrical properties of the structure are not desirable for use for damage detection, the application of a conductive film has been performed to accomplish this task. Due to the many desirable properties of carbon nanotubes, these conductive nanoparticles have been incorporated into structures to impart electrical conductivity for sensing purposes. Carbon nanotubes (CNTs) are rolled, concentric cylinders of graphene sheets, which have diameters in a range from 1 to 100 nm and aspect ratios up to the millions [55]. These nanoparticles have semi-conducting and metallic electrical properties based on the orientation of these sheets and the number of the concentric cylinders [56]. In addition to electrical conductivity, CNTs have been found to be piezoresistive [57-59]. To take advantage of these properties, they have been incorporated into structures via neat CNT thin films and polymer-based nanocomposites.

A neat CNT thin film is only composed of carbon nanotubes, which are bound together via the very strong carbon-carbon bond [60]. These films are typically manufactured by dispersing the CNTs in a polar solvent, such as dimethylformamide (DMF), and then filtering the solution to create a mat of the CNTs. These buckypapers have been predominantly characterized for their piezoresistivity [60-63]. Although piezoresistive, these films have been found to be rather brittle in nature [60], which could possibly lead to the sensor failing at higher strain levels prior to the structure failing.

Another approach to utilize the characteristics of CNTs is to incorporate them within a polymer matrix, called a nanocomposite. Primarily, this has been done two ways: as a thin film [60, 64-69] or as a bulk polymer nanocomposite [70-77]. Despite the method, the addition of CNTs not only imparts a conductivity to the non-conductive polymer matrix, but has also been found to lead to higher mechanical properties, in some cases [78]. These nanocomposites have been extensively characterized for their damage detection capabilities that can be applied to or incorporated into a structure. In these conductive nanocomposites, the piezoresistivity of the CNTs is still present, and many have found thin films exhibiting a bi-functional response to applied strain. This bi-functional response is typically initially linear, due to the piezoresistivity of the CNTs, and then becomes non-linear due to cracking of the thin film [66, 67, 76]. In the cases where a thin film was deposited directly upon the glass fibers in a GFRP composite, embedded sensing was enabled and capable of capturing this non-linear changes in resistance due to transverse cracking [66]. On the other hand, CNTs that are dispersed into epoxy can be infused throughout glass fiber weaves to create a conductive GFRP composites, which have been characterized for their strain and damage sensitivities [73, 76, 79]. Regardless of the approach towards incorporation of CNTs, doing so leads to a sensor that can be deposited or embedded within many structures.

1.3.5 Conclusions

At the present, great strides have been made to bring structural health monitoring methodologies to numerous structures, including naval vessels, aircraft, bridges, wind turbines, and many others. Despite these successes, there are drawbacks to these methods. Foil- and fiber Bragg grating-based strain sensors are point-based sensors that have high strain sensitivity at the point of application. However, to determine the strain away from these placement points, interpolation methods need to employed to a densely instrumented network of these sensors. This can lead to a high cost and weight overhead that is not

desirable for many applications, like in aircraft. Wave propagation-based methods (in acoustic and ultrasonic ranges) have the opposite problem, where their sensitivity is much higher away from the point of application. This is particularly true for the pulse-echo configuration; because the actuated wave needs to be given time to leave the transducer before it can be switched to receiving mode. In addition, components of active systems can be really heavy, although advances by various groups are mitigating this problem [80, 81]. In relation to the electrical resistance-based sensing of inherent or imparted electrical conductivity, these approaches are excellent at sensing applied strain and incurred damage. However, these measurements do not allow for the location of the resistance changing phenomenon to be resolved.

1.4 Electrical Impedance Tomography

For the past 30 years, research has been conducted in developing an electromagnetic imaging modality called electrical impedance tomography (EIT). EIT is a soft-tomographic method that can reconstruct the spatial distribution of electrical conductivity within a set of boundary electrodes. EIT is performed by propagating a current between two of the boundary electrodes, and differential voltage measurements are taken between the remaining adjacent electrodes. This is done for several current injections to create a full EIT measurement. These measurements are then used to perform the conductivity distribution reconstruction. This reconstruction is inherently ill-posed, meaning that the number of boundary voltage measurements is less than the number of conductivity variables to be solved. Due to this, a stable reconstruction algorithm was not developed until 1980 by Calderon and has since been re-printed in 2006 [82]. Since then, numerous groups have developed additional algorithms for linear [83-86] and non-linear [85, 87-90] conductivity distributions using direct [83, 84, 91] or iterative solvers [92-94]. In general, this research has focused on isotropic conductivity distributions, while others have focused on solving anisotropic conductivity distributions [95-99]. Due to the non-invasive nature of this method, it has been primarily the focus of medical [85, 88] and geophysical [90, 100] applications. Only recently has the SHM community taken notice of EIT. Thus far, groups have investigated detection of strain/impact [101], pH [102], corrosion [103], deformation [104, 105], and cracking [106]. Despite the impressive spatial sensing that has been demonstrated by these studies, there are a few drawbacks that need to be addressed before EIT can be used in the field for SHM. First, most of this work was done using an iterative reconstruction solver that can lead to long processing times, which is not ideal for real-time SHM. Second,

the deposition method used to apply the conductive films can only be manufactured on small scales. To take advantage of spatial sensing capabilities of EIT, the ability to deposit conductive films across large areas of a structure is desired. Third, none of these studies have demonstrated the ability to take advantage of the layered architecture of FRP composites for embedded sensing, where the damage is known to occur in these structures.

1.5 Key Contributions of this Thesis and Conclusions

The work presented in this dissertation focuses on providing the next steps towards embedded, spatially distributed health monitoring of glass fiber-reinforced polymer (GFRP) composites. The research was broken up into three segments, each focusing on an issue facing the implementation of EIT as discussed in the last section. These are each topics of a journal paper, which include:

1. A characterization of a MWNT-polyelectrolyte thin film formed via a layer-by-layer deposition process directly onto the surface of a GFRP composite. These thin films were characterized for their sensitivities to mechanical loading, temperature, and humidity. The results from this study indicated that these thin films are not only strain sensitive but sensitive to incurred damage from transverse cracking. The thin films' sensitivities to temperature and humidity were both found to be non-linear in nature but repeatable.
2. A conductive MWNT-polyvinylidene fluoride (PVDF) film was developed that is able to be spray-deposited over large areas. Sprayed on GFRP composite substrates, EIT measurements were performed on these films to characterize a direct (one-step) linear reconstruction algorithm called Maximum a Posteriori (MAP). To validate the algorithm, specific patterns of MWNT-PVDF conductive films were deposited on GFRP substrates to be imaged with EIT. The corresponding reconstructions were compared to the conductivity distributions measured by distributed 4-pt probe measurements. In addition, the strain sensitivity of the MWNT-PVDF films on a GFRP substrates was characterized with 2-pt probe resistance measurements and compared to the sensitivities measured using the EIT method.

3. The MWNT-PVDF films were embedded within GFRP composites, and EIT imaging was performed on these specimens. It was determined that the conductivity was anisotropic, and the MAP algorithm was modified to account for this. A damage sensitivity characterization was performed, by drilling increasingly bigger holes in the center of a specimen. In addition, the spatial sensitivity of the algorithm was determined by drilling 9 holes in a grid in the sensing area. Finally, the change in spatial conductivity distribution due to impact events of specific energies was investigated. This work demonstrated that the EIT reconstructions are capable of detecting, locating, and determining the severity of damage using embedded MWNT-PVDF films.

The work presented in this dissertation shows great promise for the use of EIT for real-time SHM measurements in the field. Due to the sensitivity characterizations of the MAP algorithm, deficiencies in its performance have been noted for possible progress in the future. In addition, the MAP algorithm has drastically increased the time for which the spatial conductivity reconstructions can be performed, with the MAP reconstructions taking about one second to perform. To enable this sensing methodology, it was determined that the deposition method for the MWNT-polyelectrolyte films would be a limiting factor in manufacturing a sensing area to use with EIT. For this reason, a MWNT-PVDF film was developed that has the ability to be deposited at area scales to be of use in the real world. Finally, by demonstrating the ability to embed the MWNT-PVDF films inside the GFRP, future work will be able to perform structural health monitoring throughout each ply in a GFRP composite laminate at a time-scale capable of real-time monitoring.

Chapter 1 References:

[1] American Society of Civil Engineers, *2009 Report Card for America's Infrastructure*, 2009.
[2] A. Shalal-Esa, "U.S. Sees Lifetime Cost of F-35 Fighter at $1.45 Trillion," *Reuters*, Reuters, 2012.
[3] Federal Highway Administration, "National Bridge Inspection Standards," *23 CFR Part 650*, Department of Transportation, ed., Federal Register, 2004.
[4] M. Moore, D. Rolander, B. Graybeal, B. Phares, and G. Washer, "Highway Bridge Inspection: State-of-the-Practice Study," Federal Highway Administration, ed., Department of Transportation, 2001.
[5] Federal Aviation Administration, "Maintenance Review Board Report Maintenance Type Board, and OEM/TCH Inspection Program Procedures," Department of Transportation, ed., John M. Allen, 2010.
[6] Flight Standards Service, "Inspection Fundamentals," *Aviation Maintenance Technician Handbook*, Federal Aviation Administration, ed., Oklahoma City, OK: F.A.A. Airmen Testing Standards Branch, 2008.

[7] Federal Aviation Administration, "AC 43-204 - Visual Inspection for Aircraft," Department of Transportation, ed., Richard O. Gordon, 1997.

[8] Luftansa Technik. "Aircraft maintenance at Lufthansa Technik," June 21, 2012; http://www.lufthansa-technik.com/applications/portal/lhtportal/lhtportal.portal?requestednode=405&_pageLabel=Template5_6&_nfpb=true&webcacheURL=TV_I/Media-Relations-new/Background---Specials/In-Focus/Maintenance---Overhaul/Aircraft_maintenance.xml.

[9] C. Boller, F. K. CHANG, and Y. Fujino, *Encyclopedia of Structural Health Monitoring*, Hoboken, NJ: Wiley, 2009.

[10] B. Roeseler, B. Sarh, M. Kismarton, J. Quinlivan, J. Sutter, and D. Roberts, "Composite Structures – The First 100 Years," in Composite Design Tutorial, Stanford University, 2009.

[11] M. V. Rosenker, "Safety Recommendation A-06-27 and -28," National Transportation Safety Board, ed., 2006.

[12] Omega Engineering Inc. "The Strain Gauge," June 21, 2012; http://www.omega.com/literature/transactions/volume3/strain.html.

[13] D. Barke, and W. Chiu, "Structural health monitoring in the railway industry: a review," *Structural Health Monitoring,* vol. 4, no. 1, pp. 81-93, 2005.

[14] T. H. T. Chan, Z. X. Li, and J. M. Ko, "Fatigue analysis and life prediction of bridges with structural health monitoring data — Part II: application," *International Journal of Fatigue,* vol. 23, no. 1, pp. 55-64, 2001.

[15] S. R. Hunt, and I. G. Hebden, "Validation of the Eurofighter Typhoon structural health and usage monitoring system," *Smart Materials and Structures,* vol. 10, no. 3, pp. 497, 2001.

[16] M. A. Rumsey, and J. A. Paquette, "Structural Health Monitoring of Wind Turbine Blades," in SPIE Smart Structures / NDE, San Diego, CA, USA, 2008.

[17] C. Hautamaki, S. Zurn, S. C. Mantell, and D. L. Polla, "Experimental evaluation of MEMS strain sensors embedded in composites," *Microelectromechanical Systems, Journal of,* vol. 8, no. 3, pp. 272-279, 1999.

[18] A. Kesavan, S. John, and I. Herszberg, "Strain-based Structural Health Monitoring of Complex Composite Structures," *Structural Health Monitoring,* vol. 7, no. 3, pp. 203-213, September 1, 2008, 2008.

[19] G. Meltz, W. W. Morey, and W. H. Glenn, "Formation of Bragg gratings in optical fibers by a transverse holographic method," *Opt. Lett.,* vol. 14, no. 15, pp. 823-825, 1989.

[20] R. C. Tennyson, A. A. Mufti, S. Rizkalla, G. Tadros, and B. Benmokrane, "Structural health monitoring of innovative bridges in Canada with fiber optic sensors," *Smart Materials and Structures,* vol. 10, no. 3, pp. 560, 2001.

[21] C. Xinlong, H. Xiangyong, H. Jianghua, and L. Jinjun, "Experimental Research on Embedded Fiber Bragg Grating Sensors Network for Solid Rocket Motors Health Monitor," in First International Conference on Intelligent Networks and Intelligent Systems, Wuhan, China, 2008, pp. 170-173.

[22] D. Betz, L. Staudigel, and M. N. Trutzel, "Test of a fiber Bragg grating sensor network for commercial aircraft structures." pp. 55-58 vol.1.

[23] M. Amano, Y. Okabe, N. Takeda, and T. Ozaki, "Structural Health Monitoring of an Advanced Grid Structure with Embedded Fiber Bragg Grating Sensors," *Structural Health Monitoring,* vol. 6, no. 4, pp. 309-324, December 1, 2007, 2007.

[24] A. Cusano, P. Capoluongo, S. Campopiano, A. Cutolo, M. Giordano, F. Felli, A. Paolozzi, and M. Caponero, "Experimental modal analysis of an aircraft model wing by embedded fiber Bragg grating sensors," *Sensors Journal, IEEE,* vol. 6, no. 1, pp. 67-77, 2006.

[25] K. Levin, and S. Nilsson, "Examination of reliability of fibre optic sensors embedded in carbon/epoxy composites." p. 222.

[26] R. Measures, "Smart composite structures with embedded sensors," *Composites Engineering,* vol. 2, no. 5, pp. 597-618, 1992.

[27] H. Tsutsui, A. Kawamata, T. Sanda, and N. Takeda, "Detection of impact damage of stiffened composite panels using embedded small-diameter optical fibers," *Smart Materials & Structures,* vol. 13, no. 6, pp. 1284-1290, Dec, 2004.

[28] G. Zhou, and L. Sim, "Damage detection and assessment in fibre-reinforced composite structures with embedded fibre optic sensors-review," *Smart Materials and Structures,* vol. 11, pp. 925-939, 2002.

[29] T. Hay, S. Jayaraman, A. Ledeczi, P. Volgyesi, and R. Hay, "Railway Bridge Structural Health Monitoring Using Wireless Acoustic Emission Sensor Network."

[30] A. Beattie, "Acoustic emission monitoring of a wind turbine blade during a fatigue test," in American Society of Mechanical Engineers Wind Energy Symposium, Reno, NV, USA, 1997, pp. 239-248.

[31] J. Yun, "Development of Structural Health Monitoring Systems Incorporating Acoustic Emission Detection for Spacecraft and Wind Turbine Blades," Electrical and Computer Engineering, Virginia Tech 2011.

[32] M. P. Wenger, P. Blanas, R. J. Shuford, and D. K. Das-Gupta, "Acoustic emission signal detection by ceramic/polymer composite piezoelectrets embedded in glass-epoxy laminates," *Polymer Engineering & Science,* vol. 36, no. 24, pp. 2945-2954, 1996.

[33] R. Ian, F. Peter, and M. Stuart, "Optical fibre acoustic emission sensor for damage detection in carbon fibre composite structures," *Measurement Science and Technology,* vol. 13, no. 1, pp. N5, 2002.

[34] A. Zagrai, D. Doyle, V. Gigineishvili, J. Brown, H. Gardenier, and B. Arritt, "Piezoelectric Wafer Active Sensor Structural Health Monitoring of Space Structures," *Journal of Intelligent Material Systems and Structures,* vol. 21, no. 9, pp. 921-940, 2010.

[35] H. Sohn, C. Farrar, N. Hunter, and K. Worden, *Applying the LANL Statistical Pattern Recognition Paradigm for Structural Health Monitoring to Data from a Surface-Effect Fast Patrol Boat,* vol. LA-13761-MS, Los Alamos National Laboratory, 2001.

[36] S. S. Kessler, E. B. Flynn, and M. D. Todd, "Hybrid Coherent/Incoherent Beam Forming Diagnostic Approach to Naval Assets," 2011.

[37] J. B. Ihn, and F. K. Chang, "Pitch-catch active sensing methods in structural health monitoring for aircraft structures," *Structural Health Monitoring,* vol. 7, no. 1, pp. 5-19, 2008.

[38] F. Chang, J. Markmiller, J. Ihn, and K. Cheng, "A potential link from damage diagnostics to health prognostics of composites through built-in sensors," *Journal of Vibration and Acoustics,* vol. 129, pp. 718, 2007.

[39] S. Kessler, and P. Agrawal, "An Adaptive Pattern Recognition Methodology for Damage Classification in Composite Laminates." pp. 17-19.

[40] H. Park, H. Sohn, K. Law, and C. Farrar, "Time reversal active sensing for health monitoring of a composite plate," *Journal of Sound and Vibration,* vol. 302, no. 1-2, pp. 50-66, 2007.

[41] S. M. Spearing, and S. S. Kessler, "Piezoelectric-based in-situ damage detection of composite materials for structural health monitoring systems," Massachusetts Institute of Technology, 2002.

[42] C. Paget, K. Levin, and C. Delebarre, "Actuation performance of embedded piezoceramic transducer in mechanically loaded composites," *Smart Materials and Structures,* vol. 11, no. 6, pp. 886-891, 2002.

[43] H.-Y. Tang, C. Winkelmann, W. Lestari, and V. La Saponara, "Composite Structural Health Monitoring Through Use of Embedded PZT Sensors," *Journal of Intelligent Material Systems and Structures,* vol. 22, no. 8, pp. 739-755, 2011.

[44] C. Winkelmann, H.-Y. Tang, and V. La Saponara, "Influence of Embedded Structural Health Monitoring Sensors on the Mechanical Performance of Glass/Epoxy Composites," in SAMPE 2008, Long Beach, CA, USA, 2008.

[45] H. Inoue, and K. Ogi, "Piezoresistance Behaviour of CFRP Cross-Ply Laminates with Transverse Cracking," *Key Engineering Materials,* vol. 334, no. 2, pp. 961, 2007.

[46] K. Ogi, "A Model for Piezoresistance Behavior in a CFRP Cross-Ply Laminate with Transverse Cracking," *Journal of Solid Mechanics and Materials Engineering,* vol. 1, no. 8, pp. 975-985, 2007.

[47] M. Taya, W. Kim, and K. Ono, "Piezoresistivity of a short fiber/elastomer matrix composite," *Mechanics of materials,* vol. 28, no. 1-4, pp. 53-59, 1998.

[48] A. Todoroki, and J. Yoshida, "Electrical Resistance Change of Unidirectional CFRP Due to Applied Load," *JSME International Journal Series A Solid Mechanics and Material Engineering,* vol. 47, no. 3, pp. 357-364, 2004.

[49] S. Wang, and D. Chung, "Piezoresistivity in continuous carbon fiber polymer-matrix composite," *Polymer Composites,* vol. 21, no. 1, pp. 13-19, 2000.

[50] J. Abry, S. Bochard, A. Chateauminois, M. Salvia, and G. Giraud, "In situ detection of damage in CFRP laminates by electrical resistance measurements," *Composites Science and Technology,* vol. 59, no. 6, pp. 925-935, 1999.

[51] D.-C. Seo, and J.-J. Lee, "Damage detection of CFRP laminates using electrical resistance measurement and neural network," *Composite Structures,* vol. 47, no. 1–4, pp. 525-530, 1999.

[52] P. Irving, and C. Thiagarajan, "Fatigue damage characterization in carbon fibre composite materials using an electrical potential technique," *Smart Materials and Structures,* vol. 7, no. 4, pp. 456-466, 1998.

[53] A. Todoroki, "Delamination Monitoring Analysis of CFRP Structures using Multi-Probe Electrical Method," *Journal of Intelligent Material Systems and Structures,* vol. 19, no. 3, pp. 291-298, 2008.

[54] A. Todoroki, H. Kobayashi, and K. Matuura, "Application of electric potential method to smart composite structures for detecting delamination," *JSME International Journal, Series A: Mechanics and Material Engineering,* vol. 38, no. 4, pp. 524-530, 1995.

[55] Z. W. Pan, S. S. Xie, B. H. Chang, C. Y. Wang, L. Lu, W. Liu, W. Y. Zhou, W. Z. Li, and L. X. Qian, "Very long carbon nanotubes," *Nature,* vol. 394, no. 6694, pp. 631-632, 1998.

[56] R. Baughman, A. Zakhidov, and W. De Heer, "Carbon nanotubes--the route toward applications," *Science,* vol. 297, no. 5582, pp. 787, 2002.

[57] E. D. Minot, Y. Yaish, V. Sazonova, J. Y. Park, M. Brink, and P. L. McEuen, "Tuning carbon nanotube bandgaps with strain," *Arxiv preprint cond-mat/0211152*, 2002.

[58] S. Peng, J. O'Keeffe, C. Wei, K. Cho, J. Kong, R. Chen, N. Franklin, and H. Dai, "Carbon nanotube chemical and mechanical sensors," in 3rd International Workshop on Structural Health Monitoring, Stanford, CA, USA, 2001, pp. 1142-1148.

[59] T. W. Tombler, C. Zhou, L. Alexseyev, J. Kong, H. Dai, L. Liu, C. Jayanthi, M. Tang, and S. Y. Wu, "Reversible electromechanical characteristics of carbon nanotubes under local-probe manipulation," *Nature,* vol. 405, no. 6788, pp. 769-772, 2000.

[60] I. Kang, M. J. Schulz, J. H. Kim, V. Shanov, and D. Shi, "A carbon nanotube strain sensor for structural health monitoring," *Smart Materials and Structures,* vol. 15, pp. 737, 2006.

[61] P. Dharap, Z. Li, S. Nagarajaiah, and E. Barrera, "Nanotube film based on single-wall carbon nanotubes for strain sensing," *Nanotechnology,* vol. 15, pp. 379-382, 2004.

[62] W. Ding, S. Pengcheng, L. Changhong, W. Wei, and F. Shoushan, "Highly oriented carbon nanotube papers made of aligned carbon nanotubes," *Nanotechnology,* vol. 19, no. 7, pp. 075609, 2008.

[63] M. Rein, O. Breuer, and H. Wagner, "Sensors and sensitivity: Carbon nanotube buckypaper films as strain sensing devices," *Composites Science and Technology,* vol. 71, no. 3, pp. 373-381, 2011.

[64] C. K. M. Fung, and W. J. Li, "Ultra-low-power polymer thin film encapsulated carbon nanotube thermal sensors." pp. 158-160.

[65] K. J. Loh, J. Kim, J. P. Lynch, N. W. S. Kam, and N. A. Kotov, "Multifunctional layer-by-layer carbon nanotube polyelectrolyte thin films for strain and corrosion sensing," *Smart Materials and Structures,* vol. 16, no. 2, pp. 429-438, 2007.

[66] B. R. Loyola, V. La Saponara, and K. J. Loh, "In Situ Strain Monitoring of Fiber-Reinforced Polymers using Embedded Piezoresistive Nanocomposites," *Journal of Material Science,* vol. 45, no. 24, pp. 6786-6798, 2010.

[67] Y. Shindo, Y. Kuronuma, T. Takeda, F. Narita, and S. Y. Fu, "Electrical resistance change and crack behavior in carbon nanotube/polymer composites under tensile loading," *Composites Part B: Engineering,* pp. 39-43, 2011.

[68] H. Yu, T. Cao, L. Zhou, E. Gu, D. Yu, and D. Jiang, "Layer-by-Layer assembly and humidity sensitive behavior of poly(ethyleneimine)/multiwall carbon nanotube composite films," *Sensors and Actuators B: Chemical,* vol. 119, no. 2, pp. 512-515, 2006.

[69] Y. Zhao, B. R. Loyola, and K. J. Loh, "Mechanical and Viscoelastic Characterization of Layer-by-Layer Carbon Nanotube-Polyelectrolyte Thin Films," *Smart Materials and Structures,* vol. 20, no. 7, pp. 075020, 2011.

[70] H. Koerner, G. Price, N. A. Pearce, M. Alexander, and R. A. Vaia, "Remotely actuated polymer nanocomposites—stress-recovery of carbon-nanotube-filled thermoplastic elastomers," *Nature Materials,* vol. 3, no. 2, pp. 115-120, 2004.

[71] Q. Zhang, S. Rastogi, D. Chen, D. Lippits, and P. J. Lemstra, "Low percolation threshold in single-walled carbon nanotube/high density polyethylene composites prepared by melt processing technique," *Carbon,* vol. 44, no. 4, pp. 778-785, 2006.

[72] R. Zhang, A. Dowden, H. Deng, M. Baxendale, and T. Peijs, "Conductive network formation in the melt of carbon nanotube/thermoplastic polyurethane composite," *Composites Science and Technology,* vol. 69, no. 10, pp. 1499-1504, 2009.

[73] N. D. Alexopoulos, C. Bartholome, P. Poulin, and Z. Marioli-Riga, "Structural health monitoring of glass fiber reinforced composites using embedded carbon nanotube (CNT) fibers," *Composites Science and Technology,* vol. 70, no. 2, pp. 260-271, Feb, 2010.

[74] F. H. Gojny, M. H. G. Wichmann, B. Fiedler, I. A. Kinloch, W. Bauhofer, A. H. Windle, and K. Schulte, "Evaluation and identification of electrical and thermal conduction mechanisms in carbon nanotube/epoxy composites," *Polymer,* vol. 47, no. 6, pp. 2036-2045, 2006.

[75] P. C. Ma, J. K. Kim, and B. Z. Tang, "Effects of silane functionalization on the properties of carbon nanotube/epoxy nanocomposites," *Composites Science and Technology,* vol. 67, no. 14, pp. 2965-2972, 2007.

[76] E. T. Thostenson, and T.-W. Chou, "Real-time in situ sensing of damage evolution in advanced fiber composites using carbon nanotube networks," *Nanotechnology,* vol. 19, no. 21, pp. 215713, 2008.

[77] M. H. G. Wichmann, J. Sumfleth, B. Fiedler, F. Gojny, and K. Schulte, "Multiwall carbon nanotube/epoxy composites produced by a masterbatch process," *Mechanics of Composite Materials,* vol. 42, no. 5, pp. 395-406, 2006.

[78] G. Pecastaings, P. Delhaes, A. Derre, H. Saadaoui, F. Carmona, and S. Cui, "Role of interfacial effects in carbon nanotube/epoxy nanocomposite behavior," *Journal of nanoscience and nanotechnology,* vol. 4, no. 7, pp. 838-843, 2004.

[79] L. Böger, M. Wichmann, L. Meyer, and K. Schulte, "Load and health monitoring in glass fibre reinforced composites with an electrically conductive nanocomposite epoxy matrix," *Composites Science and Technology,* vol. 68, no. 7-8, pp. 1886-1894, 2008.

[80] S. Kessler, and A. Raghavan, "Co-Located Triangulation for Damage Position Identification from a Single SHM Node." pp. 1-5.

[81] M. Lin, and F. Chang, "The manufacture of composite structures with a built-in network of piezoceramics," *Composites Science and Technology,* vol. 62, no. 7-8, pp. 919-939, 2002.

[82] A. P. Calderon, "On an inverse boundary value problem," *Comp. Appl. Math,* vol. 25, no. 2-3, pp. 133-138, 2006.

[83] A. Adler, and R. Guardo, "Electrical impedance tomography: regularized imaging and contrast detection," *IEEE Transactions on Medical Imaging,* vol. 15, no. 2, pp. 170-179, 1996.

[84] M. Cheney, D. Isaacson, J. Newell, S. Simske, and J. Goble, "NOSER: An algorithm for solving the inverse conductivity problem," *International Journal of Imaging Systems and Technology,* vol. 2, no. 2, pp. 66-75, 1990.

[85] N. Polydorides, "Image Reconstruction Algorithms For Soft-Field Tomography," Department of Electrical Engineering and Electronics, University of Manchester Institute of Science and Technology, Manchester, United Kingdom, 2002.

[86] W. R. Breckon, "Image reconstruction in electrical impedance tomography," 1990.

[87] D. C. Dobson, and F. Santosa, "An image-enhancement technique for electrical impedance tomography," *Inverse Problems,* vol. 10, pp. 317, 1994.

[88] L. Horesh, M. Schweiger, S. Arridge, and D. Holder, "Large-scale non-linear 3D reconstruction algorithms for electrical impedance tomography of the human head." pp. 3862-3865.

[89] M. Molinari, B. H. Blott, S. J. Cox, and G. J. Daniell, "Optimal imaging with adaptive mesh refinement in electrical impedance tomography," *Physiological measurement,* vol. 23, pp. 121, 2002.

[90] Y. Li, and D. W. Oldenburg, "3-D Inversion of DC Resistivity Data Using an L-curve Criterion," in 1999 Society of Exploration Geophysicists Annual Meeting, Houston, Texas, 1999.

[91] B. Graham, and A. Adler, "Objective selection of hyperparameter for EIT," *Physiological measurement,* vol. 27, no. S65, 2006.

[92] P. Hua, E. J. Woo, J. G. Webster, and W. J. Tompkins, "Iterative reconstruction methods using regularization and optimal current patterns in electrical impedance tomography," *IEEE Transactions on Medical Imaging,* vol. 10, no. 4, pp. 621-628, 1991.

[93] T. J. Yorkey, J. G. Webster, and W. J. Tompkins, "Comparing reconstruction algorithms for electrical impedance tomography," *IEEE Transactions on Biomedical Engineering*, no. 11, pp. 843-852, 1987.

[94] M. Vauhkonen, "Electrical impedance tomography and prior information," Department of Physics, University of Kuopio, University of Kuopio, 1997.

[95] J. F. P. J. Abascal, S. R. Arridge, D. Atkinson, R. Horesh, L. Fabrizi, M. De Lucia, L. Horesh, R. H. Bayford, and D. S. Holder, "Use of anisotropic modelling in electrical impedance tomography; Description of method and preliminary assessment of utility in imaging brain function in the adult human head," *Neuroimage,* vol. 43, no. 2, pp. 258-268, 2008.

[96] B. Abdellatif El, "Inverse source problem in an anisotropic medium by boundary measurements," *Inverse Problems,* vol. 21, no. 5, pp. 1487, 2005.

[97] A. Borsic, W. R. B. Lionheart, and C. N. McLeod, "Generation of anisotropic-smoothness regularization filters for EIT," *Medical Imaging, IEEE Transactions on,* vol. 21, no. 6, pp. 579-587, 2002.

[98] K. Astala, L. PaIvarinta, and M. Lassas, "Calderóns' Inverse Problem for Anisotropic Conductivity in the Plane," *Communications in Partial Differential Equations,* vol. 30, no. 1-2, pp. 207-224, 2005/04/01, 2005.

[99] G. Allan, L. Matti, and U. Gunther, "Anisotropic conductivities that cannot be detected by EIT," *Physiological measurement,* vol. 24, no. 2, pp. 413, 2003.

[100] A. Lehikoinen, S. Finsterle, A. Voutilainen, M. B. Kowalsky, and J. P. Kaipio, "Dynamical inversion of geophysical ERT data: state estimation in the vadose zone," *Inverse Problems in Science and Engineering,* vol. 17, no. 6, pp. 715-736, 2009/09/01, 2009.

[101] K. J. Loh, T. C. Hou, J. P. Lynch, and N. A. Kotov, "Carbon Nanotube Sensing Skins for Spatial Strain and Impact Damage Identification," *Journal of Nondestructive Evaluation,* vol. 28, no. 1, pp. 9-25, 2009.

[102] T. Hou, K. Loh, and J. Lynch, "Spatial conductivity mapping of carbon nanotube composite thin films by electrical impedance tomography for sensing applications," *Nanotechnology,* vol. 18, no. 31, pp. 315501, 2007.

[103] S. Pyo, K. J. Loh, T. C. Hou, E. Jarva, and J. P. Lynch, "A wireless impedance analyzer for automated tomographic mapping of a nanoengineered sensing skin," *Smart Structures and Systems,* vol. 8, no. 1, pp. 139-155, 2011.

[104] H. Alirezaei, A. Nagakubo, and Y. Kuniyoshi, "A highly stretchable tactile distribution sensor for smooth surfaced humanoids," in 7th IEEE-RAS International Conference on Humanoid Robots, Pittsburgh, Pennsylvania, USA, 2007, pp. 167-173.

[105] H. Alirezaei, A. Nagakubo, and Y. Kuniyoshi, "A tactile distribution sensor which enables stable measurement under high and dynamic stretch," in IEEE Symposium on 3D User Interfaces, Lafayette, Louisiana, USA, 2009, pp. 87-93.

[106] R. Lazarovitch, D. Rittel, and I. Bucher, "Experimental crack identification using electrical impedance tomography," *NDT and E International,* vol. 35, no. 5, pp. 301-16, 2002.

Chapter 2: The Electrical Response of Carbon Nanotube-based Thin Film Sensors Subjected to Mechanical and Environmental Effects

2.1 Abstract

Fiber-reinforced polymer composites are a popular alternative to traditional metal alloys. However, their internally-occurring damage modes call for strategies to monitor these structures. Multi-walled carbon nanotube-based polyelectrolyte thin films were manufactured using a layer-by-layer deposition methodology. The thin films were applied directly to the surface of glass fiber-reinforced polymer composites, with the purpose of structural monitoring. This work focuses on characterizing the sensitivity of the electrical properties of the film using time- and frequency domain methods under applied quasi-static and dynamic mechanical loading. In addition, environmental effects such as temperature and humidity are varied to characterize the sensitivity of the electrical properties due to these phenomena.

2.2 Introduction

Fiber-reinforced polymer (FRP) composites are utilized as a variety of structural components for their high strength-to-weight ratios, resistance to corrosion and fatigue, and conformability. Examples include aerospace, civil, automobile, wind turbine, and naval structures. They are a popular alternative to traditional monolithic alloys. For instance, the Boeing 787 Dreamliner that was released in October 2011 has a structure that is more than 50% composite material by weight, with the majority consisting of carbon FRP composites [1]. In contrast, wind turbine blades typically consist of glass FRP composites due to their low cost and high specific strength [2].

Despite many desirable traits, composite materials can and do sustain damage when subjected to various loading scenarios, including impact, excessive loading, fatigue, material defects, environmental deterioration, improper manufacturing, and fluid penetration. Damage induces failure modes such as delamination, fiber and matrix breakage, fiber-matrix debonding, matrix swelling, and matrix and fiber deterioration. In general, these damage modes tend to manifest internally to the composite structure, and this minimizes the ability to use visual inspection for damage detection. This is a problem, since visual inspection is the predominant method of non-destructive evaluation in many disciplines, including aerospace and civil structures. Undetected structural damage can propagate, eventually leading to catastrophic structural failure [3].

As a result of the shortcomings of visual inspection, several alternative damage detection approaches have been developed and applied to this very urgent problem. Examples of structural health monitoring (SHM) techniques that have been developed for or applied to composite damage detection include optical fibers [4], acoustic emission [5], ultrasonic sensors [6], strain gauges [7], and shape memory alloys [8], to name a few. All of these methods have shown promise in their capability to capture various modes of damage, but they also have drawbacks that need to be addressed by complementary methodologies. Many of these systems require expensive and bulky hardware and data acquisition systems, such as optical fibers and ultrasonic- and acoustic-based methods. When embedded in composite materials, these sensors have been shown to diminish composite mechanical properties (*e.g.*, optical fibers over 100 μm in diameter [9] or piezoelectric disks for ultrasonic monitoring [10]). It is for these reasons that many groups have pursued other sensing approaches that directly modify the composite material. An example is to develop piezoresistive FRP composites by embedding nanomaterials within their epoxy matrix. Monitoring the integrity of the structure can be achieved by probing its electrical properties, and the method does not adversely affect the mechanical properties of the structure.

The discovery of carbon nanotubes [11] and the identification of their unique material properties [12] has brought forth widespread attention to the use of this material for various sensing/actuation applications. Carbon nanotubes are typically introduced into FRP composites in two distinct ways: as an additive to the polymer matrix or as a thin film within or upon the composite. These applications take advantage of the high mechanical and electrical properties intrinsic to single-walled (SWNT) and multi-

walled (MWNT) carbon nanotubes [13]. It has been found that the electrical properties of CNT-based nanocomposites can change drastically when mechanical loading or damage is induced in them. Some examples of this work are CNT-epoxy nanocomposites [14], neat CNT mats (*i.e.*, buckypapers) [15, 16], and other polymer nanocomposites thin films [17, 18]. From these selected references and throughout the available literature, the response to mechanical loading of CNT nanocomposites varies widely and includes linear [16], non-linear [19], and multifunctional responses [20]. In addition to strain sensitivity, these films are also sensitive to changes in environmental conditions such as temperature [21] and humidity [22]. This type of environmental sensitivity in a sensor is not uncommon, with some examples including metal-foil strain gauges [23] and fiber-Bragg gratings [24]. Thus, prior to using CNT nanocomposites for SHM, a full characterization of their sensing and environmental response is needed.

The purpose of this article is to characterize the strain sensing and environmental sensitivity response of MWNT-based thin films manufactured using a layer-by-layer fabrication process. Films of different thicknesses have been deposited directly onto the surface of glass fiber-reinforced polymer (GFRP) composites for direct strain sensing. The responses from these tests are complementary to the work previously performed on thin films embedded in GFRPs for *in situ* strain sensing [20]. First, strain sensing characterization of film-enhanced GFRP substrates have been performed by loading them in monotonic uniaxial tension, low-cycle dynamic, and high-cycle dynamic load patterns. Thin film electrical properties have been measured simultaneously using time- and frequency-domain methods. Secondly, their environmental responses have been determined by measuring the electrical response of the films at a wide range of temperature and humidity levels. These responses have been fully characterized by curve fits motivated by physics-based models.

2.3 Experimental Methods

To demonstrate the capability of these films as an alternative for structural health monitoring of FRP composites, the MWNT-based thin films were deposited on GFRP substrates upon which all of the mechanical, thermal, and humidity tests were performed.

2.3.1 Film Fabrication

The deposition of the MWNT-based thin films upon the GFRP substrates was performed by a layer-by-layer (LbL) process that allows for nano-scale control of film deposition [25, 26]. The substrates

used were quasi-unidirectional glass fiber weaves (type 7715, Applied Vehicle Technology) that were impregnated with a two-part epoxy (125 resin / 237 hardener, Proset Inc.) and cured to specification for 15 h at 25 °C and 8 h at 80 °C. The substrates were cut to 25 x 75 mm^2 and were thoroughly cleaned with water and isopropyl alcohol prior to mounting them in the LbL deposition system. Layer-by-layer film assembly is based on the sequential deposition of opposite-charged materials onto a substrate such as the GFRP specimens used in this study [25]. To deposit the first monolayer, the LbL system was programmed to immerse the substrates in a 0.5 wt.% poly(vinyl alcohol) (PVA) solution for 5 minutes. Electrostatic and van der Waals forces drove the adsorption of PVA molecules onto the substrate. The substrates were then rinsed for 3 min in deionized water and then dried with compressed air for 5 min. To deposit the next monolayer, the dried substrates were immediately immersed in a 1.0 wt.% solution of poly(sodium 4-styrenesulfonate) (PSS) with 1 $mg \cdot mL^{-1}$ of MWNTs (Cheap Tubes, <8 nm diameter, 10-30 μm length) dispersed into the solution. The dispersal of the MWNTs into the PSS solution was accomplished by 180 min of bath sonication (135W, 42 kHz) followed by 1 h of tip sonication (3 mm tip, 150 W, 20 kHz). This two-step sonication process ensured a fully stable suspension of the MWNTs in the PSS solution. Following the immersion in the MWNT-PSS solution [18, 20], the substrates were rinsed again for 3 min and dried for 5 min, so as to remove any loosely adsorbed polyelectrolyte and nanotubes. This process was repeated for a specified number of times, each time depositing a single bilayer of the thin film (Figure 2.1). Numerous thin films were manufactured with 25, 50, 75, 100, and 150 bilayers.

The thin films resulting from this process were extremely robust, due to the chemical bond formed between the substrate to the film constituents and between the thin film chemical species. Popular thin film constituents for the LbL process are polyelectrolytes of opposite ionic charge facilitating electrostatic assembly of the thin film, of which PSS and PVA are both members of this chemical family. However, PSS and PVA bond through a covalent manner that creates a more robust film [27]. The MWNTs were bound within this polyelectrolyte matrix via polymer wrapping by the PSS, which has wound chains around each MWNT to reduce MWNT hydrophobicity [28]. A previous study of freestanding CNT-PSS/PVA films had been previously reported and validated the impressive mechanical properties resulting from the chemical associations between the film constituents [29].

Figure 2.1. Pictorial representation of a layer-by-layer manufactured $(MWNT\text{-}PSS/PVA)_n$ thin film. PSS chains (helical red lines) wrapped around MWNTs (straight black lines) with deposited PVA (thin blue lines).

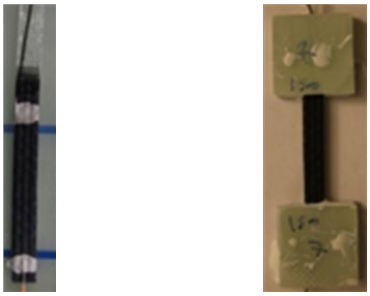

(a) (b)

Figure 2.2. $(MWNT\text{-}PSS/PVA)_n$ thin film deposited onto GFRP substrates before (a) and after (b) tabbing.

2.3.2 Specimen Preparation and Electrical Characterization

With the aim to characterize the electrical response of the thin film to mechanical, thermal, and hygroscopic conditions, uniform specimens and electrical characterization methods were used as a means to remove any dimensional effects on the sensitivities of the thin films. The ASTM standard for characterizing the tensile properties of FRP composites was consulted for determining specimen size [30]. Due to the setup used for film deposition, only 40 mm of the 75 mm length of the substrate was deposited with $(MWNT\text{-}PSS/PVA)_n$ films (where the subscript *n* indicates the number of bilayers). Following the ASTM suggestion of a 1:11 width-to-gauge length ratio, the width of the specimens was set to 3 mm for a 25 mm gauge length. In order to protect the electrodes from strain effects, the electrodes were placed outside of the gauge length with an electrical gauge length of ~28 mm. Two-point probe electrical measurements were used due to the limited space on the specimen. Contact resistance was minimized by using a highly conductive silver paint as the electrode (Figure 2.2a). To protect the substrates from damage from the grips during mechanical testing, G-10 GFRP tabs were applied to opposite ends of each specimen with a high strength adhesive (Hysol 903, Henkel Corp.). An example of a finished electromechanical specimen is presented in Figure 2.2b.

Measurement of $(MWNT\text{-}PSS/PVA)_n$ thin film electrical properties were performed using time-domain direct current (DC) resistance measurements and frequency-domain electrical impedance spectroscopy (EIS). The DC resistance measurements were performed using an Agilent 34401A digital multimeter with 6.5 digit accuracy. The EIS responses were taken using an Agilent 4294A impedance

analyzer over a frequency range of 40 Hz to 110 MHz. The impedance analyzer measured impedance by injecting a complex current between the two applied electrodes and measured the corresponding voltage and phase lag. A calculation analogous to Ohm's law was performed by the instrument to determine the complex impedance and was reported for each of the 201 frequencies logarithmically spaced throughout the frequency range.

2.3.3 Mechanical Strain Sensitivity Characterization

The strain sensing or piezoresistive response of $(MWNT\text{-}PSS/PVA)_n$ thin films were characterized by measuring their time-domain DC electrical resistance and frequency-domain impedance responses during applied mechanical loading. A total of three different sets of loading patterns were applied to specimens fabricated with different film thicknesses or number of bilayers: monotonically increasing strain to failure, low-cycle dynamic strain patterns, and high-cycle dynamic strain patterns. Each test was performed on thin films with 25, 50, 75, 100, and 150 bilayers to characterize the mechanical response as a function of film thickness. All mechanical testing was performed on a Test Resources 150R load frame equipped with a 4.48 kN load cell with serrated grips. The displacement and angular position of the load frame cross-head is verified using two laser displacement sensors (Microtrak II, MTI Instruments).

2.3.3.1 Monotonic Uniaxial Tension Tests

The full range of the films' piezoresistive response was characterized by applying monotonically increasing strain to each GFRP substrate (with an applied $(MWNT\text{-}PSS/PVA)_n$ film) until failure. Adhering to the ASTM 3039 standard, the load frame displacement is fixed at 2 $mm \cdot min^{-1}$. In order to measure the change in electrical properties at fixed strain values, the crosshead displacement was held at specified strain values for a 60 s period, when both the DC resistance and EIS measurement were obtained. These specified strain values were every 1,000 με from 0 to 10,000 με and every 5,000 με thereafter. This measurement pattern allowed for higher resolution at lower strain values, while limiting the number of pauses to minimize any effects of creep.

2.3.3.2 Low-cycle Dynamic Tests

Three-cycle tensile dynamic load tests to 8,000 με and to 25,000 με were conducted on film-enhanced GFRP specimens for characterizing thin film electromechanical responses to repeated loading and unloading. During each cyclic loading, a 60 s pause was taken at 25% increments of the total strain. As

before, these pauses allowed for the DC resistance and EIS measurement to be taken. The two different strain amplitudes were chosen based on results obtained from Section 2.3.3.1 and allowed for probing the two regions of the bi-functional electrical response.

2.3.3.3 High Cycle Dynamic Tests

As the long term intent for these films is implementation as a SHM sensor, it is important to understand how the electrical properties of the thin films change after numerous cycles of mechanical loading. To this end, specimens were subjected to 1,000 cycles of sinusoidal-cyclic loading from 0 to 8,000 με at a frequency of 1 Hz. A 60 s pause was taken at a strain value of 4,000 με every 100 cycles s to measure the film's DC resistance and EIS response. The strain amplitude was determined using the same logic as in the low-cycle dynamic tests described in Section 2.3.3.2.

2.3.4 Thermal Testing

The effects of temperature change to the films' electrical properties were characterized by subjecting specimens to monotonically increasing temperatures from ambient to 100 °C in increments of 5 °C in a convection oven. To test all specimens under the same conditions, five specimens each with thicknesses 50, 75, 100, or 150 bilayers were attached to a pristine sheet of G-10 using high-temperature kapton tape. Only one end of each specimen was affixed to the G-10 GFRP to allow unconstrained thermal expansion to occur. DC resistance measurements were taken at each temperature step after the specimens had come to thermal equilibrium.

2.3.5 Humidity Testing

Another environmental factor taken into account was the effect of humidity on the electrical properties of the $(MWNT\text{-}PSS/PVA)_n$ films. As with the thermal tests (Section 2.3.4), five specimens each with thicknesses of 50, 75, 100, or 150 bilayers were mounted onto a G-10 GFRP sheet. The sheet of specimens was placed in an environmental chamber set at 35 °C. The chamber was programmed to increase its humidity from 25 to 80 %RH in 5 %RH increments and holding at each level for 1 h. The humidity and temperature of the chamber were verified using a temperature and humidity probe that takes a measurement every 10 s. The 20 specimens were connected to an Agilent 34970A with an armature multiplexer card to measure DC resistances of each specimen every 5 s.

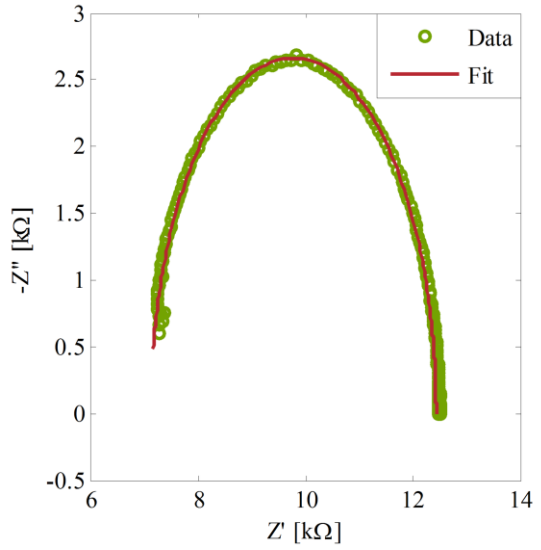

Figure 2.3. Example of an $(MWNT\text{-}PSS/PVA)_n$ EIT response and the corresponding fit to the equivalent circuit model.

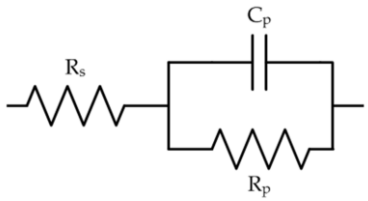

Figure 2.4. Circuit diagram of the equivalent circuit model representing the EIS response of the films

2.4 Results and Discussion

2.4.1 EIS Equivalent Circuit Fitting

A typical $(MWNT\text{-}PSS/PVA)_n$ thin film EIS response is plotted on a Nyquist plot, as shown in Figure 2.3, and this semi-circular trend is consistent with the response of other CNT thin films [17, 31]. To extract the underlying electrical properties of the film from this response, the spectrum is typically fit to a physics-based equivalent circuit model. The characteristic equivalent circuit model for a response such as the one in Figure 2.3 is a series resistor (R_s) connected to a resistor (R_p) and capacitor (C_p) in parallel and is shown in Figure 2.4. This circuit model has been used previously to describe a similar EIS response of a zirconia-yttria solid electrolyte film, where the series resistor models the mean grain resistance, and the inter-grain effects are modeled by the parallel resistor and capacitor [32]. The impedance equation that corresponds to the equivalent circuit shown in Figure 2.4 is represented in Equation (2.1):

$$Z(\omega) = Z'(\omega) + iZ''(\omega) = \left(R_s + \frac{1/R_p}{(1/R_p)^2 + \omega^2 C_p^2} \right) - i\left(\frac{\omega C_p}{(1/R_p)^2 + \omega^2 C_p^2} \right) \tag{2.1}$$

Fitting of this highly non-linear model to the EIS spectra is achieved using the non-linear least squares solver function in MATLAB.

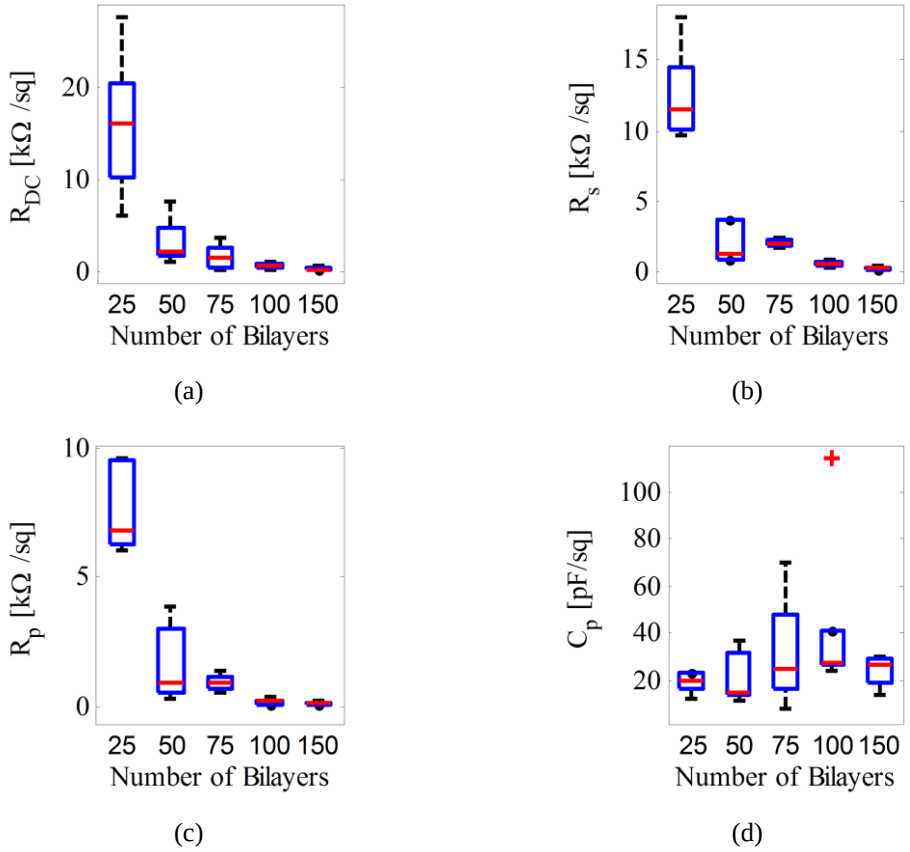

Figure 2.5. Unstrained electrical properties of $(MWNT\text{-}PSS/PVA)_n$ films as a function of film thickness plotted in a boxplot. The box indicates the interquartile region and the line within it signifies the median of the data.

2.4.2 Thin Film Electrical Properties: Unstrained

Before the mechanical, thermal, or humidity sensitivities of the films are discussed, it is important to characterize the baseline electrical properties of the $(MWNT\text{-}PSS/PVA)_n$ thin films as a function of thickness. The initial unstrained time- and frequency-domain electrical measurements from all of the mechanical experiments were compiled into boxplots as shown in Figure 2.5. Figure 2.5a shows the films' unstrained DC resistance, whereas Figures 2.5b-d present the numerically fitted equivalent circuit parameters based on Figure 2.4. It can be seen from Figure 2.5 that the median and interquartile range of the DC resistance and resistive equivalent circuit elements reduce significantly with increasing number of bilayers. This is consistent with power-law type response of particle-infused polymer composites (*i.e.*

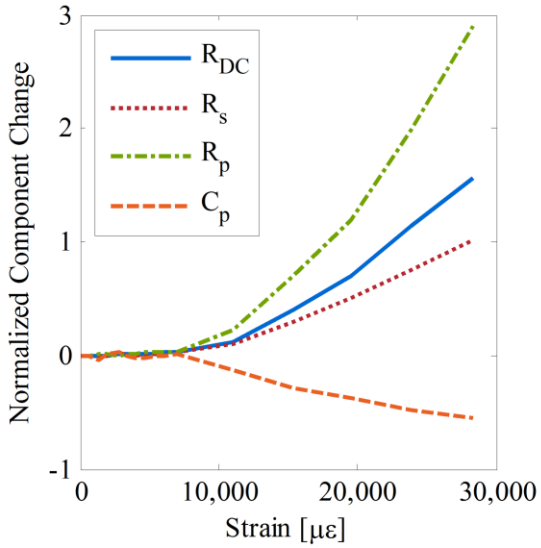

Figure 2.6. DC resistance and EIS fitted circuit elements response to monotonically increasing strain

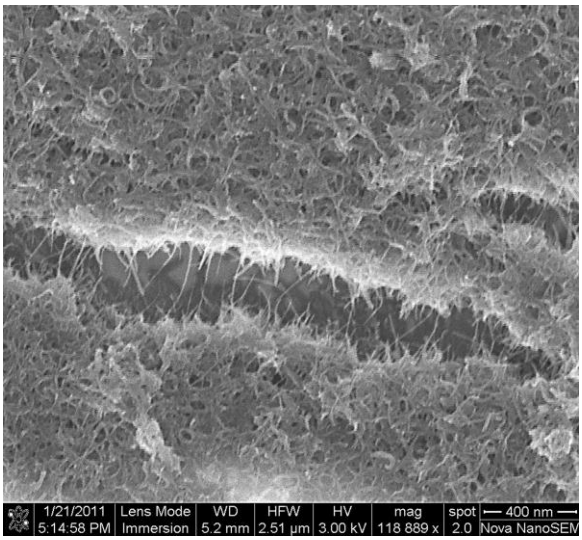

Figure 2.7. SEM image of damage to the (MWNT-PSS/PVA)$_n$ film.

nanocomposites), particularly in the post-percolation region [33-36]. As for the capacitance of the films, Figure 2.5d indicates that the capacitance stays relatively constant over the range of thin film thicknesses tested. Similar trends have also been identified by Loh *et al.* [18].

2.4.2 Uniaxial Tensile Electromechanical Response

As mentioned in Section 2.3.3.1, monotonic uniaxial tests have been conducted on GFRP specimens with (MWNT-PSS/PVA)$_n$ films for characterizing the full range of thin film piezoresistivity. Both DC resistance and EIS data have been obtained, and EIS responses have been fit to the parallel resistor-capacitor circuit shown in Figure 2.4. In order to directly compare different circuit elements dependency on strain, all of the DC resistance and EIS equivalent circuit elements are presented as normalized changes relative to the initial unstrained parameter measurement. For example, calculation of normalized resistance uses Equation (2.2), where R_0 is the unstrained resistance value.

$$R_{norm} = \frac{\Delta R}{R_0} \tag{2.2}$$

An example of a full strain response is presented in the plot shown in Figure 2.6. The responses by all of the electronic parameters are bi-functional in nature. For the resistive parameters, there exists a positive relationship between normalized changes in resistance as a function of increasingly applied tensile

strains. Several other groups have also found that CNT-based films increase their resistivity in tandem with increasing tensile strains [16, 31, 37]. In addition, Thostenson and Chou [38] and Shindo *et al.* [39] have also observed this bi-functional response comparable to Figure 2.6, although these studies have not explored the frequency-domain impedance response of CNT-based nanocomposites. The initial functional response is generally considered due to MWNT stretching or rigid-body motion of MWNTs within the compliant polymer matrix, while the second functional response is due to damage in the film in the form of micro-cracking of the composite substrate [14, 39]. This damage can be seen in the scanning electron microscope (SEM) image shown in Figure 2.7. On the other hand, film capacitance change is near zero during the first response region while decreasing after the application of large tensile strains.

Upon identification of the bi-functional circuit parameter responses to applied strain, it has been found that a linear-quadratic model can adequately fit the films' electromechanical responses. First, the transition point of the bi-functional response (*i.e.*, from low strain to high strain) has been manually identified and recorded. Then, the linear-quadratic model has been fit to each data set using the non-linear least squares fit function 'lsqnonlin' in MATLAB. The equation of the linear-quadratic model is also shown as follows:

$$\frac{\Delta R}{R_0}(\varepsilon) = \frac{1}{2}\left(1 - erf\left(\varepsilon - \varepsilon_{tr}\right)\right)\cdot\left(A + B\varepsilon\right) + \ldots$$
$$\frac{1}{2}\left(erf\left(\varepsilon - \varepsilon_{tr}\right) + 1\right)\cdot\left(A + B\varepsilon_{tr} + C\left(\varepsilon - \varepsilon_{tr}\right) + D\left(\varepsilon - \varepsilon_{tr}\right)^2\right) \quad (2.3)$$

The transition between the functional responses was facilitated using the error function, noted as erf( ) in the equation. The error function is a sigmoidal function that has a smooth but sharp transition from -1 to 1 and can be shifted and scaled to create the same transition between 0 and 1.

With the thin film time- and frequency-domain electrical responses fit to the linear-quadratic model, the medians of the results are presented in Figure 2.8 in terms of the low-strain linear sensitivity (B), the high-strain linear sensitivity (C), the high-strain quadratic sensitivity (D), and the bi-functional transition point (ε_{tr}) in terms of number of bilayers. The error bars that accompany each result are a measure of the median absolute median deviation, which is a robust measure of the variability of the results. Two distinct trends are apparent by examining the fitted sensitivity parameter in Figure 2.8.

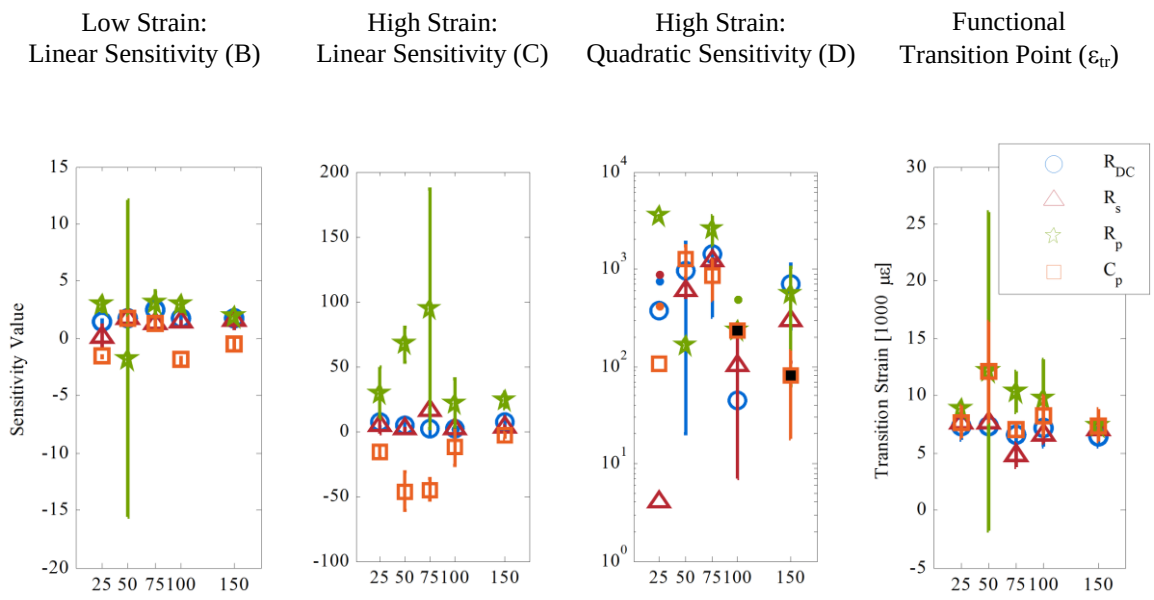

Figure 2.8. Linear-quadratic sensitivities obtained from fits to Equation (2.2). Black-filled symbols indicate negative values and error bars substituted with dots indicate lower bound is a negative value in (c).

The sensitivities of R_{DC} and R_S are statistically similar in both the low- and high-strain regimes. Within the low strain regime, these sensitivities are linear between 1 and 2.5, for all film thicknesses, and exhibit an increase of the linear sensitivities by less than a multiple of three in the higher strain regime. This is in contrast to the responses of the parallel equivalent circuit elements, although the two responses appear to be correlated with one always being positive and the other negative. In the transition between the functional responses, the sensitivities of the parallel equivalent circuit elements demonstrate an increase in linear sensitivities by one to two orders of magnitude with a drastic increase of sensitivity variability. Previous work with CNT-based thin films has been verified by acoustic emission responses [40], and a model incorporating transverse crack propagation [39] shows that this high strain regime is dominated by the response of the film to damage transferred from the damaged substrate. It is felt that this demonstrates a higher sensitivity of the parallel equivalent circuit elements to damage in the thin film as compared to the sensitivities of R_{DC} and R_S. It is not fully understood why a similar correlation is not found in the quadratic sensitivities of the fitted electrical responses in the high strain regime.

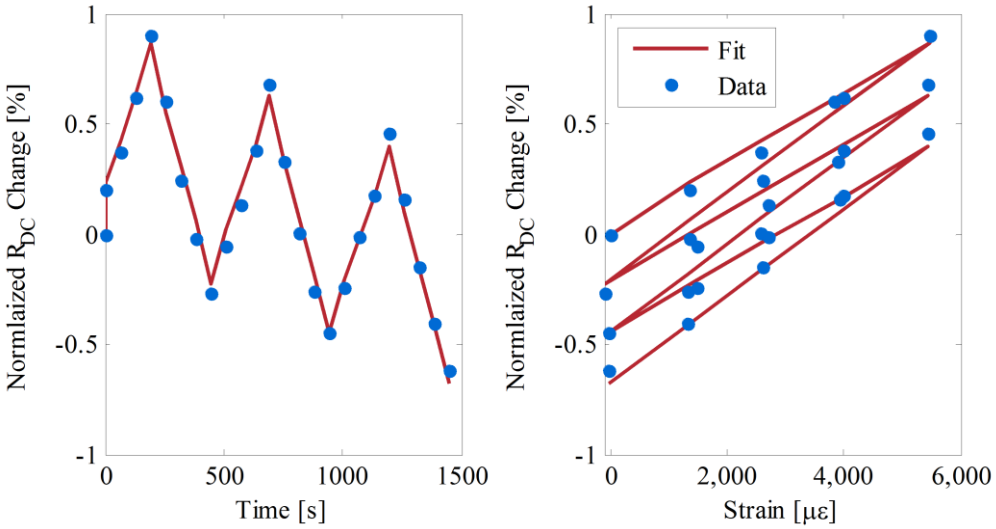

Figure 2.9. Example R_{DC} response to dynamic loading to a magnitude of 8,000 με with the corresponding fit to (4) with and $R^2 = 0.98$.

Despite the differences in the linear sensitivities between R_{DC} and R_S and that of the parallel equivalent circuit elements in the low- and high-strain regimes, the strain at which this transition occurs is statically consistent among all films thicknesses and electrical property parameters. This further reinforces that the change in the response of the electrical properties is indeed due to a physical change, where this transition has been found to be due to the onset of damage within the composite substrate, as have been demonstrated by [39, 40].

2.4.3 Dynamic Strain Response

In addition to monotonic uniaxial tensile tests, films have also been subjected to three-cycle tensile tests to 8,000 με and 25,000 με, as have been described in Section 2.3.3.2. As discussed earlier, these strain amplitudes have been chosen to understand the represented loading effects in both of the response regimes demonstrated by the films during monotonically loaded tests (Section 2.3.3.2).

The responses of the thin films during the lower magnitude dynamic tests to 8,000 με are very consistent among the different specimens tested. An example of this behavior can be seen in Figure 2.9, where the DC resistance linearly drops over time, but the film's piezoresistivity remains constant over time. To model this response, a simple linear-time and linear-strain response equation is fit to each data set, as is described in Equation (2.4):

$$\frac{\Delta R}{R_0} = \alpha t + S\varepsilon \tag{2.4}$$

All of the low-magnitude dynamic responses are fit to Equation (2.4) using the non-linear fitting function in MATLAB. The strain sensitivities of the fits for all specimens tested are reported in Table 2.1. The results for the capacitive elements are left out, because the fits did not reveal any meaningful trends. Among all of the resistive elements, the sensitivity to strain is consistent, where sensitivity varies between 1.5 and 3.3. This is very consistent with the findings from the monotonically loaded samples in the linear region (as presented in Section 2.4.2) as well as other studies on $(CNT\text{-}PSS/PVA)_n$ films [18]. As detailed in Section 2.4.2, this strain response is believed to stem from stretching and slight reorientation of the MWNTs in the film. It can be seen from Table 2.1 that the average strain sensitivities corresponding to each thickness set are consistent for R_{DC}, R_s, and R_p.

In addition to reasonably consistent sensitivity to strain, the response of the electrical properties to the dynamic loading drifts over time with a relatively low-magnitude linear dependence. Overall, the magnitude of the drift is on the order of 10^{-4} $\%\cdot s^{-1}$, which can easily be discerned in the example three-cycle dynamic response shown in Figure 2.9. The direction of the drift is predominantly negative, which is thought to be due to alignment of the carbon nanotubes and has been seen in previous work [31]. A small number of thin films with 100 or 150 bilayers have a very small positive linear trend on the order to 10^{-4} $\%\cdot s^{-1}$, which is thought to be due to the films having a lower bi-functional transition strain than the other films and are slowly accumulating damage within the film. This has been witnessed in other CNT-based thin films [38].

The response of the thin films cycled to 25,000 με is considerably different than that of the 8,000 με cyclic data. Although all responses have demonstrated a general saw tooth-shaped response, the underlying response cannot be fit to a unified model. Nevertheless, Figure 2.10 presents the full DC resistance and EIS circuit element responses for a selected dataset. As is the case with the response to 8,000 με dynamic cycling, the capacitive response is inconsistent between specimens, so these effects will be neglected from comment. Although all of the resistive parameters have a saw tooth shaped response consistent with the shape of the loading, the specific response for each cycle is not consistent. In general, the responses of the electrical properties can be delineated based on their response to increasing and

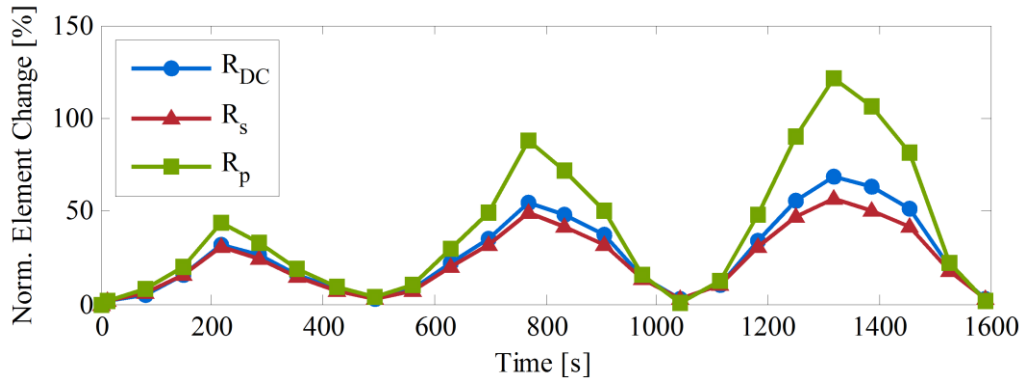

Figure 2.10. Example resistive parameter response to 25,000 με dynamic strain.

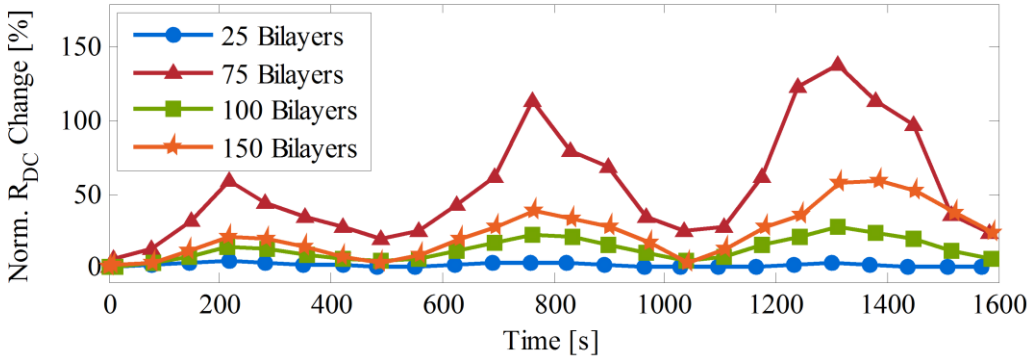

Figure 2.11. Example DC resistance response to 25,000 με dynamic strain for four thin film thicknesses.

decreasing strains. The response to increasing strain is witnessed to be linear, of a concavely increasing or of a convexly increasing manner. However, the resistive responses to decreasing strain are only of concavely or convexly decreasing magnitudes. This myriad of responses is illustrated by four randomly selected curves in Figure 2.11. It can be seen that not one of those responses match. This phenomenon is not surprising as it has been determined in the monotonically loaded case that the quadratic responses occur when damage is sustained by the film due to cracking and other failure phenomena, thus inducing a more random but general response. As indicated before, this type of response has been observed previously [38, 39].

2.3.4 High-Cycle Dynamic Strain Sensing Response

To understand how the thin films will perform in real world application with extended employment, the thin films were subjected to 1,000 cycles of loading as described in Section 2.3.3.3. As illustrated from a representative electrical response shown in Figure 2.12, the overall change in the resistive measurements with respect to the number of cycles is less than 1% over 1,000 cycles. This is comparable to

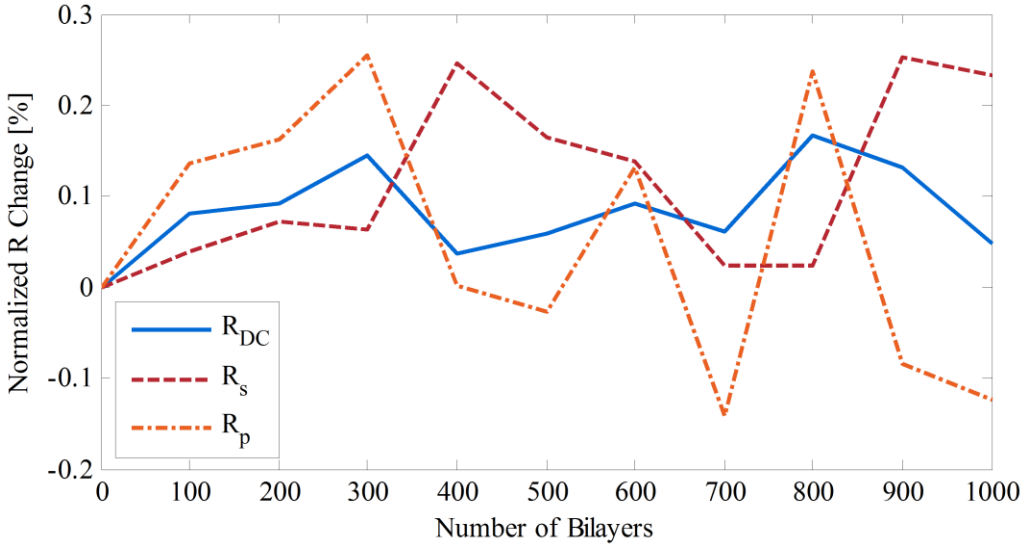

Figure 2.12. Resistive component response to 1,000 cyclic loadings with a magnitude of 8,000 με of a $(MWNT\text{-}PSS/PVA)_{50}$ film.

the time-dependent sensitivity obtained from the three-cycle dynamics tests to 8,000 με and has less drift than previous studies involving repeated dynamic responses with $(SWNT\text{-}PSS/PVA)_n$ films [31]. As with the other dynamic tests, the capacitive results are neglected due to its lack of significance.

2.4.4 Thermal Effect on Electrical Properties

Due to drastic temperature differentials that various structures can experience during operation, it is important to understand the effects of temperature on sensor electrical properties prior to their deployment for SHM. Upon conducting the temperature tests as specified in Section 2.3.4, it has been found that all of the thin films of different thicknesses behaved in the same fashion. An example of the highly non-linear electrical response to the applied monotonically increasing temperature profile is shown in Figure 2.13. This response is characteristic of single-walled carbon nanotubes in mats or tangled ropes, as presented by several researchers [41, 42]. This characteristic response has been studied and a mathematical model has been developed to take this behavior into account, which is given in Equation (2.5):

$$R(T) = R_m e^{-\frac{T_m}{T}} + R_t e^{\frac{T_c}{T+T_s}} \tag{2.5}$$

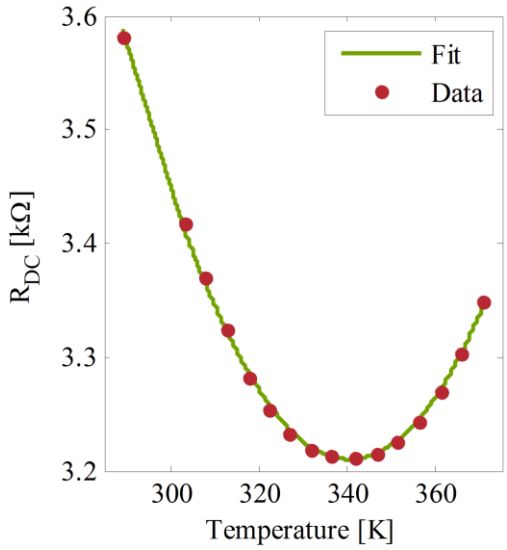

Figure 2.13. Example DC resistance response to monotonically increasing temperature with corresponding fit to Equation (2.5) with $R^2 = 0.998$.

The first term of this equations represents the highly-anisotropic conductivity along the MWNTs, where phonons with energies of $k_B T_m$ backscatter charge carriers [41] and is responsible for the $^{dR}/_{dT} > 0$ behavior. This first term is present in the thermal response of SWNTs as well as MWNTs. The second term of the equation represents electron transport due to electron tunneling between carbon nanotubes. Here T_c and T_s are electron tunneling parameters and represent the combined effect of the nanotube gaps, the PSS and the PVA. The tunneling components are responsible for the $^{dR}/_{dT} < 0$ behavior in the data. However, this response tends to be the case for SWNTs [43] and not typically for MWNT thin films. In the general MWNT case, the second component tends to be linear in nature and not exponential, as in the case of several studies involving individual MWNTs [44, 45], aligned MWNT buckypapers [46, 47], or other MWNT nanocomposites [48].

Equation (2.5) is fit to the collected data using MATLAB's non-linear least squares function, and the corresponding parameters are reported as a function of the number of bilayers in Table 2.2. As this table indicates, the thermal properties of our films are linked to thin film thickness. Although R_m is several orders of magnitude higher than R_t, the metallic resistance contribution only contributes 3.3% of the total resistance at room temperature, but the effect is high enough at higher temperatures to account for the positive slope of the resistance response. As a reference for comparison, the fit parameters obtained by

Table 2.2. Fitted parameters of DC resistance response to monotonically increasing temperature.

Number of Bi-Layers	R_m [kΩ]	R_t [kΩ]	T_m [10^3 K]	T_c [10^3 K]	T_s [K]
50	610 ± 177	0.310 ± 0.085	1.98 ± 0.26	1.30 ± 0.24	114 ± 19
75	83.9 ± 32.5	0.147 ± 0.047	1.28 ± 0.15	1.13 ± 0.09	57.7 ± 8.5
100	68.0 ± 20.7	0.194 ± 0.055	1.19 ± 0.10	1.11 ± 0.08	48.9 ± 4.8
150	21.5 ± 5.0	0.108 ± 0.022	0.99 ± 0.09	1.01 ± 0.07	45.2 ± 7.8
SWNT-Rope [41]	-	-	~2.00	0.065	42

Kaiser *et al.* [41] are included in Table 2.2 as well. It should be noted that the only significant deviation from the SWNT thermal sensitivity is the value of the T_c term, which is two orders of magnitude smaller than that of the $(MWNT\text{-}PSS/PVA)_n$ films. As stated before, this difference is thought to be due to the extra tunneling required due to the presence of PSS and PVA. The ramifications of these temperature effects on strain sensitivities is not fully known for these particular $(MWNT\text{-}PSS/PVA)_n$ thin films. However, Cao *et al.* [21] has reported that the electrical sensitivity to strain increases with temperature for MWNT buckypapers. It is hypothesized that this effect will extend to the strain sensitivities of the $(MWNT\text{-}PSS/PVA)_n$ films; however this will be investigated in the future.

With regards to the thermal-resistive behavior, it is not fully understood why the $(MWNT\text{-}PSS/PVA)_n$ films have responded to temperature in a manner like that of SWNTs instead of other MWNTs. It is hypothesized that this is due to the fact that the MWNTs used in this study are less than 8 nm in diameter. This translates to MWNTs having very few walls (*i.e.*, only two to four concentric tubes per MWNT). Although the difference in electronic properties has been investigated between SWNTs and MWNTs, it is not clear how these properties affect the thermal-electronic coupling, and more work is necessary in the future.

2.4.5 Humidity Response

The responses of the $(MWNT\text{-}PSS/PVA)_n$ thin films to monotonically increasing humidity levels are highly non-linear, as indicated by the DC resistance responses shown in Figure 2.14. Figure 2.14 plots a representative response from each of the thin film thickness sample sets. Plotted with a y-axis logarithmic scale, it is easy to see that thin film electrical responses to humidity are bi-functional in nature, possessing

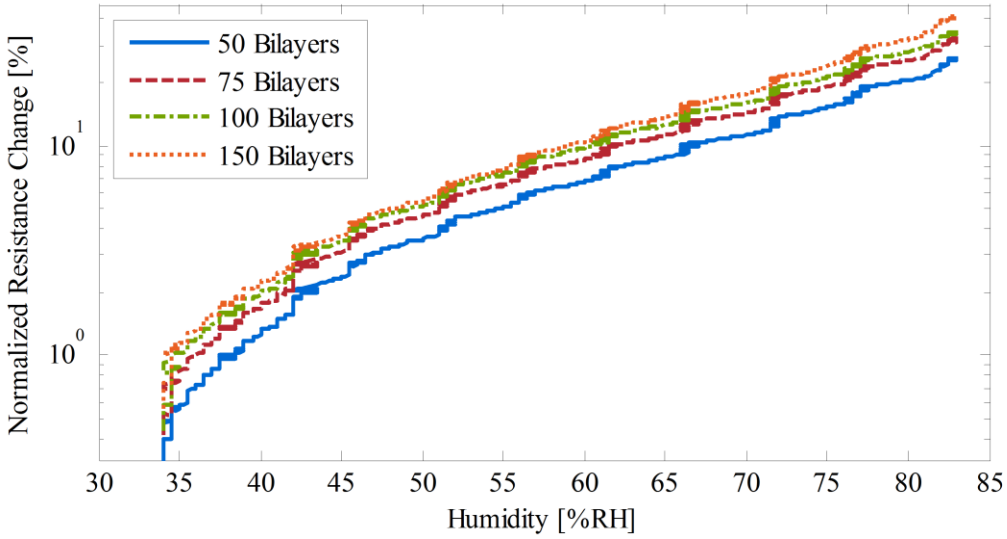

Figure 2.14. R_{DC} response to increasing humidity levels for 4 representative thin films.

two regions of different exponential sensitivity. Using a sigmoidal function to relate two exponential functions, the data has been fit to the following equation:

$$\frac{\Delta R}{R_0}(\%RH) = \frac{1}{2}\left(1 - erf\left(\%RH - H_{Tr}\right)\right)\cdot H_1 e^{f_1(\%RH)} + \frac{1}{2}\left(erf\left(\%RH - H_{Tr}\right) + 1\right)\cdot H_2 e^{f_2(\%RH)} \tag{2.6}$$

In Equation (2.6), erf( ) is the error function, which is in the sigmoidal class of functions that returns a sharp transition between -1 and 1, thereby allowing for a transition to be made between the two exponential functions. The average fits for each sample set are presented in Table 2.3. Although swelling of the PSS may contribute to this response [49], the full understanding of the underlying mechanisms has yet to be done. However, one can possibly draw a few conclusions from the fit parameters. The first exponential region has a higher sensitivity than the second by about double. This slowing is perhaps due to diffusion of water into the thin film, rather than direct surface absorption when at equilibrium. It should be pointed out that many groups have also found the humidity effect on CNT thin films to be non-linear, and to the best of our knowledge, only limited research has been done to investigate this phenomenon [22, 49, 50].

2.5 Conclusions

In this work, $(MWNT\text{-}PSS/PVA)_n$ films were manufactured via a layer-by-layer deposition process and directly deposited onto GFRP substrates. These thin films have been characterized for their sensitivity

Table 2.3. Fitted parameters of DC resistance response to monotonically increasing humidity.

Number of Bilayers	H_1	f_1 [%RH]$^{-1}$	H_2	f_2 [%RH]$^{-1}$	H_{Tr} [%RH]
50	$1.01 \pm 0.31 \times 10^{-4}$	0.130 ± 0.002	$3.13 \pm 0.68 \times 10^{-3}$	$5.56 \pm 0.08 \times 10^{-2}$	47.1 ± 0.24
75	$1.08 \pm 0.05 \times 10^{-4}$	0.128 ± 0.001	$3.39 \pm 0.15 \times 10^{-3}$	$5.51 \pm 0.06 \times 10^{-2}$	47.6 ± 0.04
100	$1.07 \pm 0.19 \times 10^{-4}$	0.132 ± 0.005	$3.46 \pm 0.33 \times 10^{-3}$	$5.62 \pm 0.12 \times 10^{-2}$	46.8 ± 0.88
150	$1.87 \pm 0.45 \times 10^{-4}$	0.118 ± 0.022	$2.37 \pm 0.28 \times 10^{-3}$	$6.13 \pm 0.19 \times 10^{-2}$	46.1 ± 0.73

to applied mechanical strain and to environmental changes due to temperature and humidity. Films loaded with monotonically increasing strain to failure demonstrated electrical sensitivity in the time- and frequency domains in a linear-quadratic response. It was found that components of the frequency-domain response have higher sensitivity to incurred damage than time-domain DC resistance measurements. Thin film electrical responses to three-cycle dynamic loads to two strain regimes were characterized. It was determined that they continued to function throughout these tests with minimal drift. High-cycle dynamic tests demonstrated the low level drift in the electrical measurements over 1,000 cycles of low level strain. To determine the sensitivity to thermal changes, the thermal response of the thin films were measured from 20 °C to 100 °C. From these tests, it was found that the $(MWNT\text{-}PSS/PVA)_n$ thin films respond to temperature in a manner more like SWNTs than MWNTs. Finally, the sensitivity of the thin films to humidity was characterized between 35 %RH and 80%RH, and the thin film response was found to be bi-exponential in nature. In conclusion, the results produced by this study have brought together a better understanding of the electrical responses of LbL carbon nanotube-based films subjected to mechanical, thermal, and hygroscopic variation.

Chapter 2 References:

[1] B. Roeseler, B. Sarh, M. Kismarton *et al.*, "Composite Structures – The First 100 Years," in Composite Design Tutorial, Stanford University, 2009.

[2] S. Nolet, "Manufacturing of Utility-Scale Wind Turbine Blades," in Iowa Wind Energy Assoc. 2010 IAWIND Conf., Ames, IA, 2010.

[3] M. V. Rosenker, "Safety Recommendation A-06-27 and -28," National Transportation Safety Board, ed., 2006.

[4] F. Bastianini, M. Corradi, A. Borri *et al.*, "Retrofit and monitoring of an historical building using "Smart" CFRP with embedded fibre optic Brillouin sensors," *Construction and Building Materials*, vol. 19, no. 7, pp. 525-535, 2005.

[5] H. Park, H. Sohn, K. Law *et al.*, "Time reversal active sensing for health monitoring of a composite plate," *Journal of Sound and Vibration,* vol. 302, no. 1-2, pp. 50-66, 2007.

[6] A. Mirmiran, and Y. Wei, "Damage assessment of FRP-encased concrete using ultrasonic pulse velocity," *Journal of Engineering Mechanics,* vol. 127, no. 2, pp. 126-135, 2001.

[7] M. A. Rumsey, and J. A. Paquette, "Structural Health Monitoring of Wind Turbine Blades," in SPIE Smart Structures / NDE, San Diego, CA, USA, 2008.

[8] Z. Qiu, X. Yao, J. Yuan *et al.*, "Experimental research on strain monitoring in composite plates using embedded SMA wires," *Smart Materials and Structures,* vol. 15, no. 4, pp. 1047-1053, 2006.

[9] H. Tsutsui, A. Kawamata, T. Sanda *et al.*, "Detection of damage of composites using embedded optical fibers," *Smart Materials and Structures,* vol. 13, pp. 1284-1290, 2004.

[10] H. Y. Tang, C. Winkelmann, W. Lestari *et al.*, "Composite Structural Health Monitoring Through Use of Embedded PZT Sensors," *Journal of Intelligent Material Systems and Structures,* vol. 22, no. 8, pp. 739-755, 2011.

[11] S. Iijima, "Helical microtubules of graphitic carbon," *Nature,* vol. 354, no. 6348, pp. 56-58, 1991.

[12] R. Baughman, A. Zakhidov, and W. De Heer, "Carbon nanotubes--the route toward applications," *Science,* vol. 297, no. 5582, pp. 787, 2002.

[13] T.-W. Chou, L. Gao, E. T. Thostenson *et al.*, "An assessment of the science and technology of carbon nanotube-based fibers and composites," *Composites Science and Technology,* vol. 70, no. 1, pp. 1-19, 2010.

[14] E. T. Thostenson, and T.-W. Chou, "Carbon nanotube networks: sensing of distributed strain and damage for life prediction and self healing," *Advanced Materials,* vol. 18, no. 21, pp. 2837-2841, 2006.

[15] M. Rein, O. Breuer, and H. Wagner, "Sensors and sensitivity: Carbon nanotube buckypaper films as strain sensing devices," *Composites Science and Technology,* vol. 71, no. 3, pp. 373-381, 2011.

[16] P. Dharap, Z. Li, S. Nagarajaiah *et al.*, "Nanotube film based on single-wall carbon nanotubes for strain sensing," *Nanotechnology,* vol. 15, pp. 379-382, 2004.

[17] I. Kang, M. J. Schulz, J. H. Kim *et al.*, "A carbon nanotube strain sensor for structural health monitoring," *Smart Materials and Structures,* vol. 15, pp. 737, 2006.

[18] K. J. Loh, J. P. Lynch, B. S. Shim *et al.*, "Tailoring piezoresistive sensitivity of multilayer carbon nanotube composite strain sensors," *Journal of Intelligent Material Systems and Structures,* vol. 19, no. 7, pp. 747-764, 2008.

[19] N. Hu, Y. Karube, M. Arai *et al.*, "Investigation on sensitivity of a polymer/carbon nanotube composite strain sensor," *Carbon,* vol. 48, no. 3, pp. 680-687, 2010.

[20] B. R. Loyola, V. La Saponara, and K. J. Loh, "In Situ Strain Monitoring of Fiber-Reinforced Polymers using Embedded Piezoresistive Nanocomposites," *Journal of Material Science,* vol. 45, no. 24, pp. 6786-6798, 2010.

[21] C. L. Cao, C. G. Hu, Y. F. Xiong *et al.*, "Temperature dependent piezoresistive effect of multi-walled carbon nanotube films," *Diamond and Related Materials,* vol. 16, no. 2, pp. 388-392, 2007.

[22] H. Yu, T. Cao, L. Zhou *et al.*, "Layer-by-Layer assembly and humidity sensitive behavior of poly(ethyleneimine)/multiwall carbon nanotube composite films," *Sensors and Actuators B: Chemical,* vol. 119, no. 2, pp. 512-515, 2006.

[23] National Instruments. "How Is Temperature Affecting Your Strain Measurement Accuracy?," May 5, 2012, 2012; http://www.ni.com/white-paper/3432/en.

[24] H. Patrick, G. Williams, A. Kersey *et al.*, "Hybrid fiber Bragg grating/long period fiber grating sensor for strain/temperature discrimination," *Photonics Technology Letters, IEEE,* vol. 8, no. 9, pp. 1223-1225, 1996.

[25] G. Decher, and J. B. Schlenoff, *Multilayer Thin Films,* Weinheim, Germany: Wiley-VCH, 2003.

[26] J. Schlenoff, and S. Dubas, "Mechanism of polyelectrolyte multilayer growth: Charge overcompensation and distribution," *Macromolecules,* vol. 34, no. 3, pp. 592-598, 2001.

[27] C. Chen, J. LaRue, and R. Nelson, "Materials Properties of Polymer Blends of Poly (3, 4-ethlenedioxythiophene)/Poly(styrenesulfonate)/N-Methyl-2-pyrrolidinone (PEDOT: PSS: NMP) and Polyvinyl Alcohol (PVA)," in Mater. Res. Soc. Symp. Proc., Warendale, PA, 2009.

[28] M. J. O'Connell, P. Boul, L. M. Ericson *et al.*, "Reversible water-solubilization of single-walled carbon nanotubes by polymer wrapping," *Chemical Physics Letters,* vol. 342, no. 3, pp. 265-271, 2001.

[29] Y. Zhao, B. R. Loyola, and K. J. Loh, “Mechanical and Viscoelastic Characterization of Layer-by-Layer Carbon Nanotube-Polyelectrolyte Thin Films,” *Smart Materials and Structures,* vol. 20, no. 7, pp. 075020, 2011.

[30] ASTM International, "ASTM Standard D3039: Standard Test Method for Tensile Properties of Polymer Matrix Composite Materials," *ASTM Standard D3039*, 2008.

[31] K. J. Loh, J. Kim, J. P. Lynch *et al.*, “Multifunctional layer-by-layer carbon nanotube polyelectrolyte thin films for strain and corrosion sensing,” *Smart Materials and Structures,* vol. 16, no. 2, pp. 429-438, 2007.

[32] J. Bauerle, “Study of solid electrolyte polarization by a complex admittance method,” *Journal of Physics and Chemistry of Solids,* vol. 30, no. 12, pp. 2657-2670, 1969.

[33] A. K. Kota, B. H. Cipriano, M. K. Duesterberg *et al.*, “Electrical and rheological percolation in polystyrene/MWCNT nanocomposites,” *Macromolecules,* vol. 40, no. 20, pp. 7400-7406, 2007.

[34] C. McClory, P. Pötschke, and T. McNally, “Influence of Screw Speed on Electrical and Rheological Percolation of Melt-Mixed High-Impact Polystyrene/MWCNT Nanocomposites,” *Macromolecular Materials and Engineering,* vol. 296, no. 1, pp. 59-69, 2011.

[35] S. De, P. E. Lyons, S. Sorel *et al.*, “Transparent, flexible, and highly conductive thin films based on polymer−nanotube composites,” *ACS Nano,* vol. 3, no. 3, pp. 714-720, 2009.

[36] Y. Ma, W. Cheung, D. Wei *et al.*, “Improved conductivity of carbon nanotube networks by in situ polymerization of a thin skin of conducting polymer,” *ACS Nano,* vol. 2, no. 6, pp. 1197-1204, 2008.

[37] I. Kang, M. Schulz, J. Kim *et al.*, “A carbon nanotube strain sensor for structural health monitoring,” *Smart Materials and Structures,* vol. 15, no. 3, pp. 737-748, 2006.

[38] E. T. Thostenson, and T.-W. Chou, “Real-time in situ sensing of damage evolution in advanced fiber composites using carbon nanotube networks,” *Nanotechnology,* vol. 19, no. 21, pp. 215713, 2008.

[39] Y. Shindo, Y. Kuronuma, T. Takeda *et al.*, “Electrical resistance change and crack behavior in carbon nanotube/polymer composites under tensile loading,” *Composites Part B: Engineering*, pp. 39-43, 2011.

[40] L. Gao, E. T. Thostenson, Z. Zhang *et al.*, “Coupled carbon nanotube network and acoustic emission monitoring for sensing of damage development in composites,” *Carbon,* vol. 47, no. 5, pp. 1381-1388, 2009.

[41] A. Kaiser, G. Düsberg, and S. Roth, “Heterogeneous model for conduction in carbon nanotubes,” *Physical Review B,* vol. 57, no. 3, pp. 1418–1421, 1998.

[42] T. M. Barnes, J. L. Blackburn, J. van de Lagemaat *et al.*, “Reversibility, Dopant Desorption, and Tunneling in the Temperature-Dependent Conductivity of Type-Separated, Conductive Carbon Nanotube Networks,” *ACS Nano,* vol. 2, no. 9, pp. 1968-1976, 2008/09/23, 2008.

[43] X. Wei, and C. Tianhong, “Characterization of layer-by-layer self-assembled carbon nanotube multilayer thin films,” *Nanotechnology,* vol. 18, no. 14, pp. 145709, 2007.

[44] J. C. Charlier, and J. P. Issi, “Electronic structure and quantum transport in carbon nanotubes,” *Applied Physics A: Materials Science & Processing,* vol. 67, no. 1, pp. 79-87, 1998.

[45] L. Langer, V. Bayot, E. Grivei *et al.*, “Quantum transport in a multiwalled carbon nanotube,” *Physical review letters,* vol. 76, no. 3, pp. 479-482, 1996.

[46] W. Ding, S. Pengcheng, L. Changhong *et al.*, “Highly oriented carbon nanotube papers made of aligned carbon nanotubes,” *Nanotechnology,* vol. 19, no. 7, pp. 075609, 2008.

[47] M. Zhang, S. Fang, A. A. Zakhidov *et al.*, “Strong, Transparent, Multifunctional, Carbon Nanotube Sheets,” *Science,* vol. 309, no. 5738, pp. 1215-1219, August 19, 2005, 2005.

[48] C. K. M. Fung, and W. J. Li, "Ultra-low-power polymer thin film encapsulated carbon nanotube thermal sensors." pp. 158-160.

[49] B. S. Shim, W. Chen, C. Doty *et al.*, “Smart electronic yarns and wearable fabrics for human biomonitoring made by carbon nanotube coating with polyelectrolytes,” *Nano letters,* vol. 8, no. 12, pp. 4151-4157, 2008.

[50] Q.-Y. Tang, Y. C. Chan, and K. Zhang, “Fast response resistive humidity sensitivity of polyimide/multiwall carbon nanotube composite films,” *Sensors and Actuators B: Chemical,* vol. 152, no. 1, pp. 99-106, 2011.

Chapter 3: Spatial Sensing Using Electrical Impedance Tomography

3.1 Abstract

The need for structural health monitoring has become critical, due to our aging infrastructure, legacy airplanes, and continuous development of new structural technologies. With updated structural design comes the need for new structural health monitoring paradigms that can sense the presence, location, and severity with a single measurement. This paper focuses on the first step of this paradigm, consisting of applying a sprayable conductive carbon nanotube-polymer film upon glass fiber-reinforced polymer composite substrates. Electrical impedance tomography is performed to measure changes in conductivity within the conductive films due to damage. Simulated damage is a method for validation of this approach. Finally, electrical impedance tomography measurements are taken while the conductive films are subjected to tensile and compressive strain states. This demonstrates the ability of electrical impedance tomography for not only damage detection, but active structural monitoring as well. This study acts as a first step towards moving the structural health monitoring paradigm towards large-scale deployable spatial sensing.

3.2 Introduction

Engineers are entrusted with ensuring the safety and longevity of a variety of structures in use today, which stem from the numerous engineering advances in the 20th century. These accomplishments include the U.S Interstate highway system, high-rise buildings, and propeller and jet-powered aircraft. However, this vital infrastructure is deteriorating as indicated by the 2009 ASCE report card's overall 'C' rating for safety of the bridges in the United States, while stating that the average bridge is 43 years old of a 50 year life span [1]. Another recent example includes a 2008 incident involving Southwest Flight 812 that

experienced a rapid depressurization of the cabin due to a rupture in the fuselage. This structural failure was attributed to fatigue cracking near riveted lap-joints [2]. Monitoring is also necessary for next-generation structures, such as fiber-reinforced composite-based aircraft, radar-evading naval vessels, and super-span suspension bridges among others, for any unexpected modalities of damage to develop. In 2005, two Airbus A-300 series aircraft had incidents where the fiber-reinforced composite skin of the aircrafts' rudders debonded. In one case, the disbond degraded the structural integrity of the rudder to the point where the rudder sheared-off of the aircraft in flight [3]. In another case involving a new structural design using traditional metals, numerous cracks have developed on the US Navy's Ticonderoga cruisers [4] and the next-generation Littoral Combat Ship U.S.S. Freedom [5], which have traditional steel hulls but have aluminum superstructures. Many of the cracks have developed at the bi-metal interfaces, above and below the water line. With the sheer magnitude of the work involved to monitor our increasing infrastructure, low-cost and automated systems will have to be implemented to aid in this colossal task.

To confront these problems, numerous research groups have developed means to implement a variety of sensing methodologies within real structures. One of these methods involved the implementation of a foil-based strain gauge network, which monitors for changes in the strain field of the structures. Some examples of this work have been applied to wind turbines [6], rail structures [7], and aircraft [8]. Other researchers have looked at the implementation of strain gauge networks with wireless systems [9]. Other groups have focused on using optical fiber Bragg gratings to measure strain and temperature in a wide array of structures, such as aircraft [10, 11], Navy fast patrol boats [12], spacecraft [13], rocket motors [14], and bridges [15-17]. The foil-based strain gauges and fiber Bragg gratings are point-based sensors that measure the strain and temperature at the point of application. To get a global view of the structure's health, interpolation and other methods are employed to determine structural degradation or damage development. Many researchers have chosen to implement networks of piezoelectric transducers and receivers, to propagate guided waves through the structure to detect potential damage. A few examples include implementation in aircraft [18], naval structures [19], civil infrastructure [20, 21], rail bridges [22], and spacecraft [23, 24]. Although acoustic- and ultrasonic-based approaches are typically much better at detecting damage away from sensor placement, there are still some issues with their effectiveness in structures with multiple interfaces, poor transmission properties (i.e. structural foams), and damage

detection when co-located with the damaged area. These systems leverage already proven, off-the-shelf technologies that have been used for a number of years, but still have issues that need to be solved or supplemented with another methodology to ensure complete and robust monitoring for a given structure.

In recent years, a newer field has emerged by developing a structural health monitoring methodology based on measuring the change in the electrical properties inherent to a structure or an applied conductive material to measure strain and detect damage within the structure. The increase in the use of carbon fiber-reinforced composites has allowed researchers to monitor for different aspects of structural health, by measuring the change in DC electrical resistance before, during, and after a loading event. Several groups have successfully detected strain [25-29], delamination [30-32], and traverse cracking [25, 33] in this material. For materials that are electrically nonconductive (i.e. glass fiber reinforced composites) or materials that are too conductive to have a resistance change above the noise threshold, thin films based on carbon nanotubes (CNTs) have been developed for application to the surface or embedded within materials with a layered construction like fiber-reinforced composites. These films are capable of sensing strain [34-39], cracks [40, 41], temperature [42-44], humidity [45-47], and changes in pH [48]. All of these measurements were done using 2- or 4-point probe resistance measurements, where the change in electrical properties is measured between the inner electrodes. If strain or damage is incurred within the gauge section of the sensor, the effect is registered by the measurement, but the location of damage cannot be determined. Although multiple measurements taken in a hash pattern can resolve this problem, this approach still leads to poor resolution and necessitates a large number of measurements.

A method called electrical impedance tomography (EIT) has been a focus of medical and geophysical research for the past 30 years, but has been relatively overlooked by the SHM community until very recently. EIT allows for the reconstruction of the spatially distributed conductivity within a sensing area bounded by a set of electrodes. However, the reconstruction of this distributed conductivity is ill-posed, and a solution has only been available since Calderon's paper in 1980 [49]. Once Calderon's strategy for conductivity reconstruction was discovered, numerous research groups have improved on this strategy by developing linear [50-54] and non-linear [51, 54-57] reconstruction algorithms depending on the topology of the conductivity distribution. Also, these reconstructions can be performed for absolute or differential imaging, where the actual or change in conductivity can be determined, respectively. The EIT

community has developed a MATLAB script suite called Electrical Impedance Tomography and Diffuse Optical Tomography Reconstruction Software (EIDORS) [58]. Despite this progress, only a few groups have released research relating to applying EIT to applied conductive films for SHM purposes. Lazarovitch et al. [59] demonstrated the ability to monitor changes in conductivity using a carbon film, with potential applications to impact damage monitoring. Pyo et al. [60], Hou et al. [61], and Loh et al. [62] have published on the use of EIT for applied monitoring using a layer-by-layer CNT-polyelectrolyte thin films for strain, impact, pH, and corrosion detection. However, these studies involved sensitive thin films that cannot be easily or cheaply scaled up for large engineering structures.

To bring EIT closer to a large-scale SHM methodology, an easily deployable conductive medium needs to be developed and shown to work in conjunction with EIT for spatially distributed sensing to changes in conductivity. In this study, these very accomplishments are demonstrated through the development of a multi-walled carbon nanotube (MWNT)-polyvinylidene fluoride (PVDF) latex-based film that can be spray-deposited on surfaces of unlimited size. Furthermore, these films are used as a sensitive conductive medium for performing EIT measurements, and thus monitor for changes in conductivity due to applied strain and simulated damage. The purpose of this work is to show that EIT is ready for serious attention as a field deployable SHM methodology.

3.3 Electrical Impedance Tomography

Electrical impedance tomography is a soft-field tomographic method that allows for the reconstruction of the 2D or 3D spatially distributed conductivity of a conductive medium that is bounded by electrodes. A typical measurement entails propagating a current between two electrodes and measuring the corresponding differential voltage at the remaining adjacent electrodes. Specifically, a current is injected into one electrode and another electrode is connected with ground. These measurements are performed for a set of current injections, called a current injection pattern. The corresponding boundary voltage measurements are correlated to the spatially distributed conductivity via Laplace's equation:

$$\nabla \cdot (\sigma \nabla u) = 0 \tag{3.1}$$

Typically, the forward problem is solved where the conductivity distribution (σ) is known and the voltage distribution (u) across the conductive medium is solved. However, the purpose of EIT is to solve the inverse problem, or the exact opposite of this case. Inevitably, the forward problem is solved in some form

while performing the inverse problem calculation. As analytical solutions are not typically available for most geometries, a numerical approach is taken using the finite element method (FEM). The weak formulation of Laplace's equation is developed, which results in (3.2):

$$\iint_{\Omega} \sigma_{\Omega} \nabla \phi \nabla u dx dy = 0 \tag{3.2}$$

In the case of this study, a 2D approach is taken using triangular elements, where (2) is performed over the area of each of these elements (Ω). In this FEM formulation, piece-wise linear shape functions are used to account for the voltage at each node. To properly model the effects of electrode contact resistance, the complete electrode model [63] is applied, where:

$$\int_{E_l} \sigma \frac{\partial u}{\partial \upsilon} ds = I_l \tag{3.3}$$

$$u + z_l \sigma \frac{\partial u}{\partial \upsilon} = V_l \tag{3.4}$$

At the current injection electrode (l), the boundary conduction problem is governed by (3), where the current is injected normal (υ) to the boundary at the electrode at a magnitude of I_l. Due to the electrode contact resistance (z_l), a voltage drop occurs between the electrode and the conductive medium. The grounded electrode is accounted for by (4), where the corresponding mesh voltage is u and V_l is the electrode voltage. The FEM discretization of (*1*) with the corresponding boundary conditions (3) and (4) is solved in matrix form for each current injection for the corresponding voltage distribution and the boundary electrode boundaries simultaneously [56].

To perform the EIT conductivity reconstruction, the absolute or differential distributed conductivity image can be reconstructed. Absolute imaging uses one set of electrode voltage measurement to reconstruct the actual conductivity within the sensing area of the measurement. Differential imaging uses two sets of EIT voltage measurements in time to reconstruct the change in the conductivity reconstruction. Previous work has shown that differential imaging is more stable [64] and for the purposes of SHM is more applicable than absolute imaging because decreases in conductivity are typically indicative of the onset of damage.

In this work, we discuss a normalized differential imaging reconstruction method called Maximum a Posteriori (MAP), developed by Adler and Guardo [50]. In general, MAP is a one-step linear

reconstruction method that requires relative changes in conductivity to be less than a ±100 % change in conductivity, for the reconstruction to be accurate. The advantage of using this method is a lower dependence of the reconstruction on the knowledge of the exact boundary electrode contact resistances and the current used for the injections. To perform this type of imaging, two sets of boundary voltage measurements are required, where the difference of the measurements is divided by the initial voltage measurements for normalized differential voltage values. These values are used in conjunction with the MAP reconstruction equation in (3.5), to determine the normalized change in conductivity:

$$\frac{\Delta\sigma}{\sigma_0} = \left(H^T W H + \lambda R\right)^{-1} H^T W \left(\frac{\Delta V}{V_0}\right) \tag{3.5}$$

The matrix H is the sensitivity matrix that correlates the normalized change in boundary electrode voltage to a change in the spatial normalized change in the conductivity. The calculation of the sensitivity matrix is fully outlined by Adler and Guardo [50]. To incorporate the effect of Gaussian white noise in the voltage measurements, the variance of these measurements are used in the W matrix where:

$$W_{i,i} = \frac{1}{\alpha_i} \tag{3.6}$$

The variable α_i is the variance of the corresponding boundary voltage measurement *i*. Due to the ill-posed nature of the reconstruction; regularization is implemented for stabilization of the calculation, in the form of a regularization matrix R and a regularization hyperparameter λ. The regularization matrix typically implements some sort of smoothing in the reconstruction, using approaches such as Tikhonov [65], NOSER [52], discrete Laplacian filtering [66], and Gaussian high-pass filtering [50]. In this study, the Gaussian high-pass filter regularization matrix will be used due to the proven efficacy in conjunction with the MAP algorithm. To determine the scalar value of the regularization hyperparameter, the noise figure (NF) metric will be implemented. First discussed by Adler and Guardo [50] and refined by Graham and Adler [64], the NF metric mandates that the signal-to-noise ratio of the reconstructed normalized differential conductivity distribution be a specified multiple of the signal-to-noise ratio of the normalized differential voltage measurements used for the reconstruction. This calculation is performed for a representative system for which future reconstructions will be performed with a small contrast of 50 % in the center of the sensing area. This contrast can be negative to positive; whichever best relates to the

sensing that will be conducted. In this study, an NF of 1 was used. Upon the determination of the regularization hyperparameter, the MAP linear reconstruction equation is fully determined and reconstruction for the sensing system defined by its components can now be conducted.

3.4 Experimental Methods

In order for EIT to be used for SHM purposes with non-conductive materials, a conductive material must be deposited, as is the case with glass fiber reinforced polymer (GFRP) composites. The present work utilized a conductive MWNT-PVDF latex-based film that was spray-deposited on large surface areas. The capability of the EIT method was then tested for sensitivity to complex shaped conductivity distributions, as a method for validation of the distributed sensing. Finally, applied films on GFRP specimens were characterized for their strain sensitivity in conjunction with the EIT methodology.

3.4.1 MWNT-PVDF Latex Coating

The MWNT-PVDF films were based on a two-part system that allowed for shelf stable solutions. When combined, it led to a robust, conductive film. The first part of the solution contained the polymer matrix that was bought as a latex solution of 150 nm particles of PVDF (Kynar Aquatec RC-10,206, Arkema Inc.). This solution was adjusted with water to ensure that the resulting mixed paint had a specific weight percentage of solids to water. The other solution contains the conductive MWNTs (SWM100, SWeNT) that were stably suspended in water using poly(sodium 4-styrenesulfonate) (PSS) (~1 MW, Sigma-Aldrich) and the addition of the polar solvent N-methyl-2-pyrrolidone (NMP) (Sigma-Aldrich). NMP acts as a coalescing agent of the PVDF, that facilitates the forming of the film when used in an amount of 3 wt.% compared to the total mass of the PVDF particles. The amount of MWNTs is determined by a specified weight percentage of MWNTs in the fully dried film. In this study, 5 wt.% of MWNTs was used.

The conductive solution was formed starting with a 2 wt.% solution of PSS that was tip-sonicated for 10 min, or until completely dissolved. To the PSS solution, NMP and powder-form MWNTs were added prior to 30 min of tip-sonication. During tip-sonication, the PSS polymer wraps [67] the MWNTs to ensure an enduring dispersion and suspension, while the NMP also acts as a dispersing agent for MWNTs [68]. The PVDF latex solution was produced by combining the PVDF latex solution and an appropriate

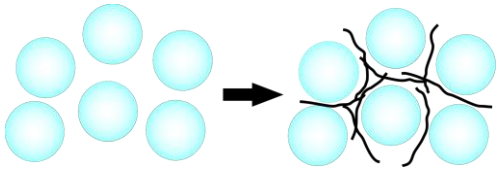

Figure 3.1. An illustration of the segregated MWNT network within the PVDF latex solution prior to film formation.

amount of DI water diluent to make a resulting combined paint that is 13 wt.% solid content, including the PVDF and the MWNTs. To produce the final paint solution, the conductive ink and the PVDF solution are combined and thoroughly mixed. The resulting paint started to immediately thicken due to shear thickening by the MWNTs, and the onset of coalescence from the NMP. This mixing created a segregated network of the MWNTs between the PVDF particles, as illustrated in Figure 3.1. At this point, the conductive paint was sprayed onto a substrate using an airbrush (VL, Paasche). Once sprayed, the paint rapidly begins to dry due to evaporation. The painted specimens were placed in a 60 °C oven for 10 minutes, to fully evaporate the water. As the water evaporated, the NMP fully coalesced the PVDF particles, locking in the MWNT network. The resulting film and representative MWNT network is shown in the scanning electron microscopy (SEM) image in Figure 3.2.

3.4.2 EIT Measurements

In order to conduct the EIT measurements, current needs to be injected into one electrode, another electrode needs to be set to ground, and the remaining electrodes need to be measured for the corresponding voltage response. To do this, each electrode around a sensing skin is connected to a matrix switch (34923A, Agilent Technologies) which is attached to a data acquisition unit (34980A, Agilent Technologies). To provide current and ground, a Keithley 6221 AC and DC Current Source was used in conjunction with the analog inputs of the 34980A. The current injection pattern for all of the EIT measurements in this study are between two electrodes directly across from one another, as shown in Figure 3.3, where each blue line represents one injection-ground pair. A full EIT measurement consists of the boundary voltage measurements corresponding to subsequent application of these pairs. To prevent voltage measurements that are affected by electrode contact resistance, voltage measurements involving the injecting or grounded electrodes are not included in measurements.

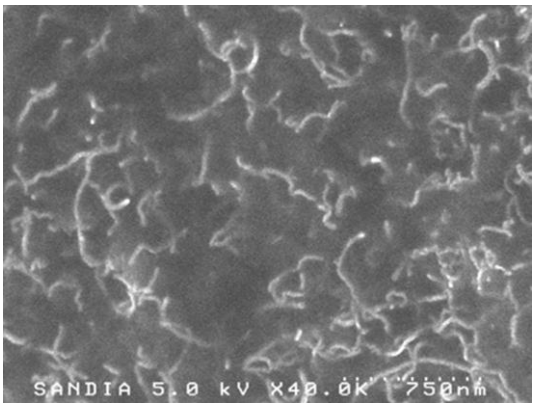

Figure 3.2. A scanning electron microscopy image of the surface of a MWNT-PVDF film.

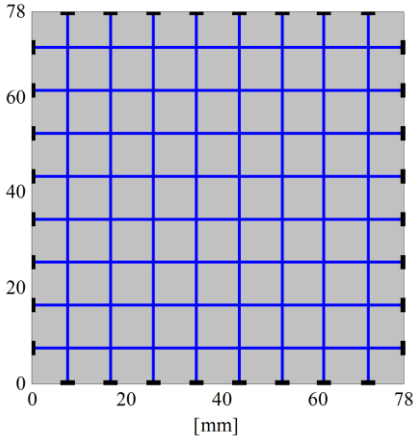

Figure 3.3. The current injection pattern used in this study, where the blue lines indicate the generalized current path.

3.4.3 EIT Validation

As a way to validate the responses from the MAP reconstruction algorithm, several conductivity patterns were spray-deposited with the airbrush onto pre-cured GFRP substrates, using masked patterns. The GFRP substrates were prepared with a 100 grit diamond abrasion pad and cleaned with isopropanol and then acetone. The masks for the electrodes, sensing area, and conductivity patterns were cut from overhead transparency film, using a CNC laser cutter. Specifically, the masked area included eight 3 mm square electrode pads extended from each edge of the 78×78 mm^2 sensing area, as shown in Figure 3.4. The electrodes were placed 6 mm apart from each other. These electrodes pads facilitated easier placement of the electrodes during specimen preparation. The masks were applied to the substrates using double-backed masking tape. All of the substrates contained conductivity pattern masks except for one substrate. This homogeneous conductivity pattern was used as the baseline measurement for the normalized differential imaging. All of the substrates were lined up, and the MWNT-PVDF paint was spray-deposited on all of the substrates at one time, to ensure a consistent coating as possible. After 50% of the paint was spray-deposited, all the conductivity pattern masks were removed, and the remaining 50% paint was applied. The specimens were then dried in a 60 °C oven for 10 minutes. After the film coalesced, 30 AWG wires were attached to each electrode pad using colloidal silver paint (Ted Pella). As can be seen in Figure 3.4, this specimen has been masked with a 6 mm wide cross that is 54 mm long in the vertical and horizontal directions.

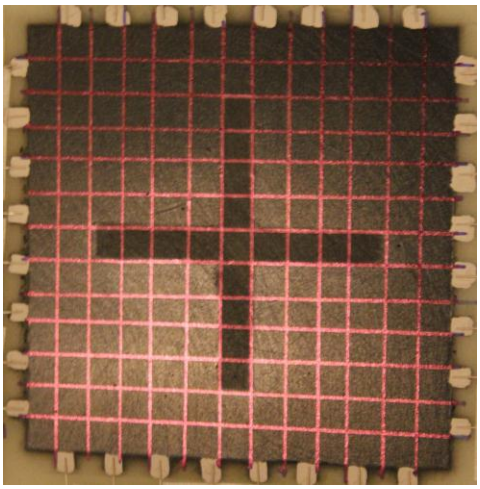

Figure 3.4. A photograph of an EIT validation specimen that has a 6 mm-wide cross contrast in the center. The lines indicate the grid where 4-pt probe resistance measurements were taken.

EIT measurements were taken for each specimen using a current injection magnitude of 100 μA. After the EIT measurements were completed, grids of 6 mm by 6 mm squares were drawn on each specimen (as shown in Figure 3.4), and 4-pt probe resistance measurements were taken in each square. Using the resistance values, the conductivity distribution for each specimen was measured and normalized difference values were calculated for each specimen in respect the homogeneous MWNT-PVDF film. These measured conductivity distributions serve as the validation for the EIT reconstructions.

3.4.4 MWNT-PVDF Piezoresistivity Characterization

Prior to characterizing the strain sensitivity of the MWNT-PVDF with EIT, the strain sensitivity of the films was characterized using 2-pt probe resistance measurements as a point of comparison. MWNT-PVDF thin films were formulated with 3 wt.% MWNTs and spray deposited on cured GFRP substrates. These substrates were manufactured using a hand-layup process, where a single layer of quasi-unidirectional glass fiber weave (type 7715, Applied Vehicle Technology) was infused with a two-part epoxy (125/237, Pro-Set Inc.). The composite was cured for 15 h at 27 °C and then for 8 h at 80 °C. Once the deposited films were coalesced, the substrates were cut into 3 mm by 75 mm strips with the 0° in the longitudinal direction. This follows the 1:11 width-to-length ratio recommended by the ASTM D 3039 standard for tensile testing composites. To create electrical connections to the specimens, two 30 AWG wires were attached to the surface of the film, spaced 28 mm apart, using conductive colloidal silver paint (Ted Pella). While loading these specimens in tension, serrated grips were used to transfer the load to the

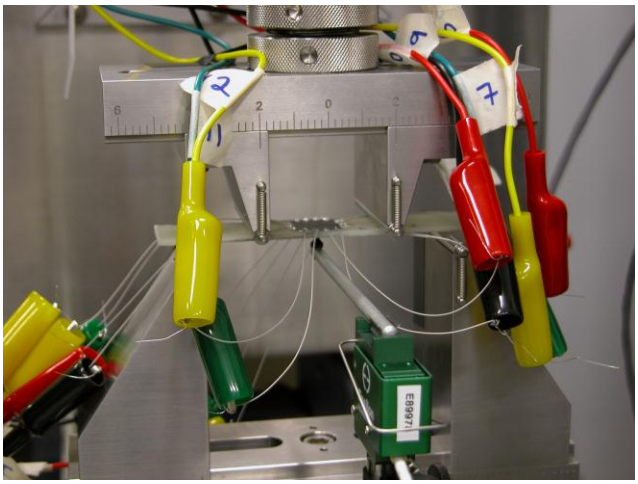

Figure 3.5. A 4-pt. bending specimen placed in the flexure fixture.

specimens. To protect the specimens from the grips, G-10 GFRP tabs were adhered using aircraft-grade epoxy (Hysol 903, Henkel Corp.). The tabs were adhered so as to create a 25 mm gauge length.

To measure the change in the 2-pt resistance measurements, each specimen was connected to a digital multimeter (34401A, Agilent Technologies) for DC resistance measurements. A load frame (150R, TestResources Inc.) was used to place the specimens in tension. The displacement of the load frame was verified using two laser displacement sensors (Microtrak II, MTI Instruments). To allow for the resistance measurements to be taken at prescribed strain values, a stepped-displacement profile was used. For a higher resolution at lower-strain values, the load frame was paused for 60 s every 1,000 με from 0 to 10,000 με and every 5,000 με until failure. This strain profile allowed for characterizing the full strain response of the DC resistance properties.

3.4.5 4-pt Bending Test Procedure

In order to characterize the ability of the EIT reconstruction to capturing the change in conductivity due to applied tensile and compression strains, an 18 mm by 18 mm sensing area was subjected to these strains, using 4-pt bending tests. These bending tests allow the specimens to be subjected to constant tensile or compression strain throughout the gauge length (between the inner supports of the fixture). The GFRP substrates were manufactured using a vacuum assisted resin transfer molding (VARTM) process, where unidirectional glass fiber mats (E-LR 0908, Vectorply) were infused with a two-part epoxy resin system (117LV/237, Pro-Set Inc.). The stack sequence for these panels was $[0°]_6$. The

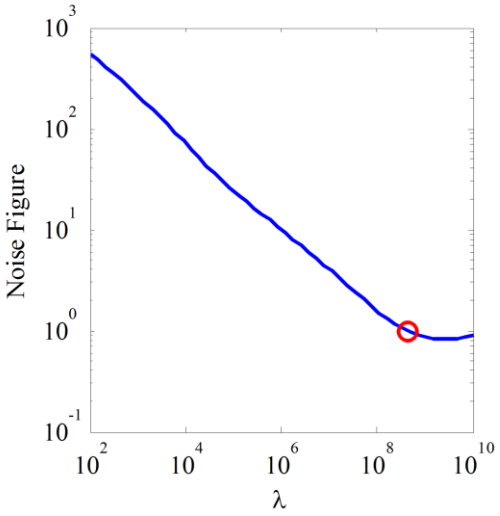

Figure 3.6. The noise figure is calculated for hyperparameters for a range from 10^2 to 10^{10}. The hyperparameter corresponding to an NF of 1 is equal to 4.54×10^8.

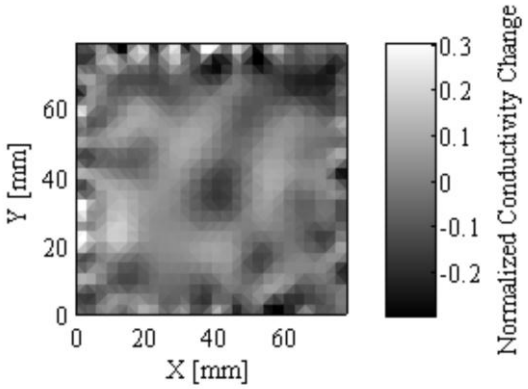

Figure 3.7. The EIT reconstruction for 6 mm center contrast and corresponds to the hyperparameter with a noise figure of 1.

infused panels were cured for 15 h at 27 °C and then for 8 h at 80 °C. Once cured, the specimens were cut into 25 mm by 127 mm specimens with the 0° fibers oriented in the longitudinal direction of the cut specimens. An 18×18 mm^2 area, with 2 mm square electrodes spaced 2 mm apart, were masked on the center of each specimen and sprayed with the MWNT-PVDF film. The electrodes were applied and attached to 30 AWG wire wrap using a silver-loaded epoxy (Hysol TRA-DUCT 2902, Henkel).

The ASTM D 7264 standard was consulted for the 4-pt flexural tests. The outer supports of the flexural fixture were placed 101.6 mm apart, while the inner supports were placed 50.8 mm apart. To put the MWNT-PVDF films in compression, the specimen was placed in the fixture with the film on the top face, as shown in Figure 3.5. To apply tensile strain, the specimens were placed in the fixture with the film facing down. The load frame (Satec 22EMF, Instron) was commanded to at a rate of 5 $mm\cdot min^{-1}$. The displacement was measured using a dilatometer connected to the load frame and placed at the center of the span. The films were subjected to tensile strain from 0 to 5,000 με in 1,000 με increments, and then subjected to compressive strain, at the same amplitudes. At each strain step, an EIT measurement was taken, while the load frame was paused. After all of the EIT measurements were taken, they were reconstructed with respect to the initial unstrained EIT measurement.

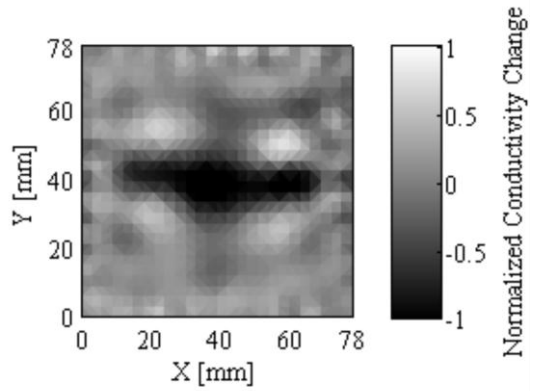

Figure 3.8. The EIT reconstruction for the conductivity distribution with a 6 mm-wide cross contrast in the center of the sensing area.

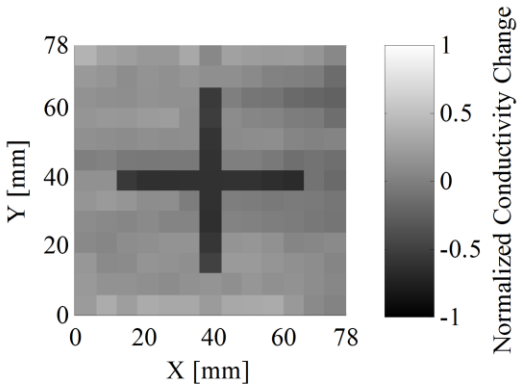

Figure 3.9. The measured conductivity distribution using 4-pt probe measurements for the specimen with a 6 mm cross contrast.

3.5 Results and Discussion

3.5.1 EIT Validation

3.5.1.1 Regularization Hyperparameter Determination

As stated previously, the regularization parameter is determined using a contrast between a homogeneous film and one with a small area in the center with a 50% decrease in conductivity. In this case, a 6 mm square at the center of a film was masked to act as the contrast area. The film looks like the specimen in Figure 3.4, except only the very center square has been masked. To determine the appropriate regularization hyperparameter, the reconstruction algorithm is run for a range of hyperparameters logarithmically spaced between 10^2 and 10^{10}. For each reconstruction, the noise figure is calculated. These responses are plotted on the logarithmic plot in Figure 3.6. The hyperparameter that corresponds to a noise figure of 1 is labeled with a red circle, and its exact value is 4.54×10^8. The reconstruction that corresponds to this hyperparameter is shown in Figure 3.7. The contrast in the center can be easily seen.

3.5.1.2 EIT Reconstruction

Using the regularization parameter reported in section 3.5.1.1, all of the validation specimens were reconstructed in reference to the homogeneous MWNT-PVDF film specimen. The resulting reconstruction for the specimens with a masked cross in the center is shown in Figure 3.8. The first point regarding this figure is the non-zero background. Because this reconstruction is a contrast between the homogeneous specimen and that with the masked cross, the non-masked areas will still not have the same conductivity

background, due to the non-uniform method of spray-deposition by hand. However, the conductivity distribution taken using the 4-pt probe measurements is shown in Figure 3.9 and generally verifies the conductivity pattern reconstructed by the EIT method. In Figure 3.9, there is a line of conductivity decrease in the top right side at a y coordinate of about 60 mm. This is presumably due to an effect of the spray deposition, as the sprayer is swept in a horizontal direction across the substrates. The same decrease in conductivity is captured in the reconstruction. In addition, there are four areas of increased conductivity change in the EIT reconstruction that are not present in the actual conductivity distribution map. These are most possibly due to an effect that occurs with all EIT reconstructions, especially with sharp contrasts as in these specimens. A small region of opposite conductivity change will bound an area of actual contrast with a much lower magnitude. This small artifact is present in all reconstructions done for this study and is also observed in other studies [50, 64]. In the case of the cross contrast reconstruction, it is thought that this effect becomes exaggerated within the internal corners of the cross. Finally, the horizontal part of the cross is better resolved than the vertical portion of the cross. This is thought to be due to effects of the high pass filter with the triangular mesh as opposed to a square mesh. In the previously reviewed work, the example reconstructions are always of round or square contrasts, so it is not known if these affects are present in those reconstruction approaches as well. However despite these aspects of the reconstruction, this EIT approach is highly capable of capturing the complex shape of the cross contrast, as well as other smaller contrasts, like the 6 mm contrast used for determining the hyperparameter.

3.5.2 EIT Strain Response

Prior to discussing the EIT strain sensitivity, the piezoresistivity of the films is examined from the 2-pt probe resistance measurements, as a point of comparison. To facilitate a more straight forward comparison, the resistance measurements were converted to conductance using Equation 3.7:

$$G = \frac{1}{R} \tag{3.7}$$

Furthermore, the percent change of the conductance was calculated for each strain value using Equation 3.8:

$$\Delta G = \frac{G - G_0}{G_0} \times 100 \tag{3.8}$$

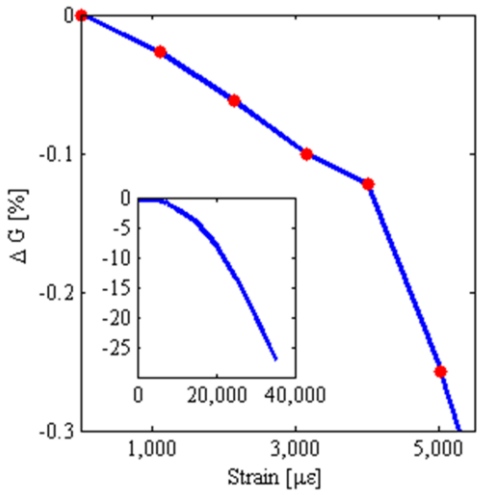

Figure 3.10. The 2-pt conductance response of the MWNT-PVDF film to applied strain over the strain regime which the EIT measurements were taken. The inset plot is the full strain response of the 2-pt conductance measurements and has the same axes as the larger plot.

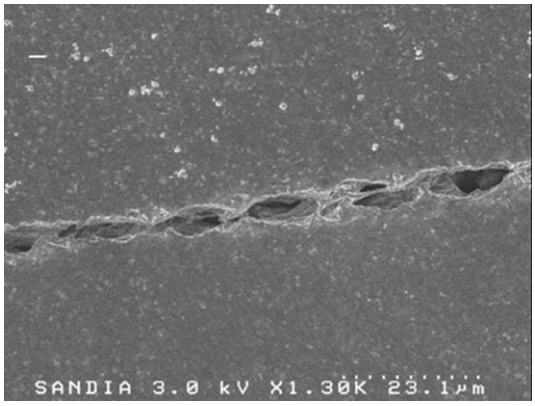

Figure 3.11. A scanning electron microscopy image of a tear the in a MWNT-PVDF film deposited on a GFRP substrate that has been subject to tensile strain to failure.

These corresponding measurements are plotted as a function of strain in Figure 3.10. The main plot is the low-strain response from 0 to 5,000 με, which are the same tensile strain levels that the EIT measurements were subjected to. The full strain conductance strain response is presented in the inset plot.

As illustrated in the inset plot in Figure 3.10, the strain responses of the MWNT-PVDF films are bi-functional, with the lower strain response as linear until 4,000 με. The calculated linear gauge factor of these films is -0.481±0.163. At 4,000 με, the response becomes non-linear, which has been seen previously [37, 40, 41] as an indication that the film is undergoing cracking. To validate this, surface scanning electron microscopy (SEM) images were taken of a tested film. A representative SEM image is presented in Figure 3.11. From the image, one can see that the underlying substrate has cracked, leading to a tear in the film. However, a full characterization of this conductance strain response is out of the scope of the present text and is reserved for the future.

To determine if the MAP reconstruction scheme is sufficiently sensitive to perform structural health monitoring, low-level tensile and compressive strain were subjected to the MWNT-PVDF. The corresponding EIT measurements were reconstructed in reference to the initial unstrained EIT measurements for each test. The hyperparameter is determined using the methodology laid out in section

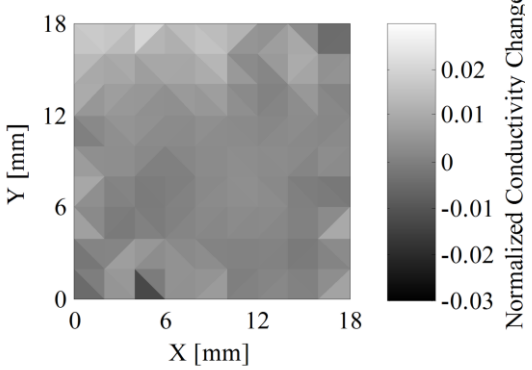

Figure 3.12. The EIT reconstruction for a MWNT-PVDF film subjected to 3,000 με.

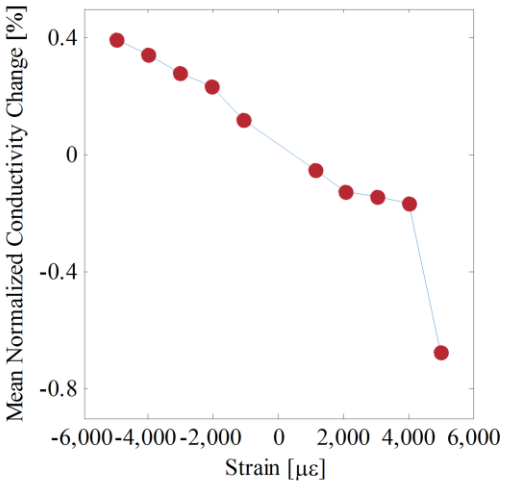

Figure 3.13. The strain response as measured using the mean value of the reconstructed conductivity distributions for a range of compressive and tensile strain values.

3.5.1.1, using a 2 mm square contrast at the center of an 18 mm by 18 mm sensing area. From the mechanical tests, a representative reconstruction response is shown in Figure 3.12. The center of the reconstructed conductivity distribution is relatively similar, but deviations can be seen near the boundaries of the reconstruction. This is partially due to the effects by strain on the electrodes that changes the contact resistance. This can have a significant effect on the reconstruction, but in this case these effects are relatively minor.

To characterize the MWNT-PVDF conductivity strain response using the EIT method, the mean value of the conductivity distribution is calculated for each strain state. This is then plotted as a function of strain as shown in Figure 3.13. As illustrated, the strain response is linear from about -5,000 με to 4,000 με. Within this linear region, the gauge factor is calculated as -0.55. This closely compares to the strain gauge calculated for the 2-pt probe responses to lower values of applied strain. After 4,000 με, a non-linear response is observed, as is consistent with the 2-pt conductance measurements discussed previously.

3.6 Conclusion

In this paper, spatially distributed sensing was performed using a spray-deposited MWNT-PVDF film and electrical impedance tomography. The latex-based MWNT-PVDF film enabled the capacity for sensing over much larger areas than was previously demonstrated. In addition, the application of the linear reconstruction method called Maximum a Posteriori was discussed and characterized for detection of

changes in conductivity distributions of MWNT-PVDF films when applied to the surface of GFRP composites. First, the capability of the algorithm was demonstrated by reconstructing the difference in conductivity between a homogeneous conductivity and one with a tailored conductivity distribution due to masking during the spray deposition. Finally, the MAP algorithm's sensitivity to small changes in conductivity due to applied strain to the MWNT-PVDF films was characterized. This sensitivity was compared to that measured by 2-pt conductance measurements and proven to be as effective. In addition to the spatial sensitivity, the MAP algorithm facilitated faster reconstruction times that previously demonstrated for SHM purposes, enabling real-time sensing using EIT. This work provides a further step towards facilitating a paradigm shift in SHM to the use of spatially distributed sensing based on electrical impedance tomography.

Chapter 3 References:

[1] American Society of Civil Engineers, *2009 Report Card for America's Infrastructure*, 2009.

[2] P. Knudson, "NTSB Continues Investigation of Southwest Airlines Flight 812," National Transportation Safety Board, ed., 2011.

[3] M. V. Rosenker, "Safety Recommendation A-06-27 and -28," National Transportation Safety Board, ed., 2006.

[4] C. P. Cavas, "Cracks plague Ticonderoga-class cruisers," *The Navy Times*, Gannett Government Media Company, 2010.

[5] S. Ritchey, N. Adler, and M. Pischel, "Crack Monitoring Survey During Rough Water Trials Period #2," Naval Surface Warfare Center - Carderock, ed., 2011.

[6] M. A. Rumsey, and J. A. Paquette, "Structural Health Monitoring of Wind Turbine Blades," in SPIE Smart Structures / NDE, San Diego, CA, USA, 2008.

[7] D. Barke, and W. Chiu, "Structural health monitoring in the railway industry: a review," *Structural Health Monitoring,* vol. 4, no. 1, pp. 81-93, 2005.

[8] S. R. Hunt, and I. G. Hebden, "Validation of the Eurofighter Typhoon structural health and usage monitoring system," *Smart Materials and Structures,* vol. 10, no. 3, pp. 497, 2001.

[9] C. Haksoo, C. Sukwon, and C. Hojung, "Structural Health Monitoring system based on strain gauge enabled wireless sensor nodes." pp. 211-214.

[10] D. Betz, L. Staudigel, and M. N. Trutzel, "Test of a fiber Bragg grating sensor network for commercial aircraft structures." pp. 55-58 vol.1.

[11] A. Cusano, P. Capoluongo, S. Campopiano, A. Cutolo, M. Giordano, F. Felli, A. Paolozzi, and M. Caponero, "Experimental modal analysis of an aircraft model wing by embedded fiber Bragg grating sensors," *Sensors Journal, IEEE,* vol. 6, no. 1, pp. 67-77, 2006.

[12] H. Sohn, C. Farrar, N. Hunter, and K. Worden, *Applying the LANL Statistical Pattern Recognition Paradigm for Structural Health Monitoring to Data from a Surface-Effect Fast Patrol Boat*, vol. LA-13761-MS, Los Alamos National Laboratory, 2001.

[13] E. Wolfgang, L. Ines, W. Reinhardt, R. Arnd, and G. Roland, "Fibre optic sensor network for spacecraft health monitoring," *Measurement Science and Technology,* vol. 12, no. 7, pp. 974, 2001.

[14] C. Xinlong, H. Xiangyong, H. Jianghua, and L. Jinjun, "Experimental Research on Embedded Fiber Bragg Grating Sensors Network for Solid Rocket Motors Health Monitor," in First International Conference on Intelligent Networks and Intelligent Systems, Wuhan, China, 2008, pp. 170-173.

[15] H.-N. Li, D.-S. Li, and G.-B. Song, "Recent applications of fiber optic sensors to health monitoring in civil engineering," *Engineering Structures,* vol. 26, no. 11, pp. 1647-1657, 2004.

[16] R. C. Tennyson, A. A. Mufti, S. Rizkalla, G. Tadros, and B. Benmokrane, "Structural health monitoring of innovative bridges in Canada with fiber optic sensors," *Smart Materials and Structures,* vol. 10, no. 3, pp. 560, 2001.

[17] Z. Zhou, and J. Ou, "Development of FBG Sensors for Structural Health Monitoring in Civil Infrastructures Sensing Issues in Civil Structural Health Monitoring," F. Ansari, ed., pp. 197-207: Springer Netherlands, 2005.

[18] J. B. Ihn, and F. K. Chang, "Pitch-catch active sensing methods in structural health monitoring for aircraft structures," *Structural Health Monitoring,* vol. 7, no. 1, pp. 5-19, 2008.

[19] S. S. Kessler, E. B. Flynn, and M. D. Todd, "Hybrid Coherent/Incoherent Beam Forming Diagnostic Approach to Naval Assets," 2011.

[20] A. Gunasekaran, S. Cross, N. Patel, and S. Sedigh, "Recent enhancements to and applications of the SmartBrick structural health monitoring platform," in Smart Structures and Materials and Nondestructive Evaluation and Health Monitoring, San Diego, CA, 2012, pp. 83450S.

[21] J. Wu, S. Yuan, S. Ji, G. Zhou, Y. Wang, and Z. Wang, "Multi-agent system design and evaluation for collaborative wireless sensor network in large structure health monitoring," *Expert Systems with Applications,* vol. 37, no. 3, pp. 2028-2036, 2010.

[22] T. Hay, S. Jayaraman, A. Ledeczi, P. Volgyesi, and R. Hay, "Railway Bridge Structural Health Monitoring Using Wireless Acoustic Emission Sensor Network."

[23] J. Yun, "Development of Structural Health Monitoring Systems Incorporating Acoustic Emission Detection for Spacecraft and Wind Turbine Blades," Electrical and Computer Engineering, Virginia Tech 2011.

[24] A. Zagrai, D. Doyle, V. Gigineishvili, J. Brown, H. Gardenier, and B. Arritt, "Piezoelectric Wafer Active Sensor Structural Health Monitoring of Space Structures," *Journal of Intelligent Material Systems and Structures,* vol. 21, no. 9, pp. 921-940, 2010.

[25] K. Ogi, "A Model for Piezoresistance Behavior in a CFRP Cross-Ply Laminate with Transverse Cracking," *Journal of Solid Mechanics and Materials Engineering,* vol. 1, no. 8, pp. 975-985, 2007.

[26] M. Taya, W. Kim, and K. Ono, "Piezoresistivity of a short fiber/elastomer matrix composite," *Mechanics of materials,* vol. 28, no. 1-4, pp. 53-59, 1998.

[27] A. Todoroki, and J. Yoshida, "Electrical Resistance Change of Unidirectional CFRP Due to Applied Load," *JSME International Journal Series A Solid Mechanics and Material Engineering,* vol. 47, no. 3, pp. 357-364, 2004.

[28] S. Wang, and D. Chung, "Piezoresistivity in continuous carbon fiber polymer-matrix composite," *Polymer Composites,* vol. 21, no. 1, pp. 13-19, 2000.

[29] S. Wang, and D. Chung, "Negative piezoresistivity in continuous carbon fiber epoxy-matrix composite," *Journal of Materials Science,* vol. 42, no. 13, pp. 4987-4995, 2007.

[30] T. Akira, and U. Masahito, "Low-cost delamination monitoring of CFRP beams using electrical resistance changes with neural networks," *Smart Materials and Structures,* vol. 15, no. 4, pp. N75, 2006.

[31] A. Todoroki, "Delamination Monitoring Analysis of CFRP Structures using Multi-Probe Electrical Method," *Journal of Intelligent Material Systems and Structures,* vol. 19, no. 3, pp. 291-298, 2008.

[32] A. Todoroki, H. Kobayashi, and K. Matuura, "Application of electric potential method to smart composite structures for detecting delamination," *JSME International Journal, Series A: Mechanics and Material Engineering,* vol. 38, no. 4, pp. 524-530, 1995.

[33] H. Inoue, and K. Ogi, "Piezoresistance Behaviour of CFRP Cross-Ply Laminates with Transverse Cracking," *Key Engineering Materials,* vol. 334, no. 2, pp. 961, 2007.

[34] L. Böger, M. Wichmann, L. Meyer, and K. Schulte, "Load and health monitoring in glass fibre reinforced composites with an electrically conductive nanocomposite epoxy matrix," *Composites Science and Technology,* vol. 68, no. 7-8, pp. 1886-1894, 2008.

[35] I. Kang, M. J. Schulz, J. H. Kim, V. Shanov, and D. Shi, "A carbon nanotube strain sensor for structural health monitoring," *Smart Materials and Structures,* vol. 15, pp. 737, 2006.

[36] K. J. Loh, J. P. Lynch, B. S. Shim, and N. A. Kotov, "Tailoring piezoresistive sensitivity of multilayer carbon nanotube composite strain sensors," *Journal of Intelligent Material Systems and Structures,* vol. 19, no. 7, pp. 747-764, 2008.

[37] B. R. Loyola, V. La Saponara, and K. J. Loh, "In Situ Strain Monitoring of Fiber-Reinforced Polymers using Embedded Piezoresistive Nanocomposites," *Journal of Material Science,* vol. 45, no. 24, pp. 6786-6798, 2010.

[38] M. Rein, O. Breuer, and H. Wagner, "Sensors and sensitivity: Carbon nanotube buckypaper films as strain sensing devices," *Composites Science and Technology,* vol. 71, no. 3, pp. 373-381, 2011.

[39] S. Vemuru, R. Wahi, S. Nagarajaiah, and P. Ajayan, "Strain sensing using a multiwalled carbon nanotube film," *The Journal of Strain Analysis for Engineering Design,* vol. 44, no. 7, pp. 555-562, 2009.

[40] L. Gao, E. T. Thostenson, Z. Zhang, and T.-W. Chou, "Coupled carbon nanotube network and acoustic emission monitoring for sensing of damage development in composites," *Carbon,* vol. 47, no. 5, pp. 1381-1388, 2009.

[41] Y. Shindo, Y. Kuronuma, T. Takeda, F. Narita, and S. Y. Fu, "Electrical resistance change and crack behavior in carbon nanotube/polymer composites under tensile loading," *Composites Part B: Engineering,* pp. 39-43, 2011.

[42] C. L. Cao, C. G. Hu, Y. F. Xiong, X. Y. Han, Y. Xi, and J. Miao, "Temperature dependent piezoresistive effect of multi-walled carbon nanotube films," *Diamond and Related Materials,* vol. 16, no. 2, pp. 388-392, 2007.

[43] M. Shiraishi, and M. Ata, "Conduction mechanisms in single-walled carbon nanotubes," *Synthetic Metals,* vol. 128, no. 3, pp. 235-239, 2002.

[44] V. Skákalová, A. Kaiser, Y. S. Woo, and S. Roth, "Electronic transport in carbon nanotubes: From individual nanotubes to thin and thick networks," *Physical Review B,* vol. 74, no. 8, pp. 085403, 2006.

[45] B. S. Shim, W. Chen, C. Doty, C. Xu, and N. A. Kotov, "Smart electronic yarns and wearable fabrics for human biomonitoring made by carbon nanotube coating with polyelectrolytes," *Nano letters,* vol. 8, no. 12, pp. 4151-4157, 2008.

[46] Q. Y. Tang, Y. Chan, and K. Zhang, "Fast response resistive humidity sensitivity of polyimide/multiwall carbon nanotube composite films," *Sensors and Actuators B: Chemical,* vol. 152, no. 1, pp. 99-106, 2011.

[47] H. Yu, T. Cao, L. Zhou, E. Gu, D. Yu, and D. Jiang, "Layer-by-Layer assembly and humidity sensitive behavior of poly(ethyleneimine)/multiwall carbon nanotube composite films," *Sensors and Actuators B: Chemical,* vol. 119, no. 2, pp. 512-515, 2006.

[48] K. J. Loh, J. Kim, J. P. Lynch, N. W. S. Kam, and N. A. Kotov, "Multifunctional layer-by-layer carbon nanotube polyelectrolyte thin films for strain and corrosion sensing," *Smart Materials and Structures,* vol. 16, no. 2, pp. 429-438, 2007.

[49] A. P. Calderon, "On an inverse boundary value problem," *Comp. Appl. Math,* vol. 25, no. 2-3, pp. 133-138, 2006.

[50] A. Adler, and R. Guardo, "Electrical impedance tomography: regularized imaging and contrast detection," *IEEE Transactions on Medical Imaging,* vol. 15, no. 2, pp. 170-179, 1996.

[51] W. R. Breckon, "Image reconstruction in electrical impedance tomography," 1990.

[52] M. Cheney, D. Isaacson, J. Newell, S. Simske, and J. Goble, "NOSER: An algorithm for solving the inverse conductivity problem," *International Journal of Imaging Systems and Technology,* vol. 2, no. 2, pp. 66-75, 1990.

[53] N. Polydorides, W. R. B. Lionheart, and H. McCann, "Krylov subspace iterative techniques: on the detection of brain activity with electrical impedance tomography," *IEEE Transactions on Medical Imaging,* vol. 21, no. 6, pp. 596-603, 2002.

[54] T. J. Yorkey, J. G. Webster, and W. J. Tompkins, "Comparing reconstruction algorithms for electrical impedance tomography," *IEEE Transactions on Biomedical Engineering*, no. 11, pp. 843-852, 1987.

[55] L. Horesh, M. Schweiger, S. Arridge, and D. Holder, "Large-scale non-linear 3D reconstruction algorithms for electrical impedance tomography of the human head," in World Congress on Medical Physics and Biomedical Engineering, Seoul, Korea 2006, pp. 3862-3865.

[56] N. Polydorides, "Image Reconstruction Algorithms For Soft-Field Tomography," Department of Electrical Engineering and Electronics, University of Manchester Institute of Science and Technology, Manchester, United Kingdom, 2002.

[57] M. Soleimani, and W. R. B. Lionheart, “Nonlinear image reconstruction for electrical capacitance tomography using experimental data,” *Measurement Science and Technology,* vol. 16, pp. 1987, 2005.

[58] EIDORS Collaboration, "Electrical Impedance Tomography and Diffuse Optical Tomography Reconstruction Software," 2011.

[59] R. Lazarovitch, D. Rittel, and I. Bucher, “Experimental crack identification using electrical impedance tomography,” *NDT and E International,* vol. 35, no. 5, pp. 301-16, 2002.

[60] S. Pyo, K. J. Loh, T. C. Hou, E. Jarva, and J. P. Lynch, “A wireless impedance analyzer for automated tomographic mapping of a nanoengineered sensing skin,” *Smart Structures and Systems,* vol. 8, no. 1, pp. 139-155, 2011.

[61] T. Hou, K. Loh, and J. Lynch, “Spatial conductivity mapping of carbon nanotube composite thin films by electrical impedance tomography for sensing applications,” *Nanotechnology,* vol. 18, no. 31, pp. 315501, 2007.

[62] K. J. Loh, T. C. Hou, J. P. Lynch, and N. A. Kotov, “Carbon Nanotube Sensing Skins for Spatial Strain and Impact Damage Identification,” *Journal of Nondestructive Evaluation,* vol. 28, no. 1, pp. 9-25, 2009.

[63] K. Paulson, W. Breckon, and M. Pidcock, “Electrode modelling in electrical impedance tomography,” *SIAM Journal on Applied Mathematics*, pp. 1012-1022, 1992.

[64] B. Graham, and A. Adler, “Objective selection of hyperparameter for EIT,” *Physiological measurement,* vol. 27, no. S65, 2006.

[65] A. N. Tikhonov, A. V. Goncharsky, V. V. Stepanov, and A. G. Yagola, *Numerical Methods for the Solution of Ill-Posed Problems*, Boston: Kluwer Academic Publishers, 1995.

[66] A. Adler, T. Dai, and W. R. B. Lionheart, “Temporal image reconstruction in electrical impedance tomography,” *Physiological measurement,* vol. 28, 2007.

[67] M. J. O'Connell, P. Boul, L. M. Ericson, C. Huffman, Y. Wang, E. Haroz, C. Kuper, J. Tour, K. D. Ausman, and R. E. Smalley, “Reversible water-solubilization of single-walled carbon nanotubes by polymer wrapping,” *Chemical Physics Letters,* vol. 342, no. 3, pp. 265-271, 2001.

[68] I. Mazov, V. Kuznetsov, S. Moseenkov, A. Ishchenko, A. Romanenko, O. Anikeeva, T. Buryakov, E. Y. Korovin, V. Zhuravlev, and V. Suslyaev, “Electrophysical and Electromagnetic Properties of Pure MWNTs and MWNT/PMMA Composite Materials Depending on Their Structure,” *Fullerenes, Nanotubes, and Carbon Nanostructures,* vol. 18, no. 4-6, pp. 505-515, 2010.